

Hydrological information in gravity: observation and modelling

Dissertation

zur Erlangung des akademischen Grades doctor rerum naturalium
(Dr. rer. nat.)

vorgelegt dem Rat der Chemisch-Geowissenschaftlichen Fakultät der
Friedrich-Schiller-Universität Jena

von Diplom-Geophysiker Marco Naujoks
geboren am 03. Juli 1978 in Eisenach

Gutachter:

1. PD Dr. Corinna Kroner, FSU Jena, GFZ Potsdam
2. Prof. Dr. Gerhard Jentsch, FSU Jena
3. Prof. Dr. Hans-Jürgen Götze, CAU Kiel

Tag der öffentlichen Verteidigung: 26. November 2008

Zusammenfassung

Hydrologische Variationen und die sie verursachenden Phänomene stellen signifikante, breitbandige Informationen in geodynamischen Beobachtungen dar, insbesondere in hochauflösenden gravimetrischen Registrierungen. In diesem Zusammenhang entwickelte sich in den letzten Jahren eine neue Anwendung zeitlicher Schwerebeobachtungen: die Untersuchung natürlicher hydrologischer Massenverlagerungen und die ihnen zugrunde liegenden hydrologischen Prozesse.

Weltweit werden hydrologische Einflüsse in gravimetrischen Registrierungen beobachtet. Effekte aufgrund von Grundwasserspiegel- und Bodenfeuchtevariationen, Niederschlag und Schnee in einer Größenordnung von wenigen nm/s^2 bis zu mehreren 10 nm/s^2 wurden nachgewiesen. Diese müssen insbesondere aus den Zeitreihen hochgenauer supraleitender Gravimeter eliminiert werden, um kleinste geodynamische Signale (z. B. Schwingungen des Erdkerns oder coseismische Variationen) aufzulösen. In Gebieten mit hügeliger Topographie und/oder inhomogenem Untergrund ist eine einfache, auf hydrologischen Punktbeobachtungen basierende Reduktion oftmals nicht ausreichend, vor allem im Nahbereich von wenigen 100 m um das Gravimeter. Für die Entwicklung genauer Reduktionsmethoden unter diesen Gegebenheiten ist das Verständnis der den hydrologischen Variationen zugrunde liegenden komplexen Prozesse von zentraler Bedeutung. Sie müssen in ihrer räumlichen und zeitlichen Dynamik berücksichtigt werden.

Umgekehrt wird eine neue Methode zur Evaluierung hydrologischer Modellierungen getestet: die Verwendung zeitabhängiger Schwerebeobachtungen in Verbindung mit einer gravimetrischen 3D-Modellierung. Da zeitabhängige Schweredaten generell die integrale Information über hydrologische Massenänderungen enthalten, bieten sie eine wertvolle Ergänzung traditioneller hydrologischer Punktbeobachtungen. Von besonderem Interesse ist, in welchem Maß die Informationen dazu beitragen, das Verständnis der hydrologischen Prozessdynamik zu verbessern und bis zu welchem Grade sie der Evaluierung hydrologischer Modelle dienen können.

Schweredaten, abgeleitet aus GRACE-Satellitenbeobachtungen beinhalten Signale durch regionale und globale hydrologische Variationen. Kontinuierliche Registrierungen mit supraleitenden Gravimetern enthalten zusätzlich Informationen über lokale Änderungen. Ergänzend zu diesen Daten tragen Wiederholungsmessungen mit portablen Relativgravimetern in einem Netz zur Gewinnung zusätzlicher lokaler Informationen über flächenhafte hydrologische Variationen bei und ermöglichen eine Trennung des lokalen hydrologischen Effekts von regionalen oder globalen Änderungen. Dabei auftretende Fragen, z. B. ob die Ergebnisse dieser Wiederholungsmessungen von ausreichender Genauigkeit und wie eindeutig die erhaltenen Informationen sind, müssen als Grundlage weiterer Interpretationen beantwortet sein.

Bezüglich dieser Themen wurden im Umfeld des Geodynamischen Observatoriums Moxa in Thüringen, Deutschland, interdisziplinäre geophysikalische, geologische und hydrologische Untersuchungen durchgeführt. Das Observatorium Moxa ist für diese Studien beson-

ders geeignet, da die Station weltweit eine der rauschärmsten ist, der Untergrund geologisch gut untersucht ist und zahlreiche meteorologische und hydrologische Parameter beobachtet werden. Zusätzlich nehmen Hydrologen dort seit einigen Jahren ebenfalls Untersuchungen vor und ein lokales hydrologisches Modell der Observatoriumsumgebung wurde erstellt. Im Ergebnis der Arbeit sollen u. a. die hydrologischen Einflussfaktoren auf die Schwerebeobachtungen in Moxa geklärt sein und eine auf andere Observatorien übertragbare Methode zur Evaluierung lokaler hydrologischer Modellierungen vorliegen.

In Moxa werden hydrologisch bedingte Schwereänderungen von maximal mehreren 10 nm/s^2 mit dem stationären supraleitenden Gravimeter signifikant beobachtet. Um den hydrologischen Einfluss zu untersuchen, wurden verschiedene Experimente durchgeführt, in denen eine bestimmte Wassermasse auf definierte Gebiete in der Gravimeterumgebung aufgebracht wurde. Der resultierende Schwereeffekt von wenigen nm/s^2 bis zu mehr als 10 nm/s^2 konnte durch erste Modellierungen des unterirdischen Abflusses sowohl im Boden als auch durch Klüfte im aufgelockerten Festgestein erklärt werden.

Zusätzliche Information konnte durch flächenhafte Wiederholungs-Schweremessungen mit transportablen Gravimetern gewonnen werden. Im hügeligen Gebiet um das Observatorium wurde ein lokales Festpunktnetz mit maximalen Punktabständen von 65 m angelegt und eine Messanordnung entwickelt, mit der für diese Gegebenheiten Genauigkeiten von ca. 10 nm/s^2 erreichbar sind. Auf dieser Grundlage wurden Wiederholungsmessungen im saisonalen Rhythmus sowie zu speziellen hydrologischen Ereignissen wie Schneeschmelzen oder längeren Trockenzeiten in 19 Kampagnen zwischen November 2004 und September 2007 durchgeführt. Für die Messungen wurden drei bis fünf ausgesuchte, exzellente und gut kalibrierte LaCoste & Romberg D- und G-Gravimeter verwendet. Hydrologisch bedingte Schwerevariationen konnten so im lokalen Maßstab erstmalig flächenhaft und signifikant nachgewiesen und wirksame hydrologische Prozesse identifiziert werden.

Die durch Netzausgleichung nach der Methode der kleinsten Quadrate berechneten Standardabweichungen variieren von $\pm 9 \text{ nm/s}^2$ bis $\pm 14 \text{ nm/s}^2$ für eine Schweredifferenz in einer Kampagne. Für Änderungen einer Schweredifferenz zwischen zwei Kampagnen liegen sie zwischen $\pm 13 \text{ nm/s}^2$ und $\pm 20 \text{ nm/s}^2$. Zwischen den Punkten des Netzes wurden signifikante relative Schwereänderungen von bis zu 170 nm/s^2 (140 nm/s^2 zwischen zwei aufeinander folgenden Kampagnen) flächenhaft nachgewiesen. Sie korrelieren mit Änderungen der lokalen hydrologischen Situation.

In der Observatoriumsumgebung werden diverse hydrologische und meteorologische Parameter flächenhaft beobachtet. Sie bilden die Datengrundlage für ein lokales konzeptionelles hydrologisches Modell für das ca. $1.5 \times 1.5 \text{ km}^2$ große Einzugsgebiet des Baches Silberleite, der durch das Observatoriumstal fließt. Das Modell wurde für den Zeitraum zwischen Oktober 2003 und Juli 2007 angewandt. Der Vergleich zwischen simuliertem und gemessenem Abfluss der Silberleite am Wehr beim Observatorium dient der Validierung des Modells. Sie zeigt, dass die hydrologische Dynamik im Einzugsgebiet der Silberleite durch das Modell im Allgemeinen gut wiedergegeben wurde. Dies wurde auch durch den „Güteparameter“, eine Nash-Sutcliffe-Effizienz von $R_{eff} = 0.8$ bestätigt.

Aus den Ergebnissen der Modellierung wurden flächenhaft zeitabhängige hydrologische Massenvariationen abgeleitet, die räumlich als Dichteänderungen von Körpern in ein komplexes gravimetrisches 3D-Modell der Observatoriumsumgebung einfließen. Daraus wurden die resultierenden Schwereänderungen für die gravimetrischen Beobachtungspunkte als Zeitreihe berechnet.

Die Datengrundlage für die gravimetrische 3D-Modellierung bilden Karten der Bouguer- und der Freiluft-Anomalie, die auf flächenhaft durchgeführten Schweremessungen an 460 Punkten beruhen. Die Bouguer-Anomalie umfasst einen Schwerebereich von ca. $0.7 \cdot 10^{-5} \text{ m/s}^2$. Sie zeichnet sich in der Umgebung des Observatoriums Moxa durch kleinräumige Anomalien aus, die die lokalen geologischen Strukturen widerspiegeln.

Voraussetzung für eine erfolgreiche gravimetrische Modellierung ist die Einbeziehung umfangreicher geologischer, tektonischer und geophysikalischer Randbedingungen, um die mit der Potentialmethode einhergehenden Mehrdeutigkeiten ausreichend einzuschränken. Sie stehen im Bereich des Observatoriums in hohem Umfang aus mehreren Feldern zur Verfügung und fließen direkt in das gravimetrische Modell ein. Das hochauflösende gravimetrische 3D-Modell, welches auf Grundlage der Freiluft-Anomalie mit Schwerpunkt auf der realistischen und möglichst exakten Darstellung hydrogeologisch relevanter Strukturen sowie der Topographie entwickelt wurde, hat den Vorteil, dass die kleinräumige geologische und hydrologische Situation im Bereich des Observatoriums sehr gut integriert werden kann.

Die aus diesem kombinierten hydrologischen und gravimetrischen Modell abgeleiteten zeitabhängigen Schwereänderungen werden den signifikanten Ergebnissen der flächenhaften Wiederholungs-Schweremessungen und den Schwereresiduen des supraleitenden Gravimeters gegenübergestellt. Im Allgemeinen zeigen die modellierten Variationen und die beobachteten Schwereänderungen eine gute Übereinstimmung. Dies führt zu der Schlussfolgerung, dass der neue Ansatz der Kombination eines lokalen hydrologischen mit einem gravimetrischen Modell eine adäquate und erfolgreiche Methode für zeitabhängige Studien zur lokalen Hydrologie ist.

Aus den Modellierungen wird abgeleitet, mit welcher Amplitude hydrologische Änderungen, die in verschiedenen Entfernungen zum Gravimeter auftreten, die Schwere beeinflussen. Für die hügelige Umgebung des Observatoriums Moxa wird gezeigt, dass 30 % des lokalen hydrologischen Effekts in den Daten des supraleitenden Gravimeters aus einem Gebiet innerhalb eines Radius von 90 m um das Observatorium und 70 % aus einer Zone mit einem Radius von 250 m um die Station stammen.

Anhand dieser Informationen wurde eine hochpräzise und zuverlässige Reduktion für das lokale hydrologische Signal in den kontinuierlichen Schwerebeobachtungen des supraleitenden Gravimeters in Moxa entwickelt. Die Unsicherheiten von $\pm 1.5 \text{ nm/s}^2$ für Regenerereignisse und $\pm 2.5 \text{ nm/s}^2$ für saisonale Schwankungen sind sehr klein. Nach Reduktion der lokalen hydrologischen Effekte können die Daten hinsichtlich kontinentaler Wassermassenverlagerungen interpretiert werden. Klare saisonale Variationen mit einer Amplitude von ca. 32 nm/s^2 wurden entdeckt, die vorher durch die lokale Hydrologie verdeckt waren. Diese saisonalen Änderungen sind globalen Ursprungs, sie finden sich auch in Schwerevariatio-

nen abgeleitet aus globalen hydrologische Modellen und GRACE-Satellitenbeobachtungen. Damit können die Daten des supraleitenden Gravimeters auch zur terrestrischen Validierung von GRACE Satellitenbeobachtungen genutzt werden. Vorhandene Diskrepanzen zwischen den verschiedenen Beobachtungen und globalen hydrologischen Modellen liefern zusätzlich wertvolle Randbedingungen für regionale und globale hydrologische Modellierungen und tragen zu einer erhöhten Aussagekraft der Satellitenbeobachtungen bei.

Ein weiteres Ergebnis der Arbeit sind Ansätze zur Weiterentwicklung der lokalen hydrologischen Modellierung: Das modellierte hydrologische Signal von extremen Ereignissen wie Starkregen oder Schneeschmelzen wird durch das hydrologische Modell um einige Stunden bis Tage verzögert wiedergegeben. Die Reaktionszeit zwischen den verschiedenen Speichern des Modells müsste bei solchen Extremereignissen verkürzt werden. Von speziellen hydrologischen Prozessen – wie kleinräumige Heterogenitäten oder bisher nicht oder nicht gut bekannte Grundwasserfließvorgänge im Observatoriumstal – die bisher nicht ausreichend berücksichtigt wurden, können zusätzliche Unsicherheiten in der hydrologischen Modellierung herrühren.

Es wurde gezeigt, dass insbesondere hydrologische Schwankungen im Steilhang östlich des Observatoriums einen entscheidenden Einfluss auf die Schwereresiduen haben. Der Steilhang wurde als ein gravimetrisch signifikanter und zuvor unterschätzter hydrologischer Bereich in der Umgebung des Observatoriums bestätigt. Die hydrologischen Prozesse in diesem Hang wurden bisher nicht ausreichend detailliert untersucht. Hier könnte aus zusätzlichen hydrologischen Untersuchungen eine feinere räumliche Unterteilung des hydrologischen Modells in diesem für das supraleitende Gravimeter entscheidenden Gebiet abgeleitet werden, um das Modell noch realitätsnäher zu gestalten.

Das supraleitende Gravimeter am Observatorium Moxa ist fest in ein weltweites Netzwerk supraleitender Gravimeter eingebunden, dem „Global Geodynamics Project“. Andere Stationen des weltweiten Netzes sind in einer ähnlichen topographischen und hydrologischen Situation, die Schweredaten dieser Stationen sind ebenfalls durch lokale hydrologische Variationen beeinflusst. Daher können der Ansatz und die Methode, die für das Observatorium Moxa entwickelt wurden – wie einerseits hydrologische Informationen in der Schwere für hydrologische Modellierungen und hydrologische Prozessforschung verwendet und wie andererseits lokale hydrologische Einflüsse aus den Schweredaten reduziert werden können – prinzipiell auf andere Gravimeterstandorte und andere Regionen weltweit übertragen werden.

Zudem bilden die hydrologische und die gravimetrische Modellierung eine Grundlage, auch durch z. B. Porendruckänderungen induzierte Signale in Neigungs- und Straindaten anhand weiterführender geodynamischer 3D-Modellierungen mit finiten Elementen zu analysieren. Damit können einerseits weitere Informationen über die wirksamen hydrologischen Mechanismen und Prozesse gewonnen werden, andererseits kann der hydrologische Einfluss auf diese geodynamischen Beobachtungen verstanden und aus den Daten reduziert werden.

Summary

Hydrological variations and their underlying processes represent significant, broadband information in geodynamic observations, especially in high-precision gravity records. In this context a new application of temporal gravity observations has been emerging: the study of natural hydrological mass changes and their underlying processes.

Hydrological effects in temporal gravity observations due to water level and soil moisture variations, precipitation events, and snow in a range from a few nm/s^2 to some 10 nm/s^2 have been discussed for a while. On the one hand, they need to be eliminated in particular in time series of superconducting gravimeters as they interfere with small geodynamic signals. In areas with hilly topography or inhomogeneous subsoil, a simple reduction based on hydrological point measurements is usually not sufficient, especially in the close vicinity of some 100 m around the instrument. For such conditions, the underlying hydrological processes need to be considered in their spatial and temporal dynamics to allow the development of a more sophisticated reduction on a physical basis.

On the other hand, a new method for the evaluation of hydrological modelling is discussed: the deployment of temporal gravity observations and gravimetric 3D modelling. As temporal gravity data generally contain integral information on hydrological mass changes, they can be considered as a valuable supplement to traditional hydrological point measurements. Of particular interest is to what extent such information can be used to improve the understanding of hydrological process dynamics and to evaluate distributed hydrological models.

Gravity data derived from GRACE satellite observations are affected by global and regional hydrological variations. Continuous recordings from superconducting gravimeters also contain information on local changes. Complementary to these data, repeated gravity observations on a local network contribute to gaining additional local information on spatial changes in hydrology and enabling a separation of the local hydrological influence from regional and global changes. But first the questions need to be answered whether the results of these repeated measurements will be of sufficiently high resolution and accuracy, as well as how unique the information obtained will be.

Regarding these issues interdisciplinary research has been carried out at the Geodynamic Observatory Moxa, Germany. At Moxa, hydrologically induced gravity variations of several 10 nm/s^2 have been significantly observed with the stationarily operating superconducting gravimeter. To investigate the hydrological influence, different hydrological experiments were carried out in which a defined amount of water was added to specific areas within the gravimeter vicinity. Additional information was gained by spatially distributed and repeated high-precision measurements with transportable relative gravimeters. A local gravity network with maximum point distances of 65 m was established in the hilly area around the observatory. Using three to five LaCoste & Romberg relative gravimeters repeated measurements were carried out in 19 campaigns according to seasons as well as at special hydrological events like snow melt or dryness over a time period of nearly three years.

The standard deviations obtained by least squares network adjustment range from $\pm 9 \text{ nm/s}^2$ to $\pm 14 \text{ nm/s}^2$ for one observed gravity difference at one campaign, and from $\pm 13 \text{ nm/s}^2$ to $\pm 20 \text{ nm/s}^2$ for gravity changes between two campaigns. Between the points of the network,

significant spatial changes of up to 170 nm/s^2 were proved. They correlate with changes in the local hydrology.

Hydrological parameters are monitored which served as input for a local hydrological catchment model for the area of about $1.5 \times 1.5 \text{ km}^2$ around the observatory. Temporal hydrological mass variations, derived from the hydrological model, were applied as density variations to the bodies of a complex gravimetric 3D model of the observatory surroundings and the resulting gravity changes for the gravity observation sites were calculated as time series. The gravimetric modelling is based on a Bouguer as well as a free-air anomaly map compiled from measurements at 460 gravity points around the observatory. The model is well constrained by various geological and geophysical boundary conditions, it incorporates local geology, topography, and hydrological particularities.

The gravity changes obtained from the combined hydrological and gravimetric modelling were compared to the results of the repeated measurements and to gravity residuals derived from the superconducting gravimeter. The modelled variations correspond well to the observed gravity changes caused by hydrological fluctuations providing evidence that the combination of a local hydrological model with a gravimetric 3D model is a suitable method for hydrological time-dependent studies.

For the hilly surroundings of Moxa observatory it is demonstrated that 30 % of the local hydrological effect impacting the superconducting gravimeter data originate from an area within a radius of 90 m around the observatory, 70 % come from an area of 250 m around the station. Based on this information gained from the modelling, a high accuracy reduction for the local hydrological signal in the continuous gravity recordings was developed, with uncertainties of $\pm 1.5 \text{ nm/s}^2$ for rain events and $\pm 2.5 \text{ nm/s}^2$ for seasonal variations.

Applying this reduction, the data of the superconducting gravimeter at Moxa observatory become suitable to be interpreted with regard to changes in continental water storage. Clear global seasonal variations with an amplitude of approximately 32 nm/s^2 could be detected which were previously masked by the local hydrology. This seasonal signal is also found in variations based on global hydrological models and in GRACE satellite observations. Existing small discrepancies between the different observation techniques and the global hydrological modelling provide constraints for regional and global hydrological models.

Regarding the quality of the local hydrological model, improvements can be derived. The modelled effect of extreme hydrological events such as heavy rain or snow melt occurs time-delayed by some hours or days. This may be improved by shortening the response time between different storages of the model. From special and up to now not sufficiently considered hydrological processes such as small-scale heterogeneities or undetected water flow in the observatory valley, additional deficiencies may be induced into the model.

It was proved that, in particular, hydrological variations in the steep slope to the east of the observatory have a crucial impact on the gravimeter observations. This slope was identified to be a gravimetrically significant hydrological compartment. From additional hydrological investigations at this slope, a finer spatial partitioning of the hydrological model in this gravimetrically crucial area may be derived to further enhance the modelling.

In general, the methods developed and the results achieved for the surroundings of Moxa observatory can be transferred to other gravity stations and other regions worldwide.

Contents

Zusammenfassung	i
Summary	v
List of Figures	xi
List of Tables	xv
1 Introduction	1
1.1 Motivation	1
1.2 Outline and methodology	2
2 The Geodynamic Observatory Moxa	7
2.1 History	7
2.2 Geographical location and topography	7
2.3 Instrumentation and tasks	8
2.4 Geology	10
2.4.1 Regional setting	10
2.4.2 Stratigraphy	12
2.4.3 Fold structure	13
2.4.4 Joints	15
2.4.5 Faults	16
2.5 Hydrology	16
3 Temporal gravity observations	19
3.1 Temporal variations in the gravity field	19
3.2 Continuous observations with a superconducting gravimeter	20
3.2.1 The superconducting gravimeter	21
3.2.2 Hydrological influences on the superconducting gravimeter data	21
3.2.3 Experiments due to hydrological influences	23
3.2.4 First attempts to model the local hydrological effect	26
3.3 Repeated observations with L&R gravimeters	28

3.3.1	Local gravity network MoxaNet	28
3.3.2	Instrument calibration	31
3.3.3	Least squares adjustment	32
3.3.4	Results of the repeated gravity campaigns	33
4	Gravimetric 3D modelling	47
4.1	Data basis	47
4.2	Bouguer and free-air anomaly	47
4.3	Boundary conditions	52
4.4	The gravimetric 3D model	53
4.5	Residuals	58
4.6	Different model versions	60
5	Hydrological modelling	63
5.1	Model layout	63
5.2	Streamflow	63
5.3	Water content of hydrological storages	65
6	Combination of hydrological and gravimetric modelling	69
6.1	Combined model assembly	69
6.2	Translation of hydrological mass changes into density variations	69
7	Results	73
7.1	Local gravity network MoxaNet	73
7.1.1	Observation site on the hill	73
7.1.2	Measurement point on the observatory roof	74
7.1.3	Stations in the valley	74
7.1.4	Standard deviations for the different model versions	77
7.1.5	General findings	79
7.2	Superconducting gravimeter	80
7.2.1	Hydrological contributions from various zones around the gravimeter	80
7.2.2	Seasonal variations	82
7.2.3	Rain events and snow melt	83

8 Discussion of the results and conclusions	87
9 Outlook	91
9.1 Global interpretations	91
9.2 Other perspectives	93
10 References	95
Acknowledgements	I
Selbstständigkeitserklärung	III
Curriculum Vitae	V

List of Figures

1.1	Flow chart illustrating the combination of hydrological modelling, gravimetric modelling, and gravity observations as used in this thesis	4
2.1	Location of the Geodynamic Observatory Moxa in Europe as well as topographic and geographic features in its surroundings	8
2.2	Floor plan of Moxa observatory including important facilities, points of the local gravity network MoxaNet, and positions of hydrological sensors	9
2.3	Regional geological and geographical setting of the Moxa area	11
2.4	Geological map of the larger surroundings of Moxa observatory	12
2.5	Detailed geological and tectonical map of the vicinity of Moxa observatory	14
2.6	Geological northwest–southeast cut through the Moxa area	15
2.7	Geological southwest–northeast cut through the Moxa area	15
2.8	Sketch of hydrological processes and flow paths at Moxa observatory, and location of the superconducting gravimeter and the points of the MoxaNet	17
3.1	Hydrological influences on the superconducting gravimeter data	22
3.2	Influence of snow accumulation and melt on the observations with the superconducting gravimeter	22
3.3	First hydrological experiment: firemen irrigate the observatory roof area	24
3.4	First hydrological experiment: gravity variations caused by water mass variations in the roof area	24
3.5	Second hydrological experiment: changes in water table at four gauges due to water injection in the gap around the gravimeter pillar	25
3.6	Second hydrological experiment: gravity variations due to water injection in the gap around the gravimeter pillar and reduced gravity residuals	25
3.7	Third hydrological experiment: overview and modelled flow paths	25
3.8	Third hydrological experiment: gravity variations and water table changes	26
3.9	Third hydrological experiment: gravity variations and modelled gravity effect for the different water flow paths	26
3.10	Gravity effect of different hydrological contributions, unreduced gravity, summarised local hydrological effect and gravity signals reduced for the local hydrological influence	27
3.11	Observation points of the local gravity network MoxaNet	29
3.12	Location of the gravity observation sites on the east–west profile	31
3.13	Gravimeter lift: lower station in the valley at the observatory building	37

3.14	Gravimeter lift: upper station on the hill east of the observatory	37
3.15	Scattering of the observed drift-reduced gravity differences and temporal changes between the campaigns for each L&R gravimeter (part 1)	38
3.16	Scattering of the observed drift-reduced gravity differences and temporal changes between the campaigns for each L&R gravimeter (part 2)	39
3.17	Temporal changes in the gravity differences with standard deviation and some hydrological parameters at the observation points	41
4.1	Locations of gravimetric points, geoelectrical soundings, and seismic lines in the surroundings of Moxa observatory	48
4.2	Bouguer anomaly in the surroundings of Moxa observatory	50
4.3	Terrain reduction in the surroundings of Moxa observatory	50
4.4	Bouguer anomaly in the observatory vicinity without terrain reduction	51
4.5	Free-air anomaly in the surroundings of Moxa observatory and the 38 vertical planes of the gravimetric 3D model	51
4.6	Plane 19 of the gravimetric 3D model including topography, soil layer, disaggregated bedrock, and intact bedrock with densities up to a distance of 1 km from the observatory	55
4.7	Detail of plane 19 showing the geologic bodies as well as the soil layer in the direct vicinity of the observatory	55
4.8	Plane 3 of the gravimetric model	56
4.9	Plane 36 of the gravimetric model	56
4.10	Gravimetric 3D model of the observatory surroundings including topography, disaggregated and intact bedrock, and soil layer	57
4.11	Triangulation of the surfaces of the gravimetric 3D model and position of plane 19 within the model	57
4.12	Residuals of the gravimetric model	59
4.13	Local residuals of the gravimetric model	59
4.14	Histogram of the residuals of the gravimetric model	60
5.1	Topography around Moxa observatory and catchment area of the creek Silberleite	64
5.2	Hydrological response units (HRUs) of the hydrological model of the Silberleite catchment and lateral routing of the water	65
5.3	Observed and modelled streamflow of the creek Silberleite at the weir at Moxa observatory	66

5.4	Mean water content of all hydrological mass storages, spatially averaged over all HRUs	66
6.1	Combined gravimetric and hydrological modelling area and HRUs in the observatory surroundings	70
6.2	Plane 19 of the gravimetric model including also bodies (HRUs) of the hydrological model	71
6.3	Detail of plane 19 showing in particular the HRUs of the hydrological model in the direct vicinity of the observatory	71
6.4	HRUs of the hydrological model which are included into the gravimetric model for the soil layer and the disaggregated bedrock	72
6.5	Triangulation of the surfaces of the gravimetric 3D model including the HRUs and position of plane 19	72
7.1	Temporal changes in the observed gravity differences with standard deviation and modelled hydrologically induced variations for five different model versions (part 1)	75
7.2	Temporal changes in the observed gravity differences with standard deviation and modelled hydrologically induced variations for five different model versions (part 2)	76
7.3	Contributions to the local hydrological effect in gravity from the different HRUs in a zone of up to 90 m around the superconducting gravimeter	81
7.4	Contributions to the local hydrological effect in gravity from different zones up to 1000 m around the superconducting gravimeter at Moxa observatory	81
7.5	Local hydrological effect derived from the combined modelling for the superconducting gravimeter as well as gravity residuals without and with local hydrological reduction	82
7.6	Detail of Figure 7.5 for the summer period from 04/05/26 to 04/07/27.	84
7.7	Detail of Figure 7.5 for the winter period from 05/02/01 to 05/04/30.	85
9.1	Gravity variations of the superconducting gravimeter at Moxa unreduced and reduced for local hydrology in hourly values and as monthly arithmetic means for comparison with GRACE and global hydrological models	92
9.2	Comparison of gravity residuals from Moxa reduced and unreduced for local hydrology to GRACE solutions and gravity variations derived from changes in continental water storage computed with the WGHM model	93

List of Tables

3.1	Coordinates and elevations of the observation points in the local gravity network MoxaNet	30
3.2	Dial and feedback system calibration terms of the used L&R gravimeters . .	32
3.3	Standard deviations for the L&R gravimeters derived from least squares adjustment for each campaign	34
4.1	Measured rock densities around Moxa observatory applied in the gravimetric model	53
4.2	Different versions of the gravimetric model	61
7.1	Standard deviations between observations and modelling for the points of the local gravity network	78

1 Introduction

1.1 Motivation

Temporal gravity observations are affected by every mass change taking place in the earth's system based on attraction due to Newton's law of gravitation and deformations due to loading effects. Hence, gravity data contain comprehensive information on tides, barometric pressure, and polar motion, but also on hydrology-related mass changes such as groundwater table or soil moisture fluctuations. Both, local hydrological mass changes and continental water storage variations impact gravity observations.

The influence of hydrological variations in gravity data, e.g. from rain or snow, changes of the groundwater table or the soil water content, is known worldwide and for a long time (e.g. Bonatz, 1967; Lambert & Beaumont, 1977; Elstner & Kautzleben, 1982; Elstner, 1987; Mäkinen & Tattari, 1988; Bower & Courtier, 1998). In particular, the continuous high resolution recordings of superconducting gravimeters show these effects which are broadband and occur with an amplitude between a few nm/s^2 and some 10 nm/s^2 ($10 \text{ nm/s}^2 = 1 \mu\text{Gal}$) (Peter et al., 1995; Crossley et al., 1998; Harnisch & Harnisch, 1999; Imanishi, 2000; Virtanen, 2000; Kroner, 2001; Zerbini et al., 2001; Amalvict et al., 2004; Abe et al., 2006; Meurers, 2006; Neumeyer et al., 2006; Sato et al., 2006; Kroner et al., 2007).

From the hydrological point of view, the impact of local and global hydrological effects on gravimeter records can be considered as a valuable data source because it provides a supplement to traditional meteorological and hydrological point observations. To obtain the spatial data necessary for water balance computations like precipitation, water level, evaporation, and soil moisture is partially difficult and generally only possible for a limited number of point observations. The advantage of gravity data lies in the fact that they contain integral information on hydrological mass changes. In this context the questions arise to what extent gravity data can be used to improve the understanding of hydrological process dynamics and which potential they provide for the parametrisation and validation of hydrological models.

One way to apply such data for hydrological model evaluation on a local scale is the direct comparison between gravity variations and simulated storage changes computed with a hydrological model as described by Krause et al. (2005, 2008) and Hasan et al. (2006, 2008). A more promising but also more difficult way is presented in this thesis: the physically based conversion of the simulated water storage changes into gravity changes.

From the geophysical point of view, hydrological variations and their underlying processes have become an important focus of scientific interest in recent years, in particular as they represent a significant, broadband disturbance in geodynamic observations. Besides strain and tilt measurements, in particular the high resolution records of superconducting gravimeters show these effects. As geodynamic signals such as oscillations of the earth's core or coseismic variations are expected in a similar or even smaller order of magnitude than the effect of hydrological variations, the gravity data require an a priori elimination of these influences.

Local hydrological fluctuations in particular have a crucial impact on gravity observations as recent publications emphasise (Boy & Hinderer, 2006; Harnisch & Harnisch, 2006; Imanishi et al., 2006; Kroner & Jahr, 2006; Van Camp et al., 2006; Hokkanen et al., 2007a,b; Nawa et al., 2007). Meurers (2006) and Meurers et al. (2007) show by modelling that the direct vicinity (< 100 m) of the observatory at Vienna (Austria) has an essential influence on the gravimeter signals for short-term meteorological events (e.g. heavy rain) as well as for long-term hydrological variations. This is generally confirmed by Virtanen et al. (2006). Comparing the gravity effect computed from mass variations in local, regional, and global hydrological models to gravity observations for the station Metsähovi (Finland) they conclude that about two thirds of the observed hydrological variations of the signal are of local origin.

Furthermore, the elimination of the local hydrological effect is a prerequisite to interpret the superconducting gravimeter data with regard to changes in continental water storage (Neumeier et al., 2006, 2008). They may behold as “ground truth” for satellite observations, e.g. of the Gravity Recovery and Climate Experiment GRACE, and may play an essential role in the evaluation of global hydrological models.

1.2 Outline and methodology

The temporal and spatial complexity as well as variability of hydrological processes in the surroundings of a gravimeter generally make a quantification of the local hydrological effect in gravity data a challenging task. Most of the investigations carried out so far are based on strong simplifications of the geological situation such as homogeneous, horizontal layers in the subsoil and the hydrological process descriptions (e.g. Delcourt-Honorez, 1995; Peter et al., 1995; Crossley et al., 1998; Dittfeld, 2000; Harnisch et al., 2000; Kroner, 2001, 2002; Nawa et al., 2007; Boy & Hinderer, 2006; Harnisch & Harnisch, 2006; Imanishi et al., 2006; Kroner & Jahr, 2006; Hokkanen et al., 2007a,b; Kroner et al., 2007). Because of such generalisations it is reasonably likely that local variations (within a radius of 1 km) are only partially or inexactly captured, in particular if the gravimeter surroundings are characterised by inhomogeneous subsoil or topography changes.

To avoid this, the local hydrological dynamics, e.g. possible water flow processes (Kroner & Jahr, 2006; Hokkanen et al., 2007a), have to be considered in more detail. Extensive hydrological and geological research as well as spatial hydrological modelling is necessary to reduce or, in the best case, to eliminate the hydrologically induced effects in the gravity data. Additionally, from small-scale spatial gravity information a broader and quantitative knowledge about the local hydrological processes acting in the surrounding of a superconducting gravimeter can be gained and further constraints for hydrological modelling on a local scale may be derived.

First steps to observe hydrological influences in gravity at different locations have been made by Wilson et al. (2007). They deploy a transportable superconducting gravimeter in Texas and other regions of the US for hydrological studies. Andersen et al. (2008) use a Scintrex

CG5 relative and a Micro-g LaCoste A10 absolute gravimeter in one of the world's largest wetlands, the Okavango delta in Botswana on measurement points in distances of about 100 km from each other. The expected gravity changes between 200 and 800 nm/s² should help to quantify hydrological variations and derive constraints for hydrological modelling.

In the first part of this thesis it is investigated how standard deviations of about ± 10 nm/s² on a local network by measurements using relative gravimeters in repeated campaigns can be reached. The second part on the one hand aims at a reliable evaluation of a small-scale hydrological catchment model by gravity data. On the other hand, a suitable reduction of the local hydrological effect in the superconducting gravimeter recordings is developed making them suitable to be interpreted with regard to changes in continental water storage as observed by the GRACE satellite mission and modelled by different global hydrological models.

Regarding these issues research has been carried out in the surroundings of the Geodynamic Observatory Moxa, Germany. Moxa observatory with its vicinity is a well suited location for geophysical and hydrological investigations: The noise level here is one of the lowest worldwide, numerous hydro-meteorological parameters are observed at several points, the geology of the subsoil is well investigated, and a number of hydrological investigations have been carried out. Besides this, many geoscientific boundary conditions from geophysical surveys are available and contribute directly to the modelling. This provides the information for well constrained hydrological and gravimetric modelling for the complex geological and hydrological situation in the surroundings of Moxa observatory.

Topography as well as the geological and hydrological situation in the surroundings of the observatory are important constraints for the investigations. They are discussed in Section 2 together with a brief description of Moxa observatory.

At Moxa observatory the superconducting gravimeter GWR CD 034 is operating for nearly 10 years. Significant hydrologically induced gravity changes are observed with this instrument in an order of magnitude of some 10 nm/s² (Kroner, 2001; Kroner et al., 2004, 2007). The gravity observations are described in detail in Section 3 together with a brief discussion of general temporal variations in the gravity field. The superconducting gravimeter at Moxa observatory is not an isolated instrument. It is integrated in the GGP network (Section 2.3). Other GGP stations worldwide (e.g. Vienna, Austria or Strasbourg, France) are in a similar topographic and hydrological situation. The gravity data of these stations are affected by hydrological variations as well.

From repeated gravity measurements carried out with transportable LaCoste & Romberg (L&R) relative instruments on a local network in the area around the observatory, spatial information on gravity changes was gained. These gravity observations, discussed in Section 3 as well, are used to constrain ambiguities, and to localise hydrological areas influencing gravity. Because for these observations always changes in gravity differences between two points are considered, only local hydrological variations are reflected. Regional or global changes vanish in the gravity differences enabling the separation of the local hydrological effect from regional or global changes.

Based on a Bouguer and a free-air anomaly map, compiled from measurements on 460 grav-

ity points, a gravimetric 3D model was set up for the observatory surroundings (Section 4). It incorporates local geology, topography, and hydrological particularities. The model is well-constrained by various geological and geophysical boundary conditions as results from seismic and geoelectric measurements or information from digging and from boreholes. The residuals of the gravimetric model are small, underlining, that the model is suited for the hydrological studies aimed for.

A small-scale hydrological catchment model is discussed in Section 5. It is based on hydrological point observations and physio-geographical information and was developed to study hydrological processes in the surroundings of the observatory.

To combine both models, they had to be modified in order to achieve that mass variations derived from the local hydrological model in hourly time steps could be converted to density changes of the subsoil bodies of the gravimetric 3D model. The disaggregated bedrock and the soil layer of the gravimetric model were subdivided into small single bodies which represent homogeneous hydrological units. Temporal hydrological mass variations, derived from the hydrological model, were applied to these bodies as density variations and the resulting gravity changes for the gravity observation sites were calculated as time series. This new approach is described in Section 6.

The output of the gravimetric 3D model – temporal modelled hydrological gravity variations for the observation sites in hourly time-steps – was compared to observed gravity changes in Section 7 for both the results of the local network and the recordings of the superconducting gravimeter. Hereby, the temporal and spatial variability of hydrological variations in the gravity data was analysed. In this context the quality of the local hydrological model was evaluated and possible modifications were proposed. Finally, the feasibility to develop a more sophisticated reduction of local hydrological effects in the superconducting gravimeter data was studied. The principal approach of the investigations in this thesis is illustrated in Figure 1.1 which shows the three main research areas hydrological modelling, gravimetric

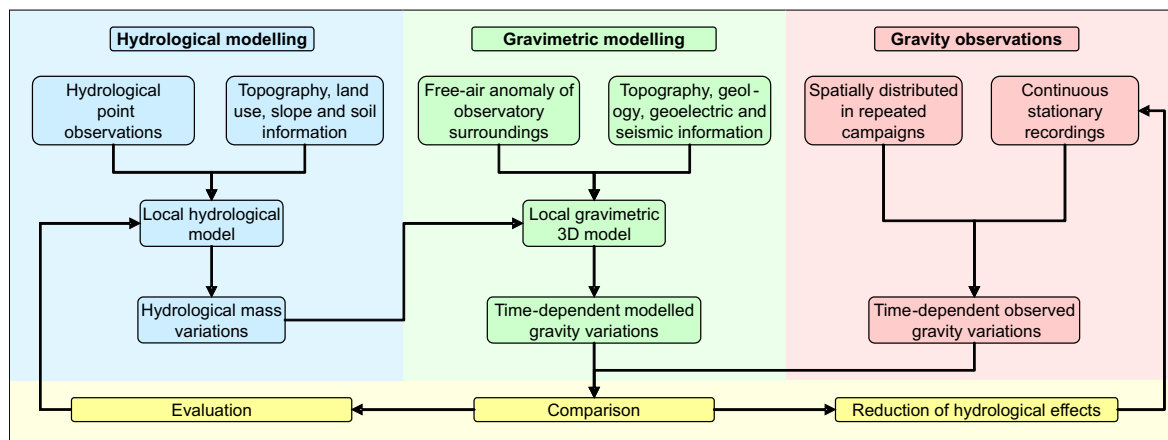


Figure 1.1: Flow chart illustrating the combination of local hydrological modelling, local gravimetric modelling, and the gravity observations at Moxa observatory as used for the investigations.

modelling, and temporal gravity observations together with the major work tasks and the application of the results.

This principal approach – how to use the hydrological information in gravity for hydrological modelling on the one hand and reduce it from the gravity data on the other hand – can be transferred to other gravimeter stations worldwide.

Parts of this thesis are already published in peer reviewed or other journals or are in preparation for publication. Some results of the repeated observations are published in [Naujoks et al. \(2006\)](#), [Kroner et al. \(2007\)](#) and [Naujoks et al. \(2008d\)](#). The results from the static geological and gravimetric modelling are in preparation to be published in [Naujoks et al. \(2008a\)](#). Results of the hydrological modelling are submitted ([Krause et al., 2008](#)) and the results of the combined gravimetric and hydrological modelling are in preparation for publication ([Naujoks et al., 2008b](#)). Additionally, more general information on the relation between gravity field observations and hydrology can be found in [Naujoks et al. \(2008c\)](#).

2 The Geodynamic Observatory Moxa

2.1 History

In the centre of the university city Jena a seismological station started to record seismicity in the year 1900. In 1923 it was moved out of the city centre to avoid the influence of traffic noise. In the middle of the fifties of the 20th century, a new location for the station had to be found again because of increased anthropogenic effects in Jena (traffic, industry) and on account of a growing instrument park (Teupser, 1975; Jentzsch, 2004).

Criteria for the new location were a low ground noise, enabled by a minimum distance of 10 km to cities, main roads, railway systems and industrial facilities, and an appropriate geologic subsoil. That is consolidated rock which does not amplify geodynamic signals or ground movements. A location in a valley seemed to be best suited, allowing the construction of a gallery in which the instruments are at least partially shielded against disturbing environmental influences. Additionally, the new station should be reachable by car in a reasonable time from Jena.

A suitable location fulfilling the criteria for site selection was found in a valley near the village of Moxa. Since 1964 the Seismological Station Moxa is operating. In 1997 a reconstruction and extension started. New instruments for tilt, strain and gravity observations were installed and Moxa station was renamed to Geodynamic Observatory Moxa.

2.2 Geographical location and topography

Moxa observatory is located in southern Thuringia, approximately 30 km south of the city of Jena and 1 km northwest of the village of Moxa in the valley of the small creek Silberleite. The surroundings of the observatory are characterised by hilly topography. The geographical coordinates of the station are 50.645°N, 11.615°E, and the elevation is 455 m above mean sea level. In Figure 2.1 the location of Moxa observatory in Europe is shown, and the main topographic features in the surroundings of the observatory are given with the village Moxa in the east. The valley of the creek Silberleite is in the central part of the study area generally running northwest–southeast. In the immediate vicinity of the observatory it strikes north–south. The slopes bordering the valley show a different morphology: The eastern slope has an inclination of up to 18°; it is more steep than the western slope with an inclination between 2 and 5°. North of the observatory the valley of the Silberleite is very narrow; the width is about 25 m. It opens to the south on a width of up to 160 m. The observatory buildings are oriented exactly to the north, following the course of the valley in this approximately 100 m long section. The central part of the facilities is built partially into the eastern slope below ground level. From this part a gallery runs further east into the hill. After a distance of 45 m it turns to the south (Figure 2.2).

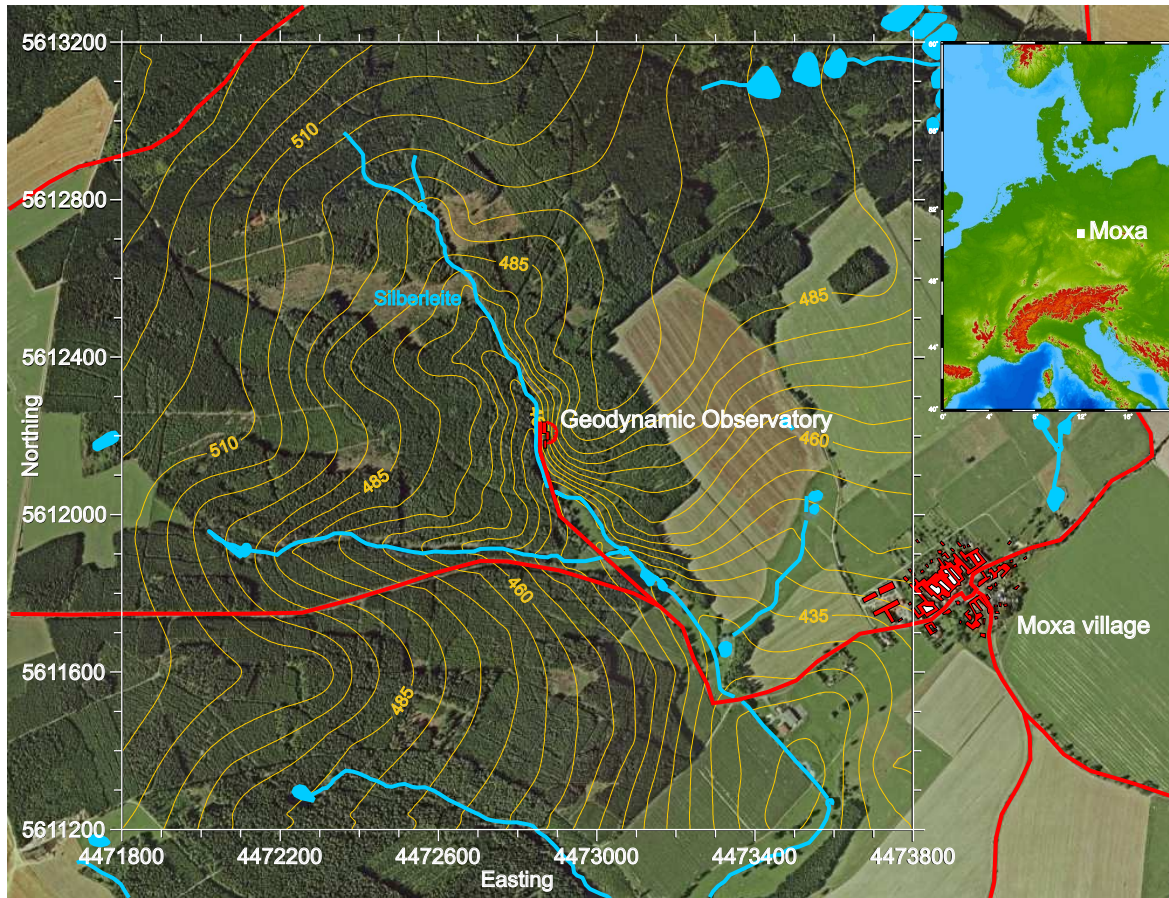


Figure 2.1: Location of the Geodynamic Observatory Moxa in Europe as well as topographic and geographic features in its surroundings. The aerial photograph was taken from [Google Earth \(2008\)](#).

2.3 Instrumentation and tasks

The task of the staff at the observatory is the monitoring, analysis, and interpretation of geodynamic effects regarding deformations of the earth's body and crust as well as the gravity field. Moxa observatory is part of a number of regional and global networks. Observations are carried out in a broad frequency band from seismology with high frequencies up to 80 Hz down to long- and aperiodic geodynamic gravity, tilt, and strain observations. For the observations different geophysical sensors are available ([Jahr et al., 2001](#)). In [Figure 2.2](#) the floor plan of the observatory is shown including all important facilities and instruments.

At the end of the gallery, the part of the station least sensitive to disturbances, the chamber for the seismometers is located. The rock coverage amounts here, approximately 60 m inside the hill, to about 35 m. As a station of the German Regional Seismological Network (GRSN) and the Thuringian Seismological Network (TSN) the observatory is equipped with broadband STS-1 and STS-2 seismometers. For short and long periods additional seismometers installed on concrete pillars are available in the observatory building.

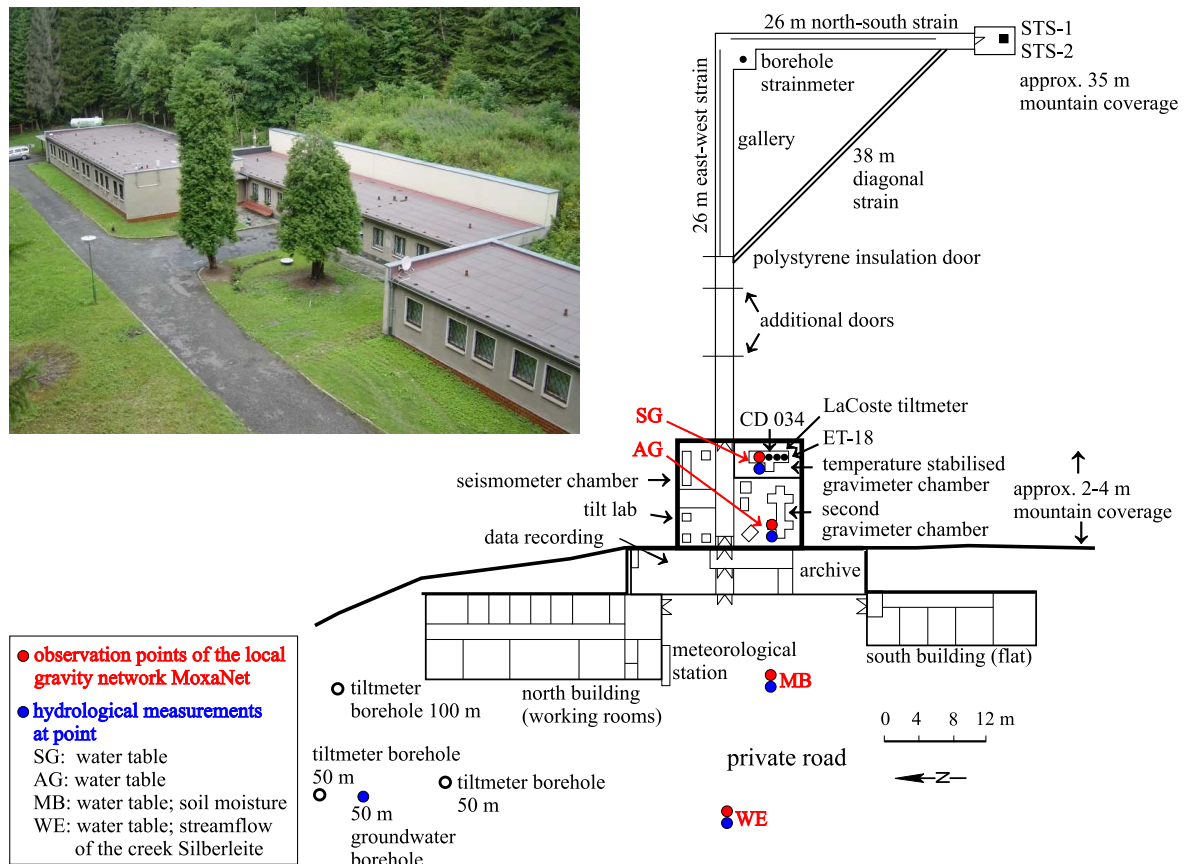


Figure 2.2: Floor plan of the Geodynamic Observatory Moxa showing all important facilities (Schulze, 1998, modified). Additionally, some points of the local gravity network MoxaNet (Section 3.3.1) are given in red and the positions of local hydrological sensors are marked in blue.

At Moxa, a north–south and an east–west oriented quartz strainmeter are operated in the gallery, each strainmeter 26 m long. A 38 m long diagonal laser strainmeter, installed in a horizontal borehole, connects the end points of the two quartz instruments. Additionally, a three-component borehole strainmeter is installed in the gallery knee. By strain measurements in different directions the surface strain can be determined. Geodynamic and environmental signals can also be studied.

An insulation door which guarantees nearly steady temperature and humidity conditions separates the gallery from the laboratories and other measuring rooms. At the observatory the dual-sphere superconducting gravimeter CD 034 is continuously operating in a temperature-stabilized room. Additionally, the spring gravimeter L&R ET-18 is in use. The gravimeters are installed on concrete pillars. The observatory is part of a world-wide network of superconducting gravimeters, the Global Geodynamics Project GGP (Crossley et al., 1999). The influence of different effects on the gravity field is studied (cf. Section 3.1).

A tiltmeter lab serves for maintenance and test of ASKANIA borehole tiltmeters. Three boreholes with steel casings are available for these instruments outside the observatory building.

Two of them have a depth of 50 m, one is 100 m deep. The tiltmeters are operated to study geodynamic and environmental signals. Additionally, on the pillar of the superconducting gravimeter a LaCoste tiltmeter is running.

The observatory buildings are used as workrooms, archive and for lodging. At the northern building a meteorological station is installed at which the following environmental parameters are monitored:

- barometric pressure in the gravimeter room, in the gallery, and outside the building;
- air temperature in the seismometer room, in the gravimeter room, in the gallery, and outside the building;
- precipitation;
- wind direction and velocity;
- relative air humidity;
- solar radiation.

Barometric pressure is recorded every second, the other parameters every 10 s. Additionally, the observatory belongs to the European Combined Geodetic Network (ECGN). GPS is continuously monitored at a location approximately 350 m south of the observatory.

Water level changes are measured at four sites in and around the observatory using the hydrostatic pressure sensor *water pilot FMX 167* by Endress+Hauser. Soil moisture variations are monitored at three sites and in two depths by Trime-EZ TDR probes (Figure 2.2).

The measurements serve as data basis for the development of reduction models for environmental effects in the geophysical observations and as additional constraints for hydrological modelling.

2.4 Geology

The information in this section provides constraints for a realistic hydrological and gravimetric modelling of the observatory surroundings. The different geological units are introduced. Faults and joints, which offer hydrological flow paths, are also discussed.

2.4.1 Regional setting

The surroundings of Moxa observatory are part of the Saxothuringicum which belongs to the basement complex of the West and Central European Variscan Belt (Linnemann, 2004). This belt runs from the northern border of the Bohemian Mass to the Ossa Morena Zone of the Iberian Peninsula passing the Armorican Massif (Figure 2.3).

The Thuringian-Franconian Slate Mountains are a part of the low metamorphic units of the Saxothuringicum. They consist of the basement units of the Schwarzburg Anticlinorium, the Ziegenrück Synclinorium and the Berga Anticlinorium (Figure 2.3; Timmermann, 1978; Linnemann, 2004). The study area is shaped by the Thuringian and Bavarian Facies which are characterised by hemipelagic-neritic basin sediments. These autochthonous rocks were sedimented in a uniform deposition area (Franke, 1984).

The Ziegenrück Synclinorium, in which Moxa is situated, strikes northeast–southwest (Figure 2.3). In the southeast it is bordered by the Berga Anticlinorium. The northern and northwestern border represents the Thuringian Trough, and in the west it borders on the Schwarzburg Anticlinorium (Timmermann, 1978). In the southwest the Franconian Forest Traverse Zone, a part of the Franconian Line, separates the Ziegenrück Synclinorium from the Teuschnitz Synclinorium.

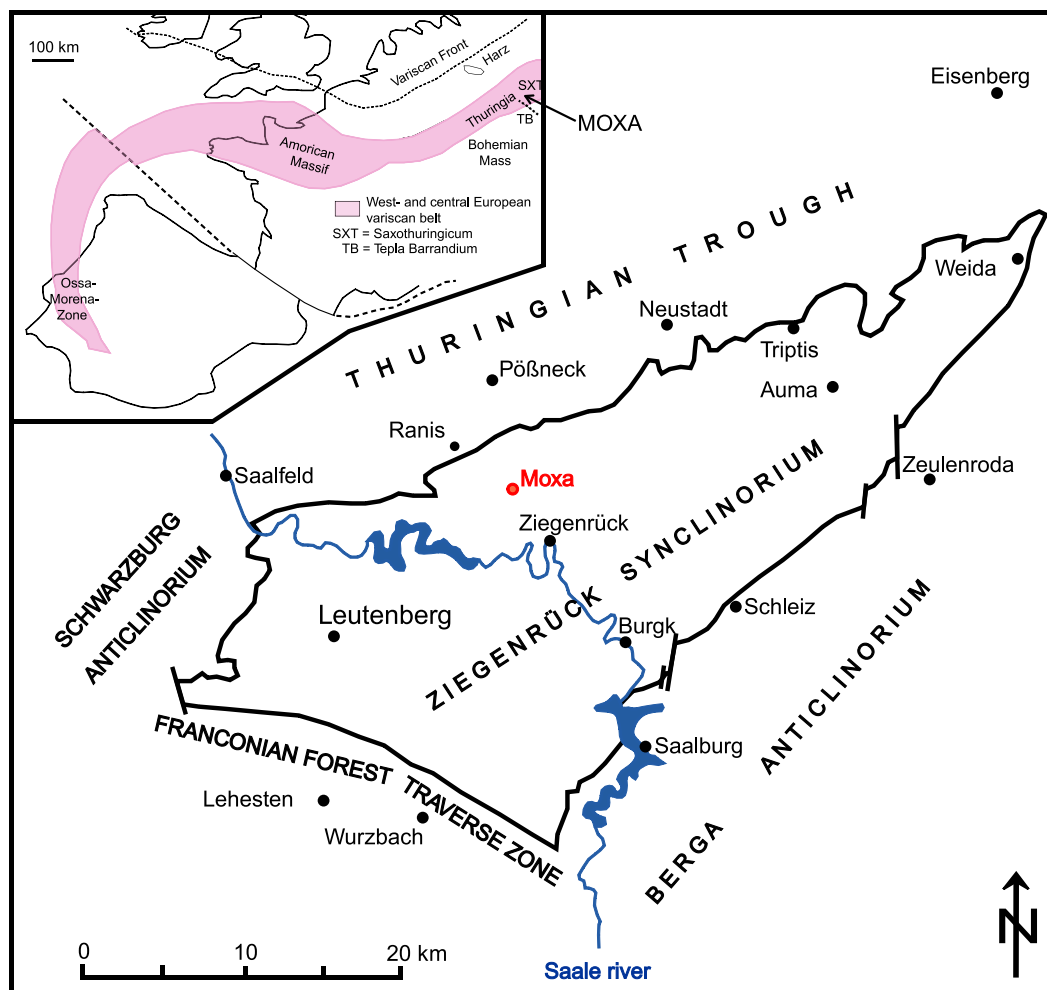


Figure 2.3: Regional geological and geographical setting of the Moxa area (Timmermann, 1978; Linnemann, 2004; Kasch, 2006, modified).

The Ziegenrück Synclinorium comprises turbiditic deposits of banded clay slates, greywackes, claystones, sandstones and conglomerates of the Thuringian Flysch Facies which reach a thickness of up to 3600 m. The rocks are between 345 and 325 million years old and belong to the stratigraphic unit Culm of the Lower Carboniferous. North of the Moxa area, following the line Ranis-Wernburg (Figure 2.4), rocks of the Zechstein period discordantly lie on the folded carboniferous rocks. This Zechstein crop-out is followed by Lower Triassic sediments in the northwest (Figure 2.4).

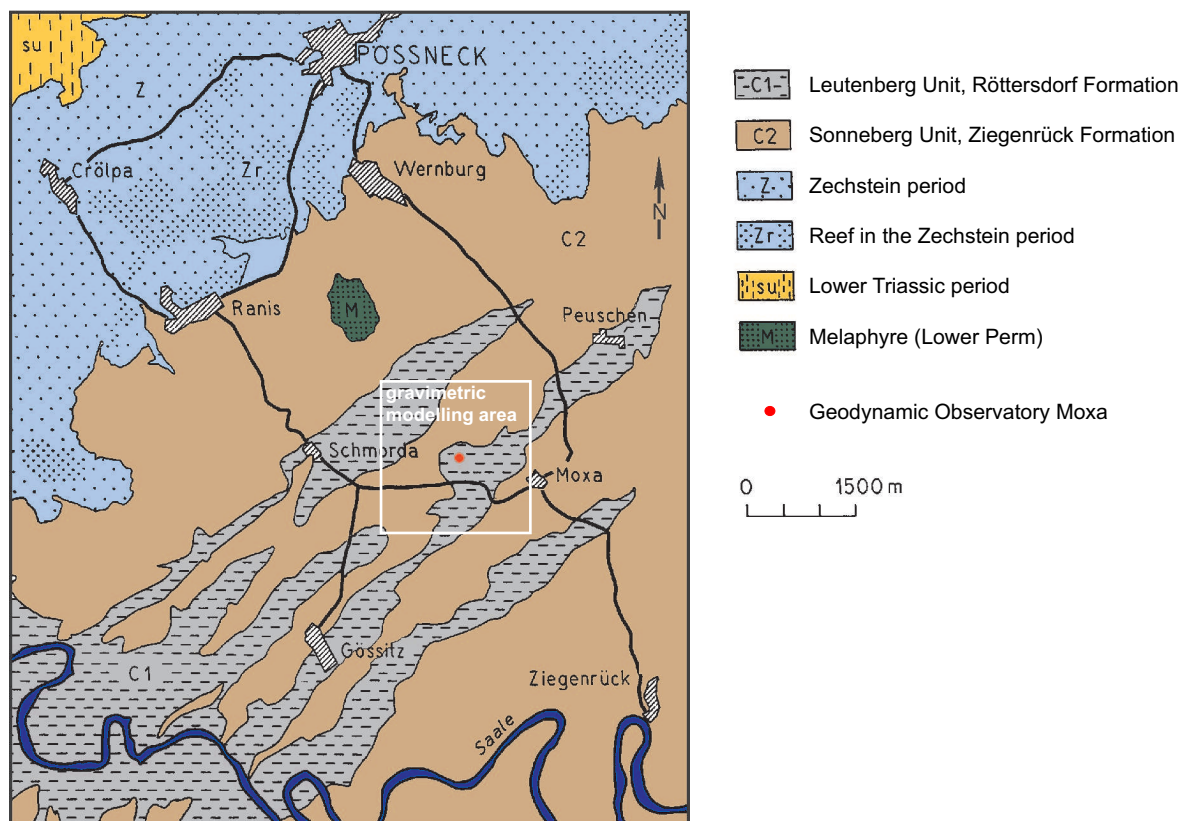


Figure 2.4: Geological map of the larger surroundings of Moxa observatory (Liebe & Zimmermann, 1888, modified). The gravimetric modelling area is also given.

2.4.2 Stratigraphy

The Ziegenrück Synclinorium is assigned to the Culm which is divided into the Lower and the Upper Culm. The Lower Culm consists of the Leutenberg Unit comprising the Lehesten, Hasenthal, Kaulsdorf and Röttersdorf Formation. The Sonneberg Unit as part of the Upper Culm comprises the Ziegenrück and Teuschnitz Formation (Wucher et al., 2001).

The rock formations in the study area completely consist of clastic sedimentary rocks. Psaphites, psammites, silt slates and clay slates are found. The following rocks can be distinguished:

- greywackes, fine to medium granular;
- greywackes, medium to coarse grained;
- greywackes, limy;
- conglomerates, rough sandy to fine gravelly;
- conglomerates, fine gravelly to rough gravelly;
- clay slates or silt slates;
- sandstones, fine to medium granular.

2.4.3 Fold structure

The surroundings of Moxa observatory are characterised by a southwest–northeast striking folded structure as first mapped by [Liebe & Zimmermann \(1888\)](#) in the geological map GK25 no. 5335 (Ziegenrück) and confirmed by [Zimmermann \(1912\)](#), [Schroeder \(1966\)](#), [Schwan \(1995\)](#), [Wucher \(1997\)](#), [Schwan \(1999\)](#), [Linnemann et al. \(2002\)](#), and [Hempel \(2003\)](#). The rocks belong to the north–eastern part of the Ziegenrück Synclinorium.

According to [Hempel \(2003\)](#) the existing folds can be generally classified due to their wavelength: 1st order folds describe the large structures of the anti- and synclinoriums with a wavelength of more than 1000 m as the southwest–northeast striking fold structure of the Sonneberg and Leutenberg Unit of the Lower Carboniferous within the Ziegenrück Synclinorium in the Moxa area (Figures 2.4 and 2.5). Folds of the 2nd order have wavelengths between 100 and 1000 m and 3rd order folds between 0.5 and 100 m. The wavelength of 4th order folds range between fist size and 0.5 m. In general, these folds are south–east vergent as well. They build up the Röttersdorf and the Ziegenrück Formation which are structures within the formations of the Sonneberg and Leutenberg Unit (Figure 2.5). The fold axes strike between 40 and 60° and dip northeast with an angle of 10 to 15°. In some cases up to 25° can be reached. Two geological cross-sections through the study are given in the Figures 2.6 and 2.7. The northwest–southeast cut (Figure 2.6) is oriented perpendicular to the fold structure, the southwest–northeast cut (Figure 2.7) parallel.

In the Moxa area 3rd order structures were found. However, in the larger surroundings of the study area also structures of the 4th order could be identified. This is due to little outcrops in the direct vicinity of Moxa observatory. Thus, it can be assumed that around Moxa observatory folds of the 4th order also exist, in particular in the more incompetent layers of the banded slates (Figures 2.5, 2.6, 2.7). From the measured data a uniform fold structure was derived ([Kasch, 2006](#)). Additionally, a mean west-southwest–east-northeast strike direction of the foliation was measured in the area around Moxa observatory. Both, foliation and folding result from compression and the load of sediments in the central former Culm Basin ([Kasch, 2006](#)).

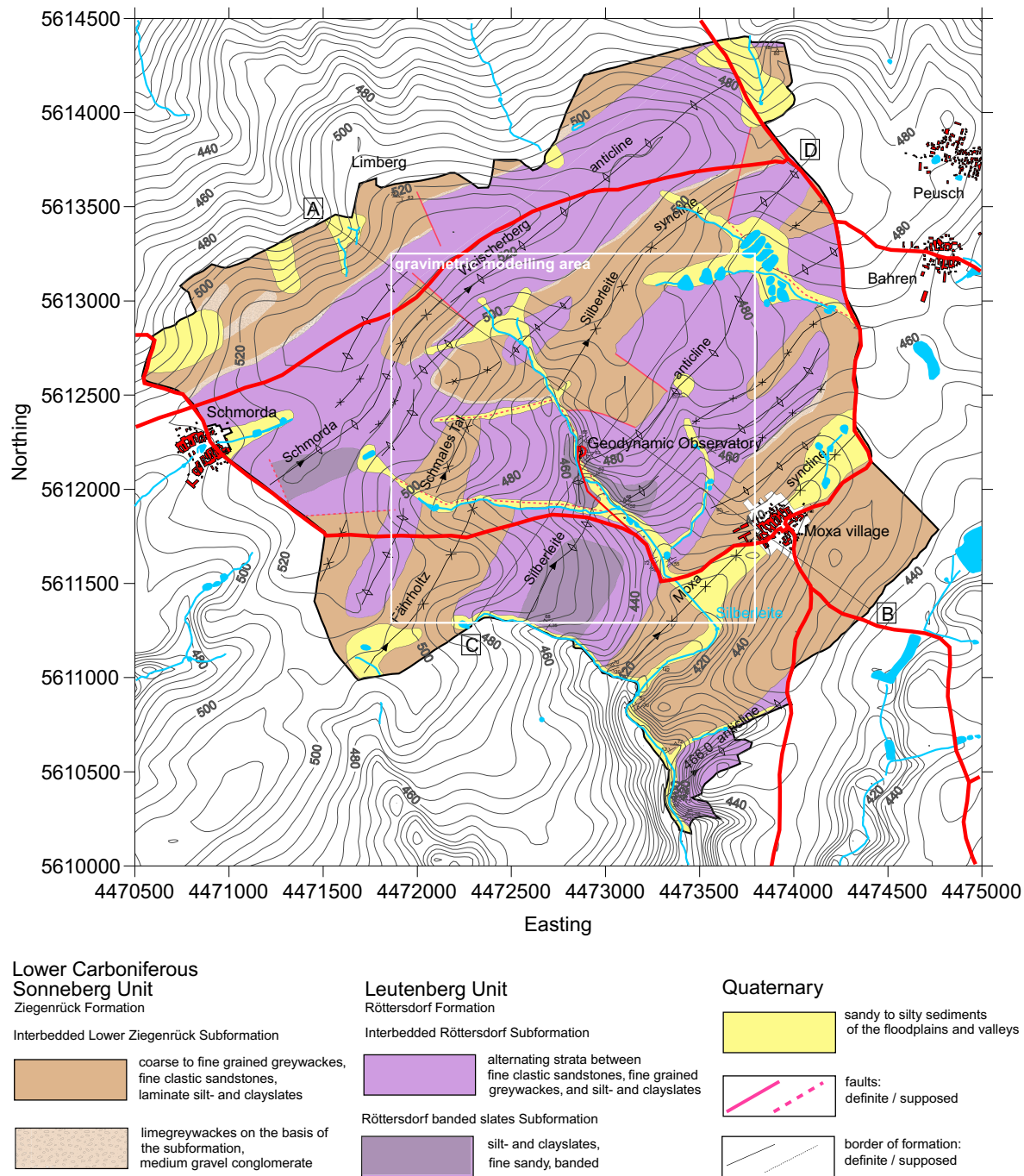


Figure 2.5: Detailed geological and tectonical map of the surroundings of Moxa observatory (Kasch, 2006, modified). The gravimetric modelling area is also given.

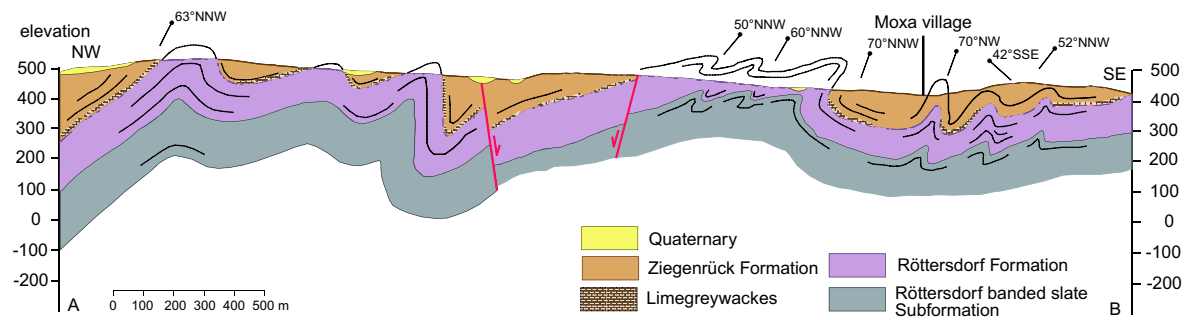


Figure 2.6: Geological northwest-southeast cut through the Moxa area following the AB line in Figure 2.5 (Kasch, 2006, modified).

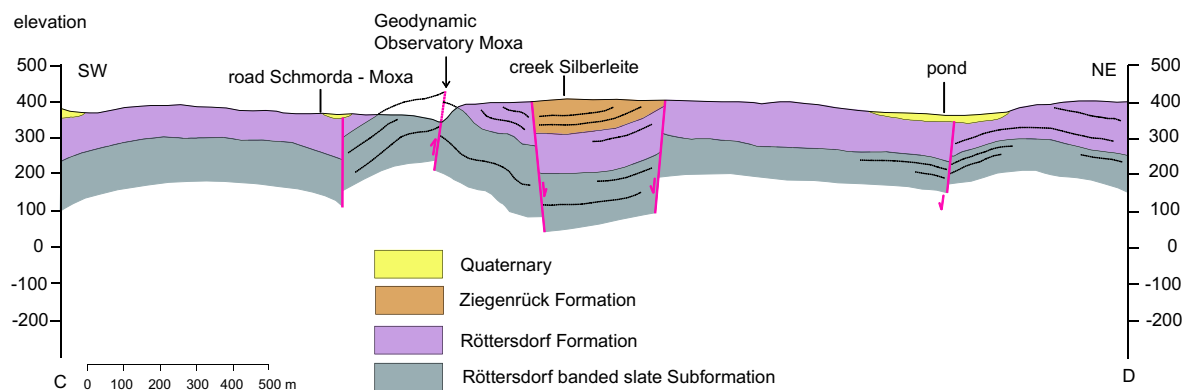


Figure 2.7: Geological southwest-northeast cut through the Moxa area following the CD line in Figure 2.5 (Kasch, 2006, modified).

The different geological units mentioned and the fold structure described are incorporated into the gravimetric model (Section 4). Relevant for the modelling are the folds of the 2nd and, partially, 3rd order – they are included into the gravimetric model.

2.4.4 Joints

Because the bedrock around the observatory is a joint aquifer (cf. Section 2.5) joints trace the way of the water from the surface into the subsoil. The joints dip almost vertically. According to their strike direction, they can be distinguished in

- dip joints striking north-northwest-south-southeast perpendicular to the fold axes and
- less frequent longitudinal joints (west-northwest-east-southeast) which are possibly connected to the foliation.

Both joint types were detected in sandstone-greywacke series of the Sonneberg Unit. Southeast-northwest striking dip joints also occur in the banded slates of the Leutenberg Unit.

2.4.5 Faults

Faults provide potential hydrological flow paths. Furthermore, if they dislocate rocks of different density, they may be visible in the Bouguer anomaly of the area and need to be considered in the gravimetric modelling.

Normal faults were mapped with strike directions varying between north-northeast–south-southwest and west–east (Figures 2.5, 2.6, 2.7). The widely northeast–southwest striking longitudinal faults are generally parallel to the foliation. They dip only a few degrees more steeply than the foliation (Schubert, 2005). These normal faults dislocate the rocks between a few and up to 150 m. The faults striking east–west to east-southeast–west-northwest are diagonal faults. However, they also can strike north–south causing conjugated shear rupture. Their dislocations can be deduced from stratigraphic information.

2.5 Hydrology

The headwater catchment of the creek Silberleite, in which Moxa observatory is located, covers an area of approximately $1.5 \times 1.5 \text{ km}^2$ and elevations between 450 m and 540 m above mean sea level. Nearly the whole catchment is covered by coniferous forest, and only very small parts in the west and east of the observatory are used for agricultural purposes (Figure 2.1).

The area is characterised by inhomogeneous subsoil. In Figure 2.8 an east–west profile of the Silberleite valley is shown which illustrates the hydrological situation and the relevant hydrological processes in the immediate observatory vicinity. The water is stored for short-, middle-, and long-term periods as soil moisture, joint water, ground water, and interception. During winter, water storage in form of snow occurs. Storage capacities are provided by the canopy, the disaggregated bedrock, the soil matrix, and the groundwater aquifer. Because of the specific topographic situation the water masses are located above and below the level of the gravity observation sites (Figure 2.8) and the aquifers are partially confined.

Rain water partially drains off on the surface, partially percolates into the fissured rock and is partially stored in the soil layer (Hasan et al., 2006; Kroner et al., 2007). Gravity changes observed with the superconducting gravimeter turned out to be correlated with hydrological variations (Section 3.2.2). Effects related to water level variations, soil moisture changes, and snow were found.

The topography plays an important role in the local interaction between hydrology and gravity at Moxa. To the east, directly next to the observatory building, a steep slope is located (Figure 2.8) which was identified as a gravimetrically significant hydrological compartment (Naujoks et al., 2008d). In the slope, interflow processes could be detected by experiments (Section 3.2.3). Rain water on this slope is mainly producing interflow with a quick response time of only a few hours (Kroner & Jahr, 2006). Nevertheless, the significance of effects by time-delayed flow processes in the steep slope is not clear yet. The extension of the local area which significantly influences gravity is also not known, and it needs to be determined

which of the hydrological contributors dominate in which frequency range.

The bedrock is very compact but has a strongly jointed top layer. The joints are mostly oriented vertically resulting in preferential flow paths for fast infiltration of subsurface water. Parts of the valley floor between the observatory and the creek Silberleite were filled up with debris during the construction of the observatory building and the gallery. This debris can be considered as an ideal and very permeable groundwater aquifer which drains water from/to the stream bed.

The soil types in the observatory surroundings were mapped in a field campaign resulting in a soil map (Scholten et al., 2004) which is based on more than 30 soil profiles. The soils are mostly cambisols with a partially significant clay fraction and a considerable rock fraction of about 30 % in the middle horizons and more than 70 % in the lower horizons. At the valley floor, groundwater influenced soils (gleysols) are found. For the entire area, 15 different soil types were identified and parameterised. The cambisols in the forest and the gleysols at the valley floor provide a hydrologically unsaturated and very permeable water storage with weathering/decomposition layer. It is underlain by strongly jointed as well as partially

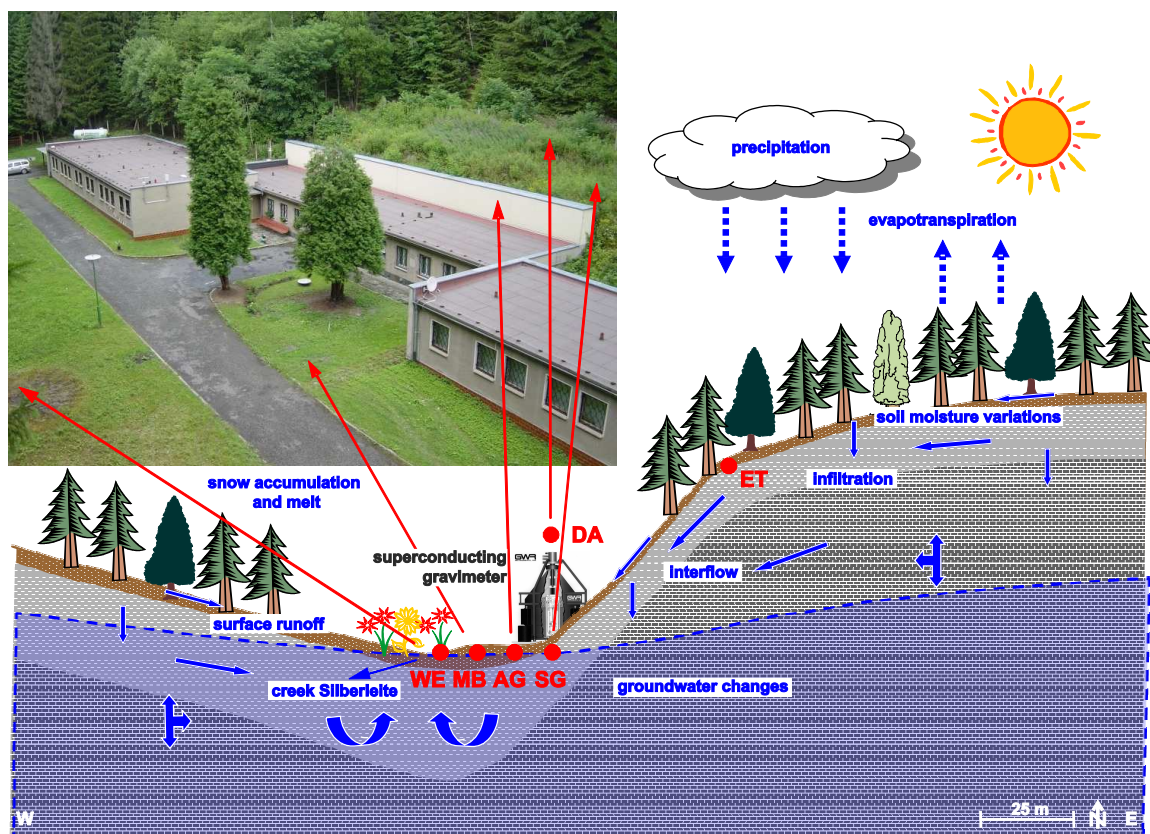


Figure 2.8: Sketch of the hydrological processes and flow paths at Moxa observatory, and location of the superconducting gravimeter and the observation points in the local gravity network MoxaNet (red points, Section 3.3).

faulted and weathered rock (disaggregated bedrock).

The meteorological conditions at the observatory are monitored every 10 s by measurements of the various hydrological and meteorological parameters mentioned in Section 2.3. The climate is humid with a mean annual temperature of 7.7°C based on the years from 2000 to 2006 and a mean annual rainfall of 733 mm. An actual evapotranspiration of 524 mm which was estimated using the equation of Penman-Monteith (Monteith, 1975) for potential evapotranspiration and considering the actual water content of the soil.

From hydrological research and modelling at Moxa (Krause et al., 2005, 2008; Hasan et al., 2006, 2008; Kroner et al., 2007) the conclusion could be drawn that the gravimeter signal shows variations which are correlated to various hydrological processes like rainfall, snow accumulation and melt, soil moisture changes, and changes in the groundwater. The influence of such hydrological changes on the gravity measurements has only been roughly investigated yet, because the interaction between hydrological state changes and gravity in general is complicated, because the geological and topographical situation is complex. One aim of this thesis is to quantify it in more detail.

3 Temporal gravity observations

3.1 Temporal variations in the gravity field

The earth's gravity field is affected by both spatial and temporal variations. Spatial variations are caused by the topography and an inhomogeneous density structure in the earth's body whereas temporal variations result from the fact that every mass change in or close to the earth and every deformation of the earth's body leads to a change in the gravity field. These mass changes can result from a number of effects which are briefly introduced:

- The *earth tides* provide the major influence in temporal gravity observations. They result from deformations of the earth's body which follow from the attraction between sun, moon, and earth as well as the rotation of these three celestial bodies around its common centre of mass. The earth tides amount to an amplitude of $\pm 1500 \text{ nm/s}^2$ maximum with periods mainly between 8 hours and one year (e.g. [Bartels, 1957](#); [Melchior et al., 1985a,b](#); [Dehant, 1987](#); [Hartmann & Wenzel, 1995](#); [Wenzel, 1996, 1997](#)).
- *Ocean tide loading effects* result from the ocean tides, commonly known as high and low tide. They go back to the same mechanism as the earth tides and mostly occur at the same frequencies. Ocean tide loading effects result from water mass shifts in the oceans which are related to the ocean tides, the resulting attraction changes, and the deformation of the earth's crust (e.g. [Farrell, 1972](#); [Baker, 1978](#); [Jentzsch, 1986](#); [Sun, 1992](#); [Jentzsch & Koß, 1997](#); [Jentzsch, 1997](#); [Jentzsch et al., 2000](#); [Zahran, 2000](#); [Zahran et al., 2006](#)).
- Changes in the *barometric pressure* occur at periods between minutes and years and reach an order of magnitude between a few nm/s^2 and up to 300 nm/s^2 , depending on the frequency range as well as the geographic position and elevation of the observation site (e.g. [Bullen, 1947](#); [Haurwitz & Cowley, 1973](#); [Warburton & Goodkind, 1977](#); [Merriam, 1992](#); [Crossley et al., 1995](#); [Sun, 1995](#); [Kroner, 1997](#); [Kroner & Jentzsch, 1999](#); [Boy et al., 2002](#); [Abe et al., 2008](#)).
- The earth can be excited to free oscillations by big earthquakes ($M > 6.5$). The periods of these oscillations are characteristic for the earth. They depend on the size, form, density and elasticity of the earth. *Free earth oscillations* are a global phenomenon. They originate from constructive interference of surface waves which run around the earth several times. The longest free earth oscillation period amounts to approximately 54 min, details are summarised by [Banka \(1993\)](#) and [Widmer-Schmidrig \(2003\)](#). Additionally, *earth's background free oscillations* are incessantly excited. The cause for these oscillations is under investigation, atmospheric turbulences or oceanic loading fluctuations are discussed (e.g. [Suda et al., 1998](#); [Nawa et al., 2000](#)).

- Gravity effects resulting from the earth's core:
 - The *free core nutation*, also called *nearly diurnal free wobble* is a free rotational oscillation of the system liquid outer core – lower mantle with a period close to one day (e.g. [Toomre, 1974](#); [Hinderer et al., 1982, 1991](#); [Florsch & Hinderer, 2000](#)).
 - The *inner core wobble* and the *free inner core nutation* are other resonance effects. The last mode lies in the diurnal band, as the free core nutation, but is a prograde mode, thus with a period larger than 1 day while the period of the free core nutation is smaller (e.g. [De Vries & Wahr, 1991](#); [Mathews et al., 1991a,b](#); [Dehant et al., 1993](#)). These effects could not be detected yet.
 - The frequencies and excitation mechanisms of *Slichter modes*, which are trans-lation oscillations of the solid inner core in the liquid outer core, are contro-versially discussed. These modes are theoretically predicted but not yet significantly detected (e.g. [Slichter, 1961](#); [Zürn et al., 1987](#); [Crossley & Rochester, 1992](#); [Smylie & Jiang, 1993](#); [Hinderer et al., 1995](#); [Courtier et al., 2000](#); [Smylie et al., 2001](#)).
- Temporal variations are observed in the angular velocity and the orientation of the earth rotation axis. The *polar motion* is a motion of the earth rotation axis relative to the earth's body. It reaches a peak-to-peak amplitude of several 10 nm/s^2 in gravity observations and comprises two main components: the *Chandler wobble*, a free oscillation of the earth with a period of about 432 days, and a forced annual oscillation (e.g. [Smith & Dahlen, 1981](#); [Wahr, 1985](#); [Fong Chao, 1993](#); [Furuya et al., 1996](#); [Furuya & Hamano, 1998](#); [Aoyama & Naito, 2000](#); [Harnisch & Harnisch, 2001](#); [Vicente & Wilson, 2002](#)).
- *Aperiodic gravity changes* can occur in an order of magnitude between a few nm/s^2 and several 1000 nm/s^2 . They are connected to relaxation processes like the Fenno-scandian land uplift ([Müller et al., 2005](#); [Steffen et al., 2008](#)) or tectonic movements like the plate movement e.g. in Iceland ([Torge & Kanngiesser, 1980](#)). During earth- quakes, *coseismic changes* may occur ([Imanishi et al., 2004](#)). At volcanoes gravity changes due to internal processes were observed ([Jentzsch et al., 2004](#)). Additionally, anthropogenic gravity changes due to the exploitation of oil and gas could be proved ([Drewes et al., 1983](#)).
- Finally, temporal gravity variations are caused by *hydrological changes*. These changes are the subject of this thesis; they are investigated and discussed in detail in the following sections.

3.2 Continuous observations with a superconducting gravimeter

Temporal variations in the earth's gravity field are monitored at Moxa observatory contin- uously with the stationarily operating superconducting gravimeter GWR CD034 for nearly

10 years now. This relative instrument is sensitive to the integral signal of mass shifts and vertical deformations in a period range between some seconds to several years. The measurements are continuous (1 s sample rate) and in contrast to measurements with other relative gravimeters nearly drift-free. They allow to monitor amongst others the influence of hydrological variations on the gravity field.

3.2.1 The superconducting gravimeter

The superconducting gravimeter, installed in 1999 at Moxa observatory (Jahr et al., 2001), is part of the world-wide network of such instruments (Global Geodynamics Project GGP; Crossley et al., 1999), in which variations of the earth's gravity field are monitored with an accuracy of better than one nm/s^2 .

The principle layout of the superconducting gravimeter consists of a Niobium sphere which levitates in a defined null position in a very stable magnetic field generated by superconducting coils. Whenever a mass change above or below the gravimeter occurs, the sphere moves in the direction of the mass increase. By a feedback system it is kept in the zero position. The voltage which is needed to keep it at the null position is recorded as a measure for the relative gravity change. The gravimeter at Moxa observatory is a dual sphere instrument. It has two in principle identical sensors. The upper sensor is placed approximately 20 cm above the lower sensor. The instrument's signal is calibrated by parallel recordings with absolute gravimeters.

As already mentioned, the gravimeter signal is affected by various influences such as tides, barometric pressure, polar motion, instrumental drift, and hydrology. In the following sections, all influences for which reduction models exist (earth and ocean tides, 3D barometric pressure (Abe et al., 2008), polar motion, instrumental drift) are eliminated from the recorded and calibrated data resulting in gravity residuals which are mainly affected by changes in hydrology.

3.2.2 Hydrological influences on the superconducting gravimeter data

At Moxa observatory hydrological variations caused by changes in the groundwater table and soil water content but as well as by precipitation events, snow cover and snow melt are significantly identified in the data of the superconducting gravimeter. They occur in an order of magnitude of a few nm/s^2 up to some 10 nm/s^2 both in a short periodic (minutes up to some days) and long periodic range (Kroner, 2001, 2002; Kroner et al., 2004, 2007).

Figure 3.1 gives an example for the hydrological influence for the period 00/04/18 to 00/05/03. A negative correlation between gravity residuals and water table observations is obvious: after rain events the water table increases whereas the residual gravity decreases. This negative correlation originates from the specific topographic location of the observatory: It is built at the base of a steep slope (cf. Figure 2.8), partially into a hill. Thus, most of the hydrological variations occur above the level of the gravimeter. This hydrological in-

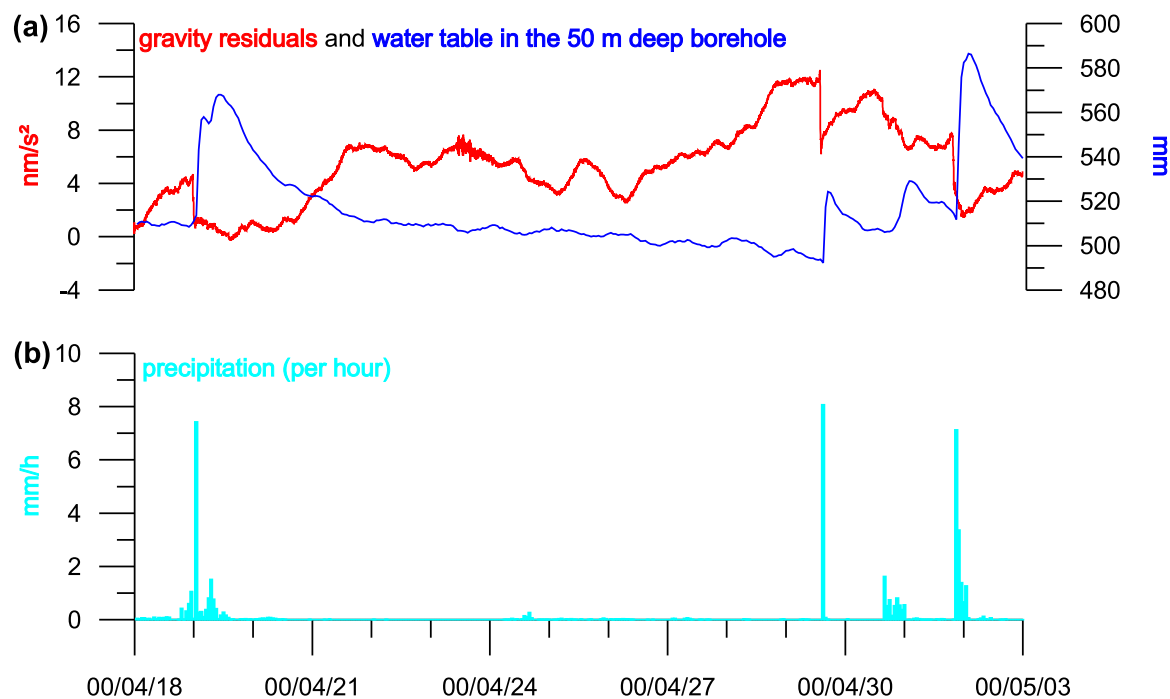


Figure 3.1: Hydrological influences on the superconducting gravimeter data at Moxa observatory; (a) gravity residuals and water table in the 50 m borehole; (b) precipitation (Kroner et al., 2004).

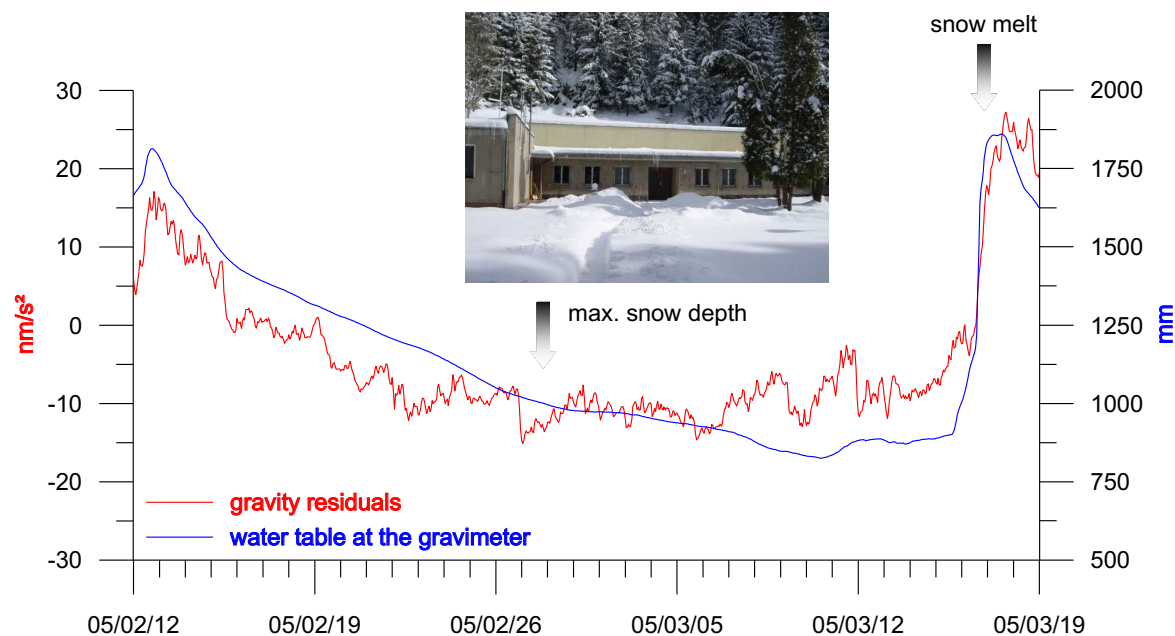


Figure 3.2: Influence of snow accumulation and melt on the observations with the superconducting gravimeter at Moxa. Shown are the gravity residuals and the water table at the gravimeter site (Kroner, 2006).

fluence is only partially compensated by soil moisture and water table fluctuations below the instrument. At rain events with successive high water table and soil moisture in the gravimeter surroundings, water mass is first stored above the gravimeter level, leading to a fast gravity decrease. While the water is moving downwards below the gravimeter level in the following hours and days, gravity slowly increases (Figure 3.1). Additionally, in the hours and days after a rain event up to 70 % of the rain water evaporate at Moxa, leading to a gravity increase as well.

An effect by snow can be detected as well: In Figure 3.2 an example of the influence of snow accumulation and melt is given. By a snowfall lasting some weeks a snow pack of approximately 0.5 m thickness was built up in winter 2005. It caused a gravity decrease between February and March 2005 of about 25 nm/s^2 . In March 2005 a rapid gravity increase of about 30 nm/s^2 within two days was observed, caused by the snow melt and the runoff of the melt water.

3.2.3 Experiments due to hydrological influences

To gain a better understanding of the hydrological effects observed in the gravity data, to identify the contributions from different areas, and to develop modelling approaches to reduce the hydrological signal from the gravity data, three experiments have been carried out in the surroundings of the superconducting gravimeter (Kroner, 2001, 2002; Kroner & Jahr, 2006). In each experiment a defined amount of water was added to a specific area and the resulting gravity change was observed. Water movement was monitored by different water level sensors (cf. Section 2.3).

3.2.3.1 First experiment: hydrological effects from the observatory roof

The first experiment was carried out to determine the influence of water mass changes in the observatory roof area which is located directly above the gravimeter (Kroner, 2001, 2002): Firemen of the auxiliary fire brigade Moxa irrigated the roof area with more than 17.6 m^3 water over a period of half an hour (Figure 3.3). On the assumption that no water runs off, the water volume corresponds to a water layer of 4 cm thickness on an area of 400 m^2 . Due to the additional water mass in the roof area above the gravimeter a gravity decrease of 11.5 nm/s^2 was observed with the lower sensor of the gravimeter (Figure 3.4), the upper sensor showed a decrease of 12.0 nm/s^2 . After the experiment gravity increased slowly. The whole decay period could not be observed because at the end of the experiment it started to rain and at night a big earthquake occurred which excited free oscillations of the earth.

By comparing the results of the experiment with typical gravity changes due to rainfall it turned out that the decrease in gravity usually observed due to rainfall is bigger and slower than the gravity decrease during the experiment even though it has been taken into account that a certain amount of water drained off immediately. These facts indicate that changes in the total hydrological regime in the wider surrounding area play an important role in the observed significant gravity changes. It is to be expected that a certain amount of water mass runs off closer to the gravimeter thus retarding the gravity decrease (Kroner, 2001).



Figure 3.3: First hydrological experiment on 99/09/29: Firemen irrigate the roof area of the observatory (Kroner, 2002).

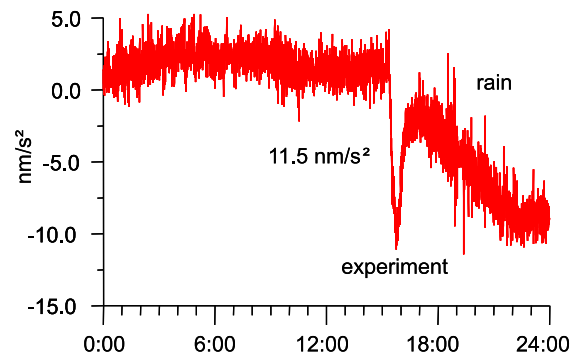


Figure 3.4: First hydrological experiment: changes in gravity residuals (lower sensor) caused by water mass variations in the roof area above the gravimeter (Kroner, 2001).

3.2.3.2 Second experiment: hydrological effects from underneath the observatory

To study the hydrological influence of water mass changes underneath the observatory 47 m^3 of water were injected into the gap between the pillar of the superconducting gravimeter and the floor over a time period of 9 hours (Kroner & Jahr, 2006). The arrival of the water front as well as the movement of the water in the artificial valley fill was monitored with four gauges in different distances to the gravimeter (Figure 3.5). The observed gravity effect (Figure 3.6) first results mainly from the water mass added almost directly below the gravimeter. The effect of water mass changes several meters away from the instrument becomes visible in the gravimeter data some minutes to hours later. The maximum gravity effect is about 10 nm/s^2 and corresponds to the maximum water level in the pillar gap. Two days after the experiment, the water level at 8 m distance from the gravimeter falls to zero (Figure 3.5).

For the reduction of the experiment-related hydrological effect in the gravity data (Figure 3.6) a combination of two hydrological sensors had to be used (Kroner & Jahr, 2006): The first represents the water level changes in the gap around the gravimeter pillar, the second in 8 m distance from the gravimeter. The effect was removed by applying two linear time-dependent regression coefficients on the time series. The time-dependency simulates the time-varying filling of the pore or joint volume.

This method of reduction is only required when water movement underneath the observatory with clear events is detected in the water level data. These near-field effects need to be removed from the data before the effect of contributions from a wider area can be studied.

3.2.3.3 Third experiment: influence of water movement in the hill slope

The gravity changes observed at Moxa in connection with rainfall (Section 3.2.2) indicate possible hydrological effects which occur several hours up to a few days after the rain event. The source for these gravity variations could be water movement downwards in the hill

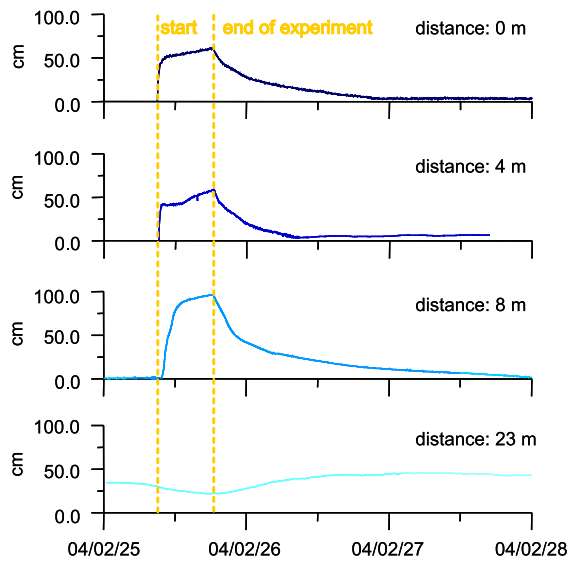


Figure 3.5: Second hydrological experiment: changes in the water table at four gauges due to water injection at the gravimeter pillar (Kroner & Jahr, 2006). The yellow line marks start and end of the experiment.

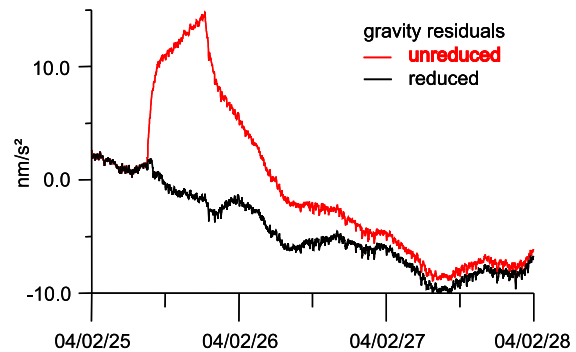


Figure 3.6: Second hydrological experiment: gravity variations due to water injection in the gap around the gravimeter pillar, and reduced gravity residuals (Kroner & Jahr, 2006).

behind the gravimeter site (cf. Figure 2.8). Another indication for this would be water found underneath the observatory and the associated flow path. In the third experiment, 20 m³ water were irrigated within 1 hour on a defined area of approx. 800 m² on the upper part of the eastern slope above the gravimeter (Figure 3.7). This is comparable with the mass of (very local) rain, as it occurs every 1–2 years (Kroner & Jahr, 2006). The resulting gravity effect is comparable with the gravity effect of the snow melt in spring.

The gravity and water table variations (directly at the gravimeter) after the experiment are given in Figure 3.8. A gravity decrease of about 2 nm/s² within the first 4 hours after the experiment was observed which was caused by the additional mass above the gravimeter. Six hours after the start of the experiment gravity began to increase to a total value of 8 nm/s².

The gravity change, caused by the experiment, was modelled by a waterfront moving downhill in the slope. Three flow paths were assumed (Figures 3.7 and 3.9): For flow path 2 a vertical movement of the water down to the level of the gravimeter is assumed. Flow path 3 runs on the basis of the disaggregated bedrock. Flow path 1 firstly

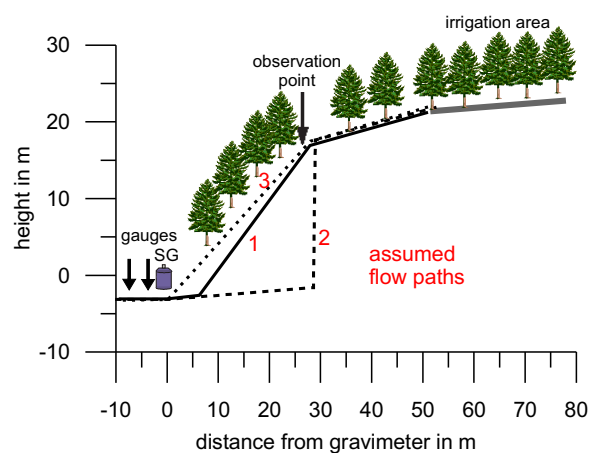


Figure 3.7: Third hydrological experiment: overview and water flow paths 1–3 for which gravity effects were computed (Kroner & Jahr, 2006).

follows the layer of disaggregated bedrock. Subsequently its slope angle increased when it runs down into the valley. For this case it is assumed that the water flows through joints in the rock. All 3 flow paths meet at the level of the superconducting gravimeter and the water runs off below the observatory into the creek Silberleite or into the valley floor. This is supported by the water table observations. The modelled gravity effect is given in Figure 3.9 (black lines). It turned out, that flow path 1 best matches the observations. Thus, in Moxa interflow in or below the disaggregated rock layer must occur through joints.

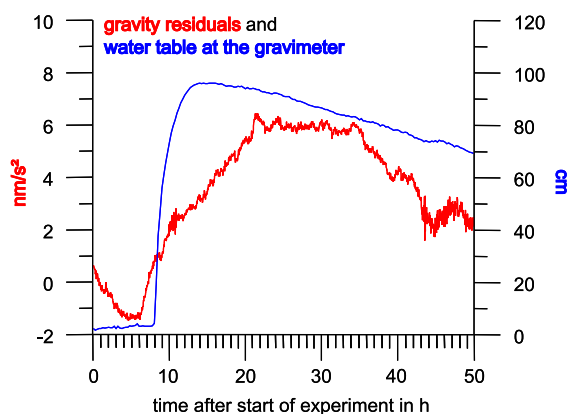


Figure 3.8: Third hydrological experiment: gravity variations and changes in the water table at the gravimeter (Kroner & Jahr, 2006).

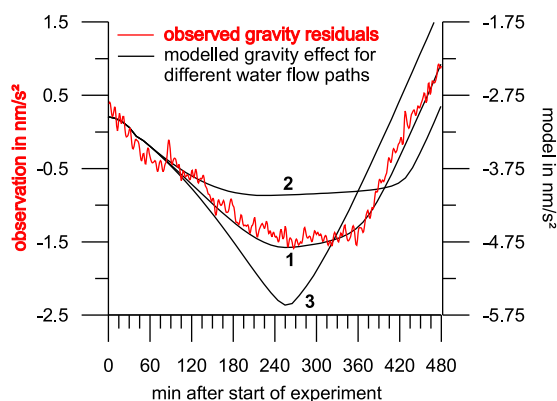


Figure 3.9: Third hydrological experiment: observed gravity variations for the first 8 hours after the experiment and modelled gravity effect for the different water flow paths (cf. Figure 3.7, Kroner & Jahr, 2006).

3.2.4 First attempts to model the local hydrological effect

From the experiments valuable information on the relationship between hydrological changes and gravity was derived. In a next step a first rough reduction for the hydrological influence was developed (Kroner et al., 2007).

From the meteorological and hydrological observations the gravity effects of soil moisture and water table variations as well as the effect of snow were modelled. Using elevation data the area up to a distance of 700 m from the SG was divided into cells of $5 \times 5 \text{ m}^2$. For each rectangular prism the effect of soil moisture variations and additionally for the valley bottom the effect due to water level changes was calculated (Nagy, 1966). For soil moisture fluctuations a layer of 1 m thickness divided into 10 cm thick layers was considered using soil moisture data from three different sites (valley bottom in front of the observatory, forest near top of the hill slope, and intermediate area) and two different depths (0.3 and 1 m). Between the two depths a linear change in soil moisture was assumed. For the computation of the gravity effect of water level changes a porosity of 25 % was assumed representing a mixture of gravel and loam. The lower boundary of the water-saturated zone was set to a depth of 2 m below surface as found by geoelectrical resistivity measurements. For simplification,

the water level variations obtained at the observation site directly in front of the observatory was applied in the calculation. The effect of water level variations in the direct vicinity of the gravimeter was computed applying the water level data from the site directly at the gravimeter and the reduction algorithm derived from the injection experiment (Section 3.2.3.2). The effect of snow was computed by accumulating precipitation for temperatures below 0°C. For temperatures above 0°C a simple snow melt model based on degree-days above a reference temperature was used (Chow, 1964; Bower & Courtier, 1998).

In Figure 3.10 the modelled effects of the different hydrological contributions, their total effect as well as unreduced gravity and gravity residuals reduced for hydrological effects are summarised for the period from 04/12/15 to 05/07/25. The total hydrological effect amounts to 35 nm/s² with soil moisture and water table effect partially compensating due to the hilly area. The hydrological reduction leads to a visible decrease in the peak-to-peak amplitude of the gravity residuals and in the general fluctuations. Nonetheless, a significant hydrological effect certainly remains in the gravity data. It was explained by inaccuracies in the modelling of the different hydrological contributions discussed above, but more important may be that changes in the amount of water stored in the hill slope are not yet taken into account. The total uncertainty due to these simplifications amounts to some nm/s². Due to the limited data time series of seven months a possible gravity effect related to seasonal hydrological variations – which is not reflected in the soil moisture or water table observations but could also amount to some nm/s² – is not taken into account here.

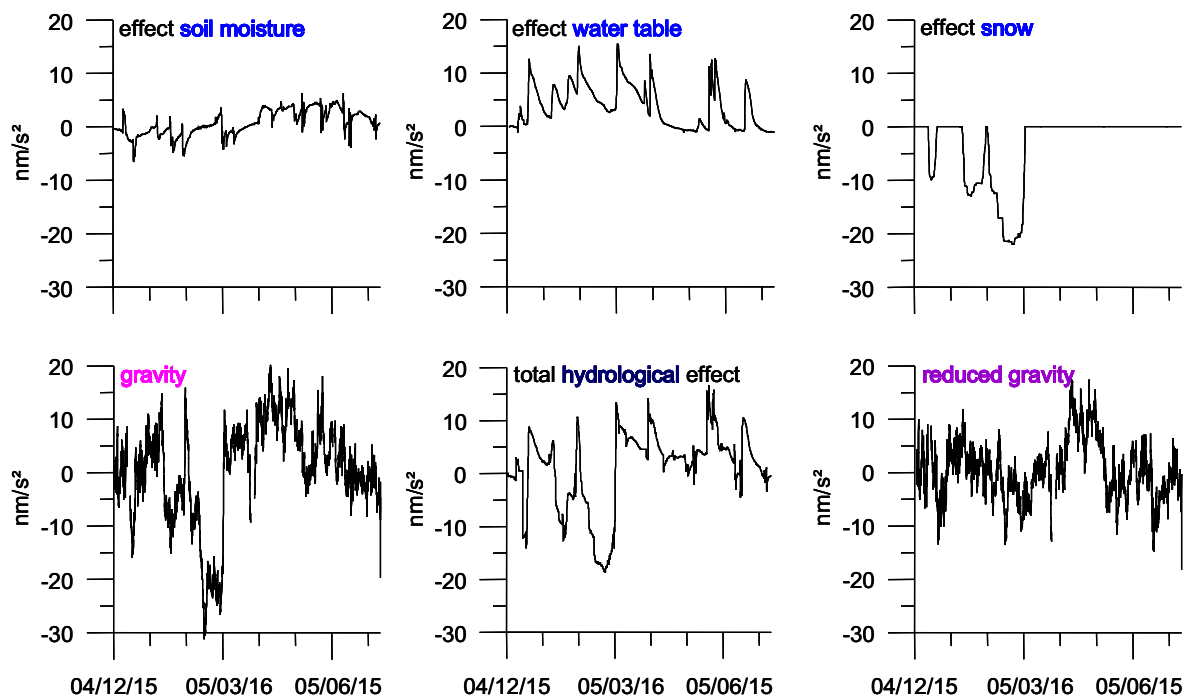


Figure 3.10: Gravity effect of different hydrological contributions, unreduced gravity, summarised local hydrological effect and gravity signals reduced for the local hydrological influence, hourly values, 04/12/15–05/07/25 (Kroner et al., 2007).

3.3 Repeated observations with L&R gravimeters

In addition to the stationary observations with the superconducting gravimeter, small-scale spatial gravity information is of interest to gain a broader knowledge about local hydrological processes acting in the surrounding of a superconducting gravimeter and to deduce constraints for hydrological modelling on a local scale.

With the only absolute gravimeter available for spatially distributed outdoor measurements, the A10, developed by Micro-g LaCoste, an accuracy of $\pm 50 \text{ nm/s}^2$ can be obtained (Liard & Gagnon, 2002), which is not sufficient to detect hydrological variations of some 10 nm/s^2 in gravity significantly. This leaves the only option of deploying classical relative instruments, which also have the advantage of being easily available.

Using relative instruments, Jentzsch et al. (2004) detected temporal gravity changes at the Mayon, Merapi, and Galeras volcanoes with a standard deviation of $\pm 100 \text{ nm/s}^2$ to $\pm 180 \text{ nm/s}^2$. The point distances were up to 20 km and the gravity range covered $750 \cdot 10^{-5} \text{ m/s}^2$ ($1 \cdot 10^{-5} \text{ m/s}^2 = 1 \text{ mGal}$). Ergintav et al. (2007) investigated temporal gravity changes due to postseismic deformations in the Marmara region, Turkey. They obtained accuracies of up to $\pm 100 \text{ nm/s}^2$ at point distances of several 10 km and a gravity range of some $10 \cdot 10^{-5} \text{ m/s}^2$.

Regarding the Fennoscandian land uplift, relative measurements were carried out on a network with point distances of some 10 km and a small gravity range of $0.5 \cdot 10^{-5} \text{ m/s}^2$ with standard deviations of some $\pm 10 \text{ nm/s}^2$ (Ekman et al., 1987). From several campaigns on local networks it is known that standard deviations between $\pm 10 \text{ nm/s}^2$ and $\pm 20 \text{ nm/s}^2$ can be achieved for one difference using several instruments in parallel (e.g. Vitushkin et al., 2002). Mäkinen & Tattari (1988, 1991) observed gravity variations related to hydrology with two relative gravimeters between two points with standard deviations of up to $\pm 13 \text{ nm/s}^2$ (point distance 2 km, gravity range 600 nm/s^2). During these measurements Mäkinen & Tattari (1991) showed that local hydrology-related gravity variations can change a gravity difference repeatedly measured with L&R relative gravimeters significantly.

This opens the possibility to derive information on local hydrological processes from spatially distributed gravity observations by repeated high-precision measurements. However, first the question needs to be answered whether or not it is possible to reach standard deviations of about $\pm 10 \text{ nm/s}^2$ on a local network, consisting of several points using relative gravimeters in repeated campaigns. If the answer is *yes*, spatially distributed gravity observations with relative instruments may lead to better, quantitative information on hydrological processes in the subsoil. They hold the potential to localise areas with a considerable hydrological influence on gravity.

3.3.1 Local gravity network MoxaNet

In the surroundings of Moxa observatory the gravity network MoxaNet was established. It consists of 12 observation points in distances up to 370 m (Figure 3.11) on massive concrete

pillars in hydrologically diverse areas (cf. Section 2.5). Coordinates and elevations of the points are given in Table 3.1. Nine points were installed on already existing pillars in and around the observatory, three pillars (for the points *MB*, *AN*, and *ET*) were newly built with a diameter of 0.3 m and a foundation depth of 1 m. On each pillar the gravimeter position and orientation to north is indicated. A measuring point for height control belongs to each observation site. The stability of the points was checked by repeated levelling in 5 campaigns. Significant height changes could not be found within the achieved accuracy of ± 1.5 mm. Therefore, the stability of the points is taken as better than ± 1.5 mm.

The points *TR*, *GA*, and *GR* are situated about 350 m south of the observatory building close to the GPS observation site, the points *PN* and *PS* are at the boreholes for the tiltmeter installation (cf. Figure 2.2). The point *AN* is situated to the east of the observatory, the pillar is mounted on the foundation of a former radio mast.

The six observation sites *SG*, *AG*, *MB*, *WE*, *DA*, and *ET* are located roughly on an east–west profile running perpendicular to the Silberleite valley in distances from a few up to 65 m (Figure 3.12). The maximum height difference between these points is 25 m, the maximum gravity difference is $4.42 \cdot 10^{-5} \text{ m/s}^2$. The point *ET* is situated on the hill to the east of the observatory near the top of the steep slope (Figure 2.8), a second point (*DA*) on the soil-

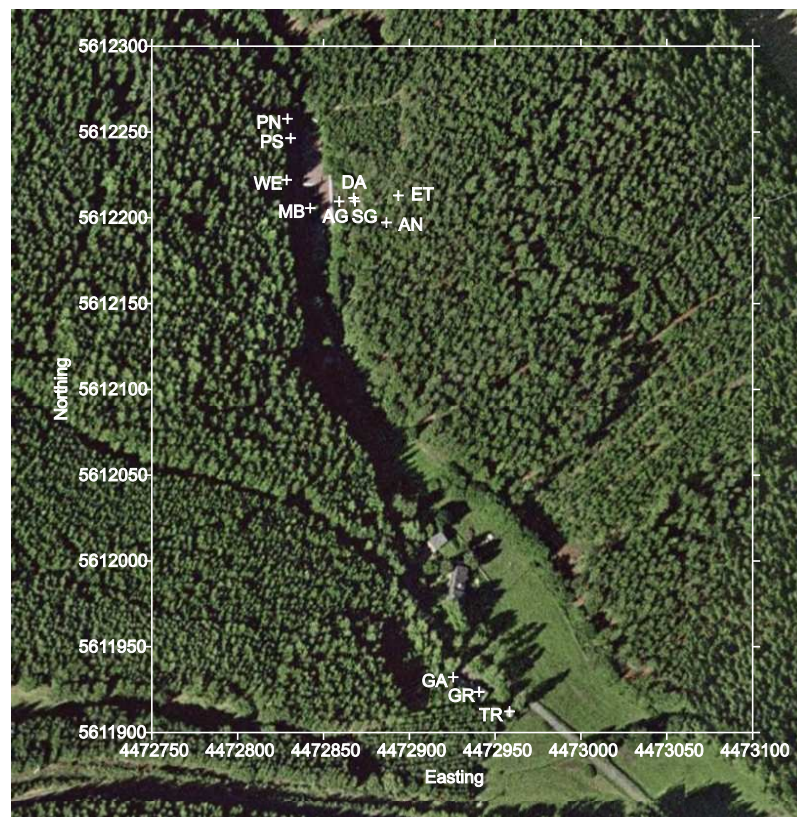


Figure 3.11: The 12 observation points of the local gravity network MoxaNet at the Geodynamic Observatory Moxa. The aerial photograph was taken from [Google Earth \(2008\)](#).

Table 3.1: Coordinates and elevation of the observation points in the local gravity network MoxaNet (reference system PD83). The first 6 points are on the profile shown in Figure 3.12.

Observation point	Easting	Northing	Elevation in m
SG	4472867.617	5612211.545	455.083
AG	4472859.164	5612209.568	455.072
MB	4472842.278	5612205.694	454.176
WE	4472828.539	5612222.150	454.433
DA	4472868.357	5612209.611	461.098
ET	4472893.583	5612213.013	479.550
PN	4472829.052	5612257.757	455.458
PS	4472830.839	5612246.414	454.917
AN	4472886.682	5612197.281	475.478
GA	4472940.694	5611923.657	445.979
GR	4472925.560	5611932.235	446.271
TR	4472958.359	5611912.255	444.255

covered roof of the observatory building. Another point *SG* is next to the superconducting gravimeter in the observatory building, about 6 m below point *DA* at the base of the steep slope. Hence, the results of the repeated measurements can be compared to the data of the superconducting gravimeter and interpreted jointly. Three more sites (*AG*, *MB*, *WE*) are situated in the valley in increasing distances to the superconducting gravimeter. Besides point *SG* also point *AG* is located inside the observatory building, the points *MB* and *WE* outside, the point *WE* next to the Silberleite creek in an almost permanent saturated area.

For the measurements three to five L&R relative gravimeters (G085, G858, D187, G662, and G896) were used. The instruments G896 and D187 belong to the Friedrich-Schiller-University Jena. The gravimeters G085 and G858 were lent from the Technical University Berlin, the G662 from the Leibniz Institute for Applied Geosciences Hanover. All gravimeters are equipped with an electronic feedback system and the instruments G662, G896, and D187 with electronic levels.

Measurements were carried out over a period of 35 months between November 2004 and September 2007 in 19 campaigns (lasting 2 or 3 days; Table 3.3) in a seasonal rhythm as well as at special hydrological events (snow melt, heavy rain, dryness; Figure 3.17). For the measurements, the step method (Torge, 1989) was applied. The points *SG*, *AG*, and *MB* were connected to a triangle; and each of the stations *WE*, *DA*, and *ET* was connected to two or three points of this triangle. Each observed gravity difference was measured at least five times with each gravimeter. Using four gravimeters, 20 ties minimum were measured between two points. Each single observation is the arithmetic mean of three gravimeter read-

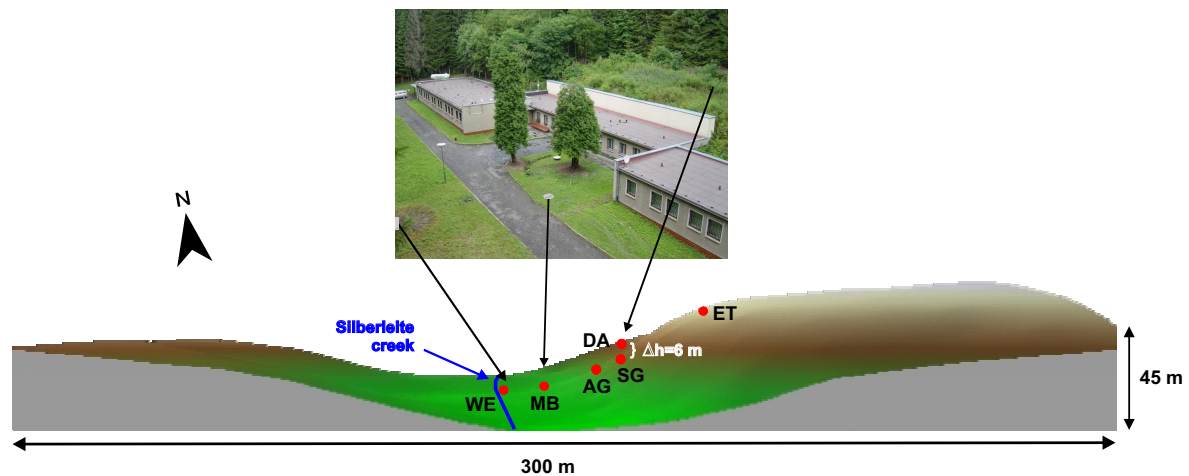


Figure 3.12: Location of the gravity observation sites on the east–west profile in the MoxaNet.

ings at different dial positions and with three different feedback readings, all close to zero (cf. Section 3.3.2). This results in a well configured network with approximately 200 observed gravity differences for each campaign.

3.3.2 Instrument calibration

From long experience, the instruments used are known to be robust and of high accuracy with low and stable drift rates (Kanngieser et al., 1983; Atzbacher & Gerstenecker, 1993; Jentsch et al., 2004; Ergintav et al., 2007). Regarding the desired accuracy of $\pm 10 \text{ nm/s}^2$, the calibration, their stability, and systematics of the instruments are essential. Systematic instrument-specific errors can only be minimised by using several gravimeters in parallel. Furthermore, uncertainties in the calibration can be reduced.

At the vertical gravimeter calibration line Hanover, Germany (Kanngieser et al., 1983; Timmen & Gitlein, 2004), periodic dial calibration terms as well as linear and quadratic feedback calibration terms were determined for the gravimeters used. Linear calibration factors of the dial were checked on the Hanover–Harz calibration line, which covers the gravity range of MoxaNet. These calibration factors, shown in Table 3.2, were used additionally to the calibration given by the manufacturer.

Regarding the accuracy of $\pm 10 \text{ nm/s}^2$ striven for and the gravity range of the MoxaNet ($4.42 \cdot 10^{-5} \text{ m/s}^2$), linear calibration factors need to be stable within $1 \cdot 10^{-4}$. The stability of the linear calibration factors of the instruments has been proved over decades in campaigns carried out by Kanngieser et al. (1983), Atzbacher & Gerstenecker (1993), Jentsch et al. (2004), and Ergintav et al. (2007). This is valid in general on the condition that no bigger repairs were made at the instruments. Furthermore, the calibration values obtained on the Hanover–Harz line at different campaigns were compared with each other. Changes larger than $1 \cdot 10^{-4}$ could not be detected.

Periodic calibration terms arise from the mechanical construction of the instruments, in particular from not exactly centrically mounted gearwheels. The periods were determined by [Kiviniemi \(1974\)](#). From long experience, these terms are known to be stable with time as long as the gravimeter is not modified. In contrast, the calibration factors of the feedback system may change with time. Therefore, in the MoxaNet, all feedback readings were done with feedback values around zero (± 20 mV). Thus, the influence of possible instabilities in the feedback calibration on the observations in the MoxaNet is negligible.

Table 3.2: Calibration terms of the L&R gravimeters used for the dial and feedback system.

Gravimeter	Dial				Feedback	
	Linear term	Periodic terms			Linear term	Quadratic term in 10^{-6}
		Period in CU	A in nm/s^2	ϕ in $^\circ$		
G085	1.001700	1.0000	18 ± 11	302 ± 32	1.05966	0.6570
	± 0.000036	3.9400	13 ± 7	240 ± 36	± 0.00030	± 0.0143
		7.8800	70 ± 7	200 ± 7		
G858	1.000630	1.0000	17 ± 12	145 ± 42	1.06324	0.2310
	± 0.000112	3.6700	30 ± 13	19 ± 21	± 0.00044	± 0.0257
		7.3300	26 ± 10	295 ± 21		
D187	0.995662	0.7220	21 ± 6	232 ± 18	1.11899	0.2624
	± 0.000144	1.6250	72 ± 5	103 ± 5	± 0.00019	± 0.0094
		3.2500	48 ± 8	212 ± 8		
G896	1.000559	1.0000	59 ± 18	119 ± 20	1.04028	-0.4069
	± 0.000036	3.6700	43 ± 21	50 ± 28	± 0.00036	± 0.0156
		7.3300	151 ± 19	327 ± 7		
G662	1.000789	1.0000	67 ± 20	66 ± 14	1.02682	-0.1985
	± 0.000066	3.6700	64 ± 10	47 ± 9	± 0.00022	± 0.0101
		7.3300	31 ± 11	175 ± 21		

3.3.3 Least squares adjustment

The data were analysed by least squares adjustment using the software package GRAVNA ([Wenzel, 1993](#)). The least squares technique takes into account all observations evenly or with predefined weights to compute the unknowns ([Großmann, 1969](#)). This leads to consistent results and provides an insight into the scale and the distribution of the discrepancies among the observations. The residual equation for one gravity difference measured with one

gravimeter is given by [Kanngieser et al. \(1983\)](#) and [Wolf \(1997\)](#)

$$v_{i,j} = (\bar{g}_i - \bar{g}_j) - (g_i - g_j) + D(t_i - t_j) \quad (3.1)$$

with the adjusted gravity difference $(\bar{g}_i - \bar{g}_j)$ between the stations i and j , the observed gravity difference $(g_i - g_j)$ between i and j , a linear drift coefficient D over the observation time $t_i - t_j$, and the residual $v_{i,j}$.

The observed gravity difference $(g_i - g_j)$ was computed by converting the gravimeter readings z_i and z_j into gravity values g_i and g_j using firstly the calibration table provided by the manufacturer and correcting the influence of atmospheric pressure by the factor 3.3 nm/s^2 per hPa and earth tides using the tidal potential development from Cartwright-Tayler-Edden 1973 ([Cartwright & Edden, 1973](#)). Additionally, the calibration terms, determined at the gravimeter calibration system Hanover (Section 3.3.2), were applied to the dial readings. These are a linear calibration term $E_1(z_i - z_j)$ and the periodic calibration terms

$$\sum_{n=1}^p X_n \left(\cos \frac{2\pi z_i}{T_n} - \cos \frac{2\pi z_j}{T_n} \right) \quad (3.2)$$

and

$$\sum_{n=1}^p Y_n \left(\sin \frac{2\pi z_i}{T_n} - \sin \frac{2\pi z_j}{T_n} \right) \quad (3.3)$$

with the parameters $X_n = A_n \cdot \cos \phi_n$, $Y_n = A_n \cdot \sin \phi_n$, and $A_n = \sqrt{X_n^2 + Y_n^2}$. In Equations (3.2) and (3.3) n is the number of the periodic calibration term, p the number of the periods to be corrected, A the amplitude, ϕ the phase, and T the period in counter units (CU, Table 3.2).

To the feedback readings of each gravimeter a linear and a quadratic calibration term was applied (Table 3.2). Finally, the observed gravity differences of all gravimeters entered the least squares adjustment.

Because hydrological variations were expected at all observation points, no point could be fixed in the least squares adjustment. Therefore, a free network adjustment was made for each campaign. The unknowns of the system were the linear drift coefficients of the gravimeters and the gravity values of the stations from which the gravity differences were calculated. A linear drift coefficient was adjusted for each gravimeter and for each campaign. The results obtained were the adjusted gravity differences with standard deviations for each campaign. For further interpretation the temporal changes of these gravity differences were considered.

3.3.4 Results of the repeated gravity campaigns

3.3.4.1 Accuracies and test measurements

The standard deviation m_0 for one single observation obtained in the adjustment of the observations of all gravimeters varies between $\pm 54 \text{ nm/s}^2$ and $\pm 88 \text{ nm/s}^2$ (Table 3.3). Besides the m_0 of the combined adjustment, the standard deviation m_0 of a single observation with

Table 3.3: Standard deviations in nm/s^2 for the L&R gravimeters used derived from the least squares adjustment for each campaign.

Campaign No.	Date yyyy/mm/dd	L&R gravimeter							
		G085 m_0	G858 m_0	D187 m_0	G662 m_0	G896 m_0	Combined m_0 m_g $m_{\Delta g}$		
1	2004/11/17–29	49	72	97	118	141	68	13	19
2	2004/12/09	-	77	-	98	91	87	22	31
3	2004/12/16	37	-	-	109	117	88	14	20
4	2005/01/06	22	-	-	96	110	64	8	12
5	2005/03/18–20	49	55	47	-	131	73	8	12
6	2005/07/14–15	55	62	64	-	70	61	7	10
7	2005/08/24–25	53	53	73	73	-	63	7	10
8	2005/09/28–29	42	61	43	73	-	58	6	9
9	2006/02/17–19	34	87	46	85	-	70	6	9
10	2006/04/05–06	57	70	65	65	-	67	8	12
11	2006/05/16–17	37	66	47	-	85	54	9	13
12	2006/08/14–16	33	95	74	-	-	80	9	13
13	2006/09/11–12	30	73	77	-	99	75	7	10
14	2006/11/10–11	85	90	74	-	-	84	10	14
15	2007/01/12–16	46	76	69	-	-	69	8	12
16	2007/02/26–27	50	83	73	-	-	76	9	13
17	2007/04/23–24	40	80	80	-	-	66	9	13
18	2007/08/22–28	38	52	70	-	-	54	7	10
19	2007/09/12–13	33	84	68	-	-	87	9	13

(m_0 , standard deviation of one single observed gravity difference; m_g , standard deviation of the gravity values at the stations; $m_{\Delta g}$, standard deviation of an adjusted gravity difference; note: campaigns 1–4 comprise the test phase)

each gravimeter used is also shown in Table 3.3 for each campaign. Statistically insignificant observations (outlier criterion: $> 3 \cdot m_0$) were removed from the data.

In the first four campaigns of the repeated measurements the standard deviation $m_{\Delta g}$ of an adjusted gravity difference varies from $\pm 12 \text{ nm/s}^2$ to $\pm 31 \text{ nm/s}^2$. Thus, the standard deviation m_g of a gravity value at the stations is between $\pm 8 \text{ nm/s}^2$ and $\pm 22 \text{ nm/s}^2$. These standard deviations obtained for the first four campaigns of the repeated measurements were too large to detect hydrological variations of a few 10 nm/s^2 significantly. To increase accuracy, extensive tests were carried out:

- From the comparison of the standard deviations m_0 of one single observation for the different L&R gravimeters follows that the gravimeters G085, G858, and D187 are the best high-precision instruments (Table 3.3). The G662 also has a fairly small m_0 , but was not always available when needed. The G896 is less suitable for these high-precision repeated measurements. Therefore, in the following campaigns mainly the instruments G085, G858, and D187 were used.
- In the first four campaigns different network configurations were tested in order to achieve the best results regarding accuracy and effective measuring regime. In these campaigns measurements were not always carried out at the points *WE* and *DA*. In the following campaigns these points were always included into the network to achieve a better network conditioning.
- Tests at three campaigns showed that for the gravity differences to the points *PN* and *PS* at the tiltmeter boreholes deviations between the gravimeters of up to 1460 nm/s^2 occurred. This indicates that at these points an influence on the gravimeter readings exists which is different for each instrument. Geomagnetic measurements in the vicinity of the points showed anomalies in the magnetic total field of up to 5600 nT at the tiltmeter boreholes. These anomalies are artificial, they were obviously caused by the cover plate and the steel casing of the boreholes. Because an influence of the magnetic field on L&R gravimeter readings is known (Pálinkáš et al., 2003; Forbriger, 2007), these anomalies may have caused the deviations between the instruments. Consequently, no further gravity measurements were carried out at the points *PN* and *PS*.
- At the point *AN*, mounted on the foundation of a former radio mast, measurements could be carried out only in dry weather conditions. At wet weather conditions the surroundings of the point become very slippery, more than expected when the point was built. This is dangerous as the point is situated directly at the escarpment of the steep slope east of the observatory. For this reason and because this point is located close the point *ET* (cf. Figure 3.11), it was not used anymore in the gravity campaigns.
- A simple model was used to get a first rough estimate of the hydrological effects to be expected at the various observation points. It includes a soil layer (thickness 1.5 m, porosity 25 %), the disaggregated bedrock (thickness 15 m, porosity 2 %), and the topography in the observatory surroundings (Section 4). A change from a very wet to a dry situation was considered as maximum estimation (e.g. between a campaign at snow melt and in dry summer). The volumetric soil water content was assumed to decrease by 5 % for the soil layer, and 2 % for the disaggregated bedrock.

From the results a gravity increase of 38 nm/s^2 for the point *SG*, and a gravity decrease of 22 nm/s^2 for the point *MB* and 89 nm/s^2 for the point *ET* was derived. To describe $|g_{SG} - g_{ET}|$ – the absolute value of the difference g_{SG} minus g_{ET} , the expression *SG-ET* is used, also for all other differences in the network. In the calculations for the MoxaNet, always the locations with higher gravity values entered the difference as minuend, and the stations with lower gravity values as subtrahend. Therefore, the difference *SG-ET* increased by 127 nm/s^2 , the difference *MB-ET* by 67 nm/s^2 , and the

difference $MB-SG$ decreased by 60 nm/s^2 . From this estimate it can be inferred that gravity changes in an order of magnitude of larger than 100 nm/s^2 may occur in the gravity differences. The largest effects are to be expected between points in the valley and the higher located points due to their different hydrological situation.

- Certain hydrological events like snow melt or heavy rain last only a few days or less. To catch these events in the repeated campaigns the gravity network needs to be covered within a few days; the observation campaign needs to be completed before the hydrological situation changes. The tests showed that the gravity differences between the six observation points WE , MB , AG , SG , DA , and ET on the profile (cf. Figure 3.12) could be covered within two days. To include the points GA , GR , and TR into the network takes two additional days because of a longer transportation time for the instruments of about 15 to 20 min to these points and the number of additional observations. Due to this reason and the results of the first rough modelling, discussed in the last point, the stations GA , GR , and TR were excluded from the network. The measurements were restricted to the six points along the profile running perpendicular to the topography (Figure 3.12). Thus, it had to be accepted not to gain information on hydrological changes occurring north–south in the Silberleite valley, which surely have a smaller amplitude than the changes perpendicular to the valley, but probably exist.
- The gravity differences from the points within the valley to the point ET at the steep slope are the largest in the MoxaNet. Furthermore, the transportation of the instrument to the point ET takes approximately 15 min, between the points in the valley less than 5 min. Therefore, the differences to the point ET are affected by the largest errors. To counter this, the number n of observed gravity differences ($g_i - g_j$) from points in the valley to the point ET was increased from 10 to 14.
- During the tests in the first four campaigns occasionally a lower number of gravity differences than described in Section 3.3.1 was measured (2–3 instead of 5–7 between two points). This partially could have caused the lower accuracies in the first phase of the measurements. The observation scheme described in Section 3.3.1 turned out to be best suited; it was used in the campaigns 5–19.
- A shock-free transportation of the gravimeters to the point ET on the hill is difficult because of rugged and sometimes slippery ground at the steep slope. To shorten transportation time to the point ET and to ensure a shock-free transport (for reducing drift rates and avoiding jumps) a lift was built for gravimeter transportation from the observatory to the point ET (Figures 3.13 and 3.14).
- Highest accuracies were obtained if always the same well-versed persons observed the gravity differences, each person always with the same gravimeter.
- The least squares adjustment was done with and without consideration of periodic dial calibration terms. The results with higher accuracy were obtained when periodic terms had been taken into account.



Figure 3.13: Gravimeter lift: lower station in the valley at the observatory building.



Figure 3.14: Gravimeter lift: upper station on the hill east of the observatory close to the point *ET* of the MoxaNet.

Considering these findings, in the subsequent campaigns the standard deviation $m_{\Delta g}$ of an adjusted gravity difference ranges between $\pm 9 \text{ nm/s}^2$ and $\pm 14 \text{ nm/s}^2$. Thus, the standard deviation m_g of a gravity value at the stations is between $\pm 6 \text{ nm/s}^2$ and $\pm 10 \text{ nm/s}^2$ (Table 3.3). It is within the order of magnitude of the hydrologically caused gravity variations observed with the superconducting gravimeter (Section 3.2). Therefore, it is possible to significantly observe and investigate these variations with L&R instruments.

3.3.4.2 Scattering of the individual measurements in the least squares adjustment

The scattering of the observed, drift-reduced gravity differences ($g_i - g_j$, cf. Equation 3.1) and the temporal changes between the campaigns are given in Figures 3.15 and 3.16 for each L&R gravimeter, and for all observed gravity differences between the points *SG*, *AG*, *MB*, *WE*, *DA*, and *ET*. For better comparison, a mean value was subtracted from the differences. Generally, in the first four campaigns the scattering was larger than in the following campaigns due to changes in the network design and the selection of the instruments (Section 3.3.4.1). Between most campaigns the changes obtained with the different gravimeters fit well together – they point in the same direction and are in the same order of magnitude. This is one prerequisite to achieve reliable results in the combined adjustment. Significant temporal changes could not be proved in the individual differences, but between some campaigns tendencies were identified:

Between campaigns 5 and 6, as well as 12 and 13 an increase of about 100 nm/s^2 was observed in the differences *SG-ET*, *AG-ET*, and partially *MB-ET* with all gravimeters (Figure 3.15 a–c). Between the campaigns 10 and 11 and partially between the campaigns 11 and 12 an increase was identified in these differences as well (the difference *SG-ET* was not observed during campaign 11). Between campaigns 8 and 9 the differences *SG-ET*, *AG-ET*, and *MB-ET* decreased by about 100 nm/s^2 as observed by all gravimeters.

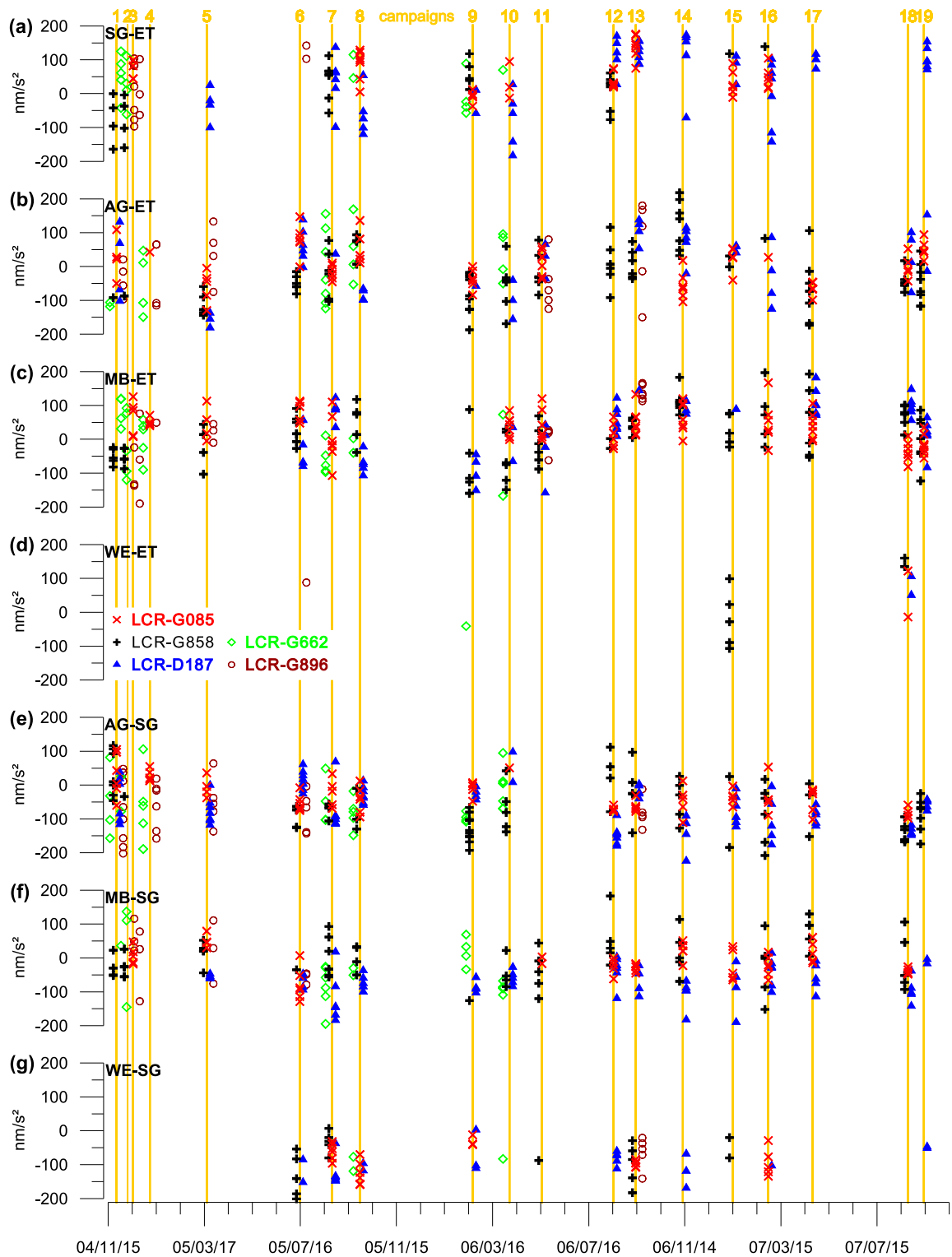


Figure 3.15: Scattering of the observed drift-reduced gravity differences ($g_i - g_j$) and temporal changes between the campaigns for each L&R gravimeter used; gravity difference between the points (a) *SG-ET*, (b) *AG-ET*, (c) *MB-ET*, (d) *WE-ET*, (e) *AG-SG*, (f) *MB-SG*, and (g) *WE-SG* (cf. Table 3.3 and Figure 3.12); mean value reduced; campaigns 1–4: test phase.

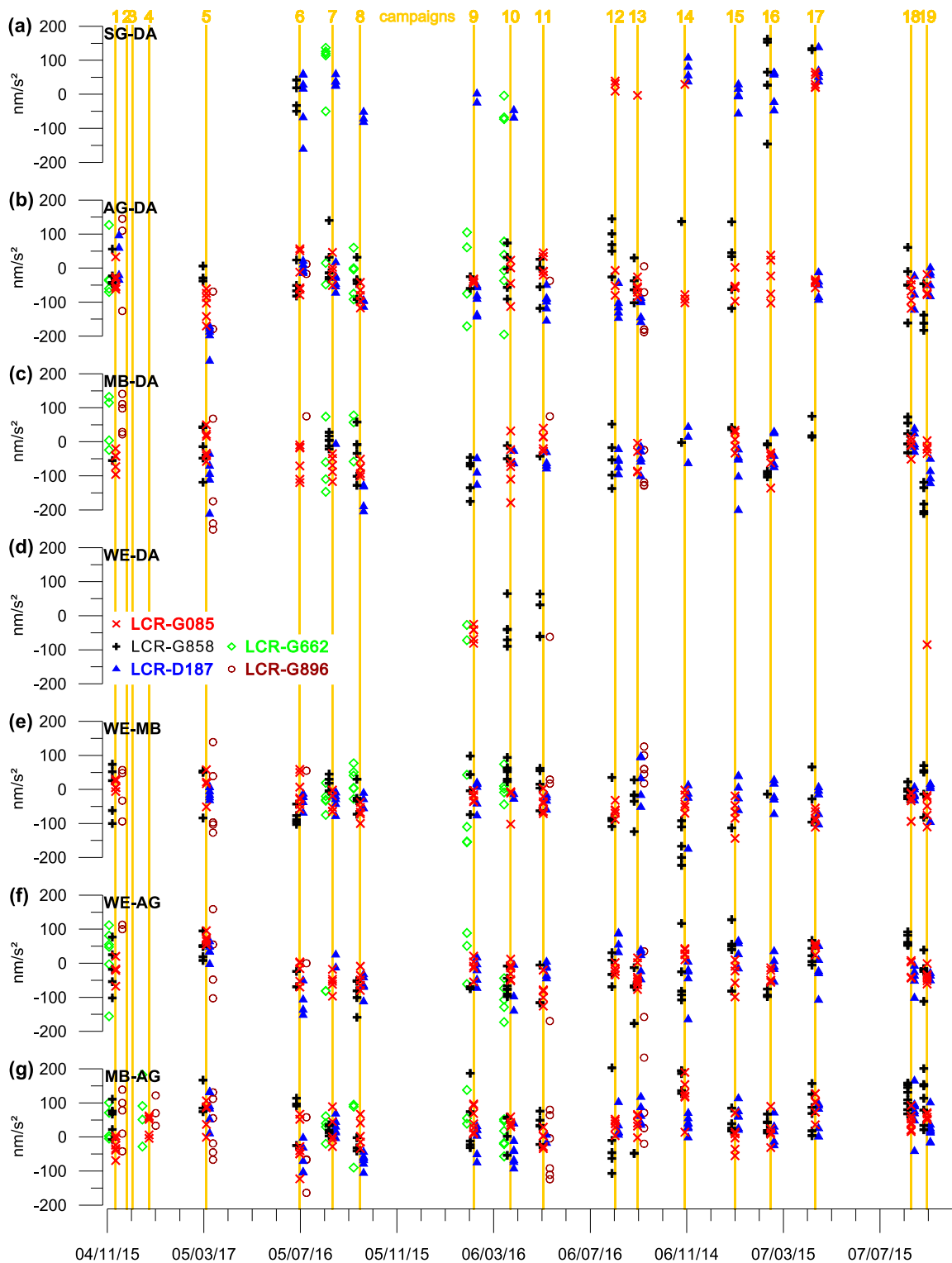


Figure 3.16: Scattering of the observed drift-reduced gravity differences ($g_i - g_j$) and temporal changes between the campaigns for each L&R gravimeter used; gravity difference between the points (a) *SG-DA*, (b) *AG-DA*, (c) *MB-DA*, (d) *WE-DA*, (e) *WE-MB*, (f) *WE-AG*, and (g) *MB-AG* (cf. Table 3.3 and Figure 3.12); mean value reduced; campaigns 1–4: test phase.

In the differences between the points *SG*, *AG*, *MB*, and *WE* in the observatory valley and point *DA* on the roof (Figure 3.16 a–d) changes were identified as well. However, these changes mostly are not homogeneous. Whereas the difference *AG-DA* (Figure 3.16 b) increased between the campaigns 5 and 6, the difference *MB-DA* (Figure 3.16 c) decreased. Between campaigns 8 and 9 an increase in the gravity difference *MB-DA* of about 60 nm/s^2 was measured with the instrument D187, the results from gravimeter G858 show a decrease of about 30 nm/s^2 .

Despite the very small gravity differences between the points within the valley (Figures 3.15 and 3.16 e–g), in these differences temporal changes could be identified as well. As in the differences to the point on the observatory roof, they have, however, partially opposite tendencies. For instance, between the campaigns 5 and 6 a decrease in the differences *MB-SG*, *WE-AG* and *MB-AG* of about 80 nm/s^2 was observed by all gravimeters (Figure 3.15 f and 3.16 f–g), whereas in the difference *WE-MB* (Figure 3.16 e) almost no changes were detected, also between the other campaigns. In the difference *AG-SG* the changes were partially not homogeneous between campaigns 5 and 6. With the instrument D187 an increase of about 90 nm/s^2 , with the G085 a decrease of about 60 nm/s^2 , and with the G896 no changes were measured. Thus, from the scattering of the individual measurements here no information can be derived.

In the differences to the point on the hill (Figure 3.15 a–d) or to the observatory roof (Figure 3.16 a–d), the scattering is by the factor 1.5 higher than in the differences between stations within the Silberleite valley. This is due to the larger gravity differences and the longer transportation time to the points *ET* and *DA* (Section 3.3.4.1). The differences *WE-ET* and *WE-SG* (Figure 3.15 d, g) as well as *SG-DA* and *WE-DA* (Figure 3.16 a, d) were measured additionally to the other differences but not at all campaigns. From these differences alone no results could be derived. However, they provide valuable ties in the network which constrain and improve a combined least squares adjustment, where all observations are considered.

As mentioned previously, all variations in the drift-reduced gravity differences are tendencies, no significant changes. Significant and reliable results were derived by a combined adjustment of the complete network with all gravimeters used.

3.3.4.3 Combined least squares adjustment

The results of the repeated observations after the combined least squares adjustment including all gravimeters and all observation points are shown in Figure 3.17. Besides the temporal changes in the adjusted gravity differences with standard deviation (Figure 3.17 a–c), variations of some hydrological parameters are also given (Figure 3.17 d–g).

As mentioned in Section 3.3.4.1, the standard deviation obtained for one adjusted gravity difference at one campaign $m_{\Delta g}$ varies from $\pm 9 \text{ nm/s}^2$ to $\pm 14 \text{ nm/s}^2$ after the test phase, and for changes in one gravity difference between two campaigns from $\pm 13 \text{ nm/s}^2$ to $\pm 20 \text{ nm/s}^2$ (Table 3.3, Figure 3.17 a–c). Hence, changes in the gravity differences larger than twice the standard deviation, which is between $\pm 26 \text{ nm/s}^2$ and $\pm 40 \text{ nm/s}^2$, are significant.

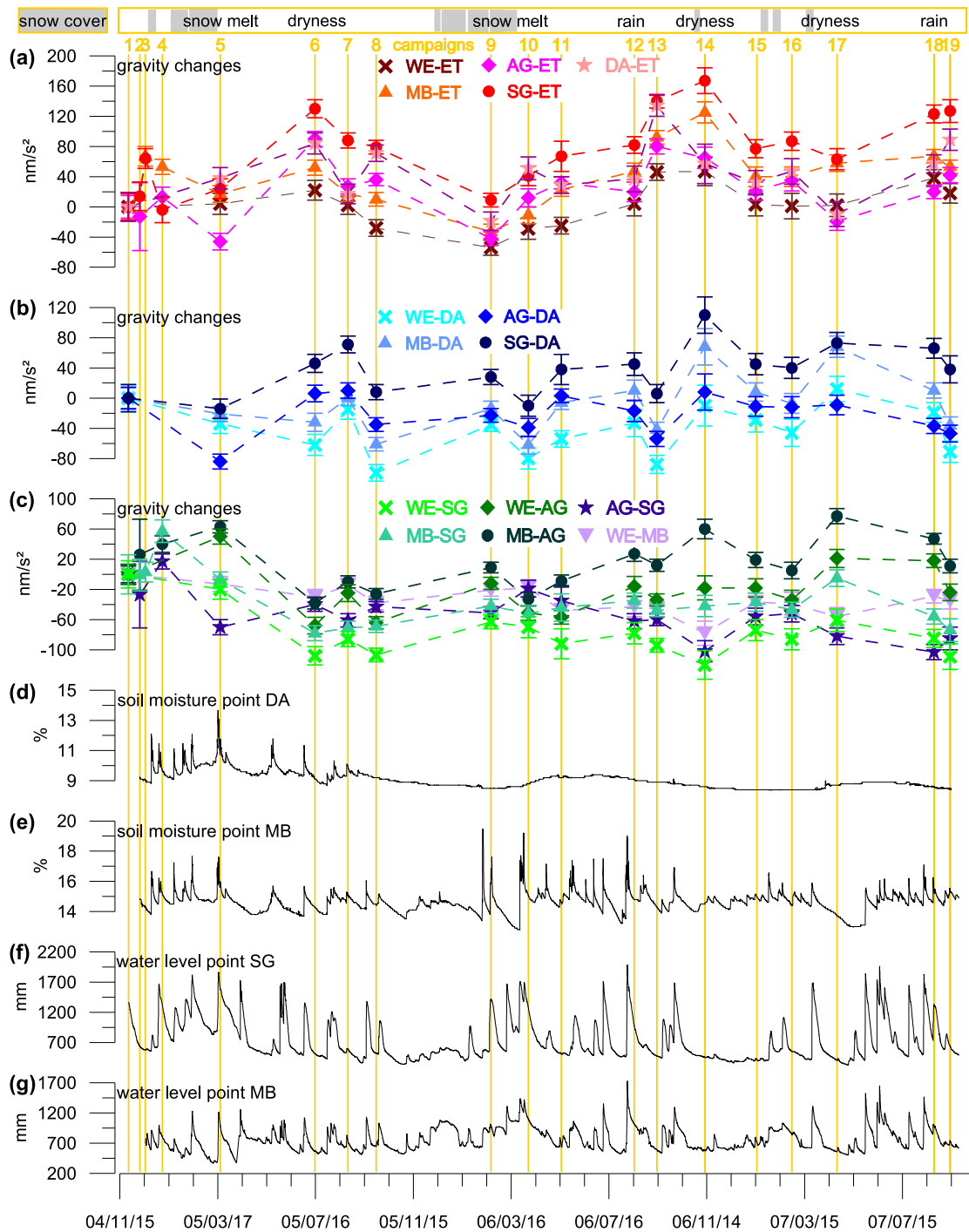


Figure 3.17: Temporal changes in the gravity differences with standard deviation and some hydrological parameters at the observation points: (a) gravity changes between different points in the valley and site *DA* on the observatory roof as well as point *ET* on the hill (cf. Figure 3.12), (b) gravity changes between different points in the valley and point *DA*, (c) gravity changes between all points in the valley, (d) soil moisture variation at point *DA* in 1 m depth, (e) soil moisture variation at point *MB* in 1 m depth, (f) water level variation at point *SG*, (g) water level variation at point *MB*.

Besides the reduced accuracy of the measurements in the test phase during campaigns 1-4, it has to be noted that in campaign 13 strong wind influenced the measurements and reduced the accuracy. In campaign 14 an earthquake disturbed the measurements. In this campaign the network could be covered only partially resulting in lower data quality.

Differences to the measuring point on the hill

In the gravity differences between the points within the Silberleite valley and point *ET* near the top of the steep slope (Figure 3.17 a) maximum changes of up to 171 nm/s^2 were observed between all campaigns, and 139 nm/s^2 between the two successive campaigns 5 and 6. The changes are maximum for the differences *AG-ET* or *SG-ET*, where the points *AG* and *SG* are situated in the observatory building at the foot of the slope. The changes are smaller in the differences from the points in the valley with increasing distance to the slope: In the difference *SG-ET* and *AG-ET* they amount to up to 106 nm/s^2 and 139 nm/s^2 respectively, between campaigns 5 and 6 (Figure 3.17 a). In the difference *MB-ET* a maximum change of 35 nm/s^2 was observed, and in the difference *WE-ET* a small variation of 18 nm/s^2 is estimated. In the difference *DA-ET* between the point on the observatory roof and the point on the hill also strong changes are detected. They amount to up to 46 nm/s^2 between campaigns 5 and 6 and to up to 153 nm/s^2 between all campaigns and show a similar behaviour as the changes in the differences between points in the valley and the point *ET* on the hill.

Differences to the gravity site on the observatory roof

A similar result was found for the gravity differences between the points within the valley and point *DA* on the observatory roof (Figure 3.17 b) but here the amplitude of the changes is generally about 20 % smaller. Between campaigns 5 and 6 the changes reach up to 60 nm/s^2 for the difference *SG-DA*, and up to 90 nm/s^2 for the difference *AG-DA*. For the differences from the points *MB* and *WE* outside the observatory in the middle of the valley to the observatory roof the changes are generally smaller: Between campaigns 5 and 6 they amount to up to 11 nm/s^2 for the difference *MB-DA*, and 28 nm/s^2 for the difference *WE-DA*. Between all campaigns changes of up to 130 nm/s^2 were determined.

Differences between the points in the valley

The variations in the differences between all points within the valley are given in Figure 3.17 c. In the differences *AG-SG* and *WE-MB* only very small changes were observed. This may be due to the specific location of the points: the points *AG* and *SG* close to each other in the observatory building, both points *WE* and *MB* outside the building. In contrast, in the differences *WE-SG*, *MB-SG*, *WE-AG*, and *MB-AG* between points inside and outside the observatory building (Figure 7.2 e-h), larger changes occurred. However, the changes in the differences between the measurement points in the valley are still too small to be significant, but they are consistent and trends can be identified. For example, between campaigns 5 and 6 all differences decreased by about 90 nm/s^2 , and between campaigns 8 and 9 all differences increased by about 40 nm/s^2 .

The unusual high values of the differences $AG-SG$, $MB-SG$, and $MB-AG$ in campaign 4 may be due to changes in the network design at campaign 4 and the fact that the high-precision instruments G858 and D187 were missing in this campaign (Section 3.3.4.1, Table 3.3). However, in the following campaigns the changes in the difference $AG-SG$ show almost always an opposite trend to all other differences within the valley, which can be explained by the particular situation of the points AG and SG , both within the observatory building close to the steep slope. This trend can also be recognized in the gravity changes between the points within the valley and point ET or DA (Figure 3.17 a, b); in particular between campaigns 5 and 6, as well as 16 and 17.

General considerations

The results indicate that the slope between the points WE , MB , AG , and SG in the valley and the point ET on the hill plays a crucial role in the changes of the gravity differences. The stronger the changes in topography between the observation points, the larger are the temporal gravity changes. This is also recognizable in the gravity differences between observation points within the valley and point DA on the observatory roof as well as in the difference $DA-ET$.

The previously mentioned diverse changes in the differences between the points within the valley can be explained by the respective position of the single points. Whereas the points SG and AG are located inside the observatory building close to the steep slope, the points WE and MB are situated close together outside the building in the middle of the valley (Figure 3.12). This also explains why the changes in the differences from the points SG and AG to the stations on the roof and on the hill have different characteristics in amplitude and sign than the changes in the differences from the points WE and MB to those stations.

3.3.4.4 Relation to hydrology

To investigate the relation between the observed gravity changes and hydrological variations, the gravity changes were compared to water level variations at the points SG and MB as well as soil moisture variations at the observation sites DA and MB over the whole measuring period from November 2004 to September 2007. These hydrological parameters are included in Figure 3.17 as an indication of the respective hydrological situation at the various gravity points.

The soil moisture data show variations of up to 6 % (Figure 3.17 d, e), the water level observations up to 1.5 m (Figure 3.17 f, g), with peaks after rain events or at snow melts. Comparing the temporal changes in the gravity differences with variations of the hydrological parameters, the following results were derived:

Differences to the point on the hill

During wet conditions, recognizable from high water level and high soil moisture (peaks in Figure 3.17 d–g) as well as the appearance of water in usually dry areas, the gravity dif-

ferences between various points in the Silberleite valley in different distances to the steep slope and the point *ET* near the top of the steep slope east of the observatory are generally by some 10 nm/s^2 smaller than during dry conditions (Figure 3.17 a). Between the extreme hydrological situations snow melt and dry summer in the year 2005 (between campaigns 5 and 6) a maximum increase of 139 nm/s^2 was observed in the differences. In the year 2006 (between campaigns 9 and 11) the measured changes amounted to up to 74 nm/s^2 .

The changes in the difference *DA-ET* from the observatory roof to the point *ET* behave similarly to the changes in the differences from points in the valley to the point *ET*. Partially even a higher amplitude was observed, for example between campaigns 8 and 9 (90 nm/s^2) or 17 and 18 (67 nm/s^2). This indicates that the processes which lead to the gravity changes are active not only between the points in the valley and point *ET* but also between the points *DA* and *ET*. Because the changes in this difference were between some campaigns larger than in the differences between points in the valley and point *ET*, the underlying hydrological effect seems to partially compensate between the points in the valley and point *ET* but is strongest between the observatory roof and the point on the hill.

Differences to the point on the observatory roof

Hydrological variations are also the reason for changes in the gravity differences between various observation points in the valley and the point *DA* on the observatory roof (Figure 3.17 b). The changes in the two differences *SG-DA* and *AG-DA*, e.g. between campaigns 5 and 6, show a different behaviour than the changes in the differences *MB-DA* and *WE-DA*, probably due to the different hydrological situation at the points in the valley. The strong changes in the differences between the points in the valley and point *ET* as well as in the difference *DA-ET* indicate a hydrological storage in the hill slope between these points as mentioned previously. The fact that strong changes were also observed between the points in the valley and point *DA* is a further indication that the hydrological process, which caused the gravity variations, is strongest in the differences between the points in the valley and the observatory roof and in the difference *DA-ET*. However, it partially compensates in the differences between points in the valley and the measurement point on the hill.

The roof of the observatory was covered with waterproof sheet in autumn 2005 resulting in a reduction of the soil moisture variations on the roof (Figure 3.17 d). However, the amplitude of the observed gravity changes did not decrease significantly after the roof was sealed up. This shows that soil moisture variations on the roof have only a minor impact on the gravity differences. Other hydrological processes in the surroundings, in particular water storage and flow processes within the hill slope, have a larger impact.

Differences between points in the valley

Hydrologically caused gravity changes occurred in the differences between the points in the Silberleite valley as well (Figure 3.17 c). As discussed in Section 3.3.4.3, in the differences *AG-SG* and *WE-MB* only very small changes of 84 nm/s^2 and 63 nm/s^2 were observed after the test phase. This may be due to the specific location of the points: the points *AG*

and *SG* close to each other in the observatory building, both points *WE* and *MB* outside the building in the middle of the valley in the same hydrological regime (Figure 3.12). In contrast, in the differences *WE-SG*, *MB-SG*, *WE-AG*, and *MB-AG* between points inside and outside the observatory building, larger changes of up to 118 nm/s^2 were observed. This indicates that the points within the building are differently influenced by local hydrology than the points outside the building. The gravity effect of changes in the various hydrological storages (e.g. soil moisture, ground water, joint water; Section 2.5) partially compensates in the middle of the valley (at points *WE* and *MB*), but is higher at the steep slope (points *SG* and *AG*). In particular, the points *SG* and *AG* are strongly influenced by hydrological variations in the hill.

General considerations

The observed gravity changes are associated with the hydrological situation at the respective points as indicated by soil moisture and water level measurements. However, the hydrological situation at Moxa observatory is rather complicated and a linear and obvious correlation between changes in the gravity differences and soil moisture or water level variations is not always fully visible. For instance, the gravity changes between campaigns 12 and 15 do not reflect the observed soil moisture or water level variations at the points *SG*, *MB*, or *DA* (Figure 3.17 a–g). Between the campaigns 17 (dryness) and 18 (rain) the gravity differences between points in the valley and the point *ET* increase in contrast to the changes in the other campaigns. By comparing the obtained gravity changes with hydrological point observations only, they cannot be fully explained. This is another indication that different hydrological compartments influence the gravity differences which are only partially reflected by the water level and soil moisture observations shown in Figure 3.17 d–g. The soil moisture and water level observations describe only the particular situation at the point of the measurement. They do not need to be valid in some distance from these points. In contrast, the gravimeter detects the integral hydrological mass changes. Thus, a direct correlation between soil moisture or groundwater table time series and the gravity differences is not always necessarily to be expected.

From the results it can be inferred that very local features have an essential influence on the gravity differences and result in a complex image of the temporal changes. The observed gravity changes are significantly influenced by the hydrological processes acting in the steep slope between the point on the hill and the points in the valley. They can be explained by varying water masses within the slope. This influence is larger than a priori expected from the experiments around the superconducting gravimeter (Section 3.2.3) as the changes in the gravity differences show.

In general, the variations observed in the gravity differences reflect local hydrological mass transport which opens the possibility to use them as constraint to evaluate local hydrological modelling.

4 Gravimetric 3D modelling

To provide constraints for an evaluation of local hydrological modelling and to derive a more sophisticated reduction of the hydrological influence in the superconducting gravimeter data, the observed hydrologically influenced gravity changes need to be compared to and verified by modelled gravity variations derived from hydrological mass changes. To translate hydrological mass variations, derived from hydrological modelling, into gravity changes, gravimetric modelling is needed. Therefore, a complex three-dimensional (3D) gravimetric model of the area around Moxa observatory was set up utilising the software package IGMAS (Interactive Gravity and Magnetic Application System; Götze, 1976, 1984; Götze & Lahmeyer, 1988; Schmidt, 1996, 2000).

4.1 Data basis

In a first step a gravity anomaly map of the surroundings of Moxa observatory was compiled to provide a basis for the gravimetric modelling. Because of the $1/r^2$ dependency of gravity in Newton's law of gravitation (r = distance between the two masses), and the natural features namely the topography and the local geology, a gravimetric survey area of $2 \times 2 \text{ km}^2$ around the observatory – as most important site – was selected (Figure 4.1). In this small-scale area gravity measurements with L&R gravimeters were carried out at 460 locations. The measurements have an accuracy of about $0.04 \cdot 10^{-5} \text{ m/s}^2$. For each location the geographical position, the elevation and the surrounding topography were also determined.

Because of the scaling in Newton's law, a very high resolution of the gravity anomaly was desired in the immediate surroundings of the observatory. In this region a maximum distance of 5 to 10 m between the gravity points was chosen to provide a high resolution gravity anomaly map. With increasing distance from the observatory the distance between the points was increased stepwise from 10 to 25, 50, 100, and, finally, 150 m (Figure 4.1). With the large number and high spatial density of gravity points in the area a very good data basis for a small-scale, 3D gravimetric modelling of the underground was provided. This included the possibility to obtain a high resolution of local geological and hydrological relevant structures in a range of less than 10 m in the close vicinity of the observatory.

4.2 Bouguer and free-air anomaly

From the measured gravity values the Bouguer anomaly Δg_B was calculated after Torge (1989):

$$\Delta g_B = g + \delta g_F - \delta g_{Pl} + \delta g_T - \gamma_0. \quad (4.4)$$

In this equation g is the observed gravity, reduced for tides and instrumental drift, δg_{Pl} the Bouguer plate reduction, δg_T the terrain reduction, δg_F the free-air reduction, and γ_0 the normal gravity.



Figure 4.1: Gravimetric sites in the surroundings of Moxa observatory. The locations of geoelectrical soundings and seismic lines, which are used as constraints for the gravimetric model, are also given. The aerial photograph was taken from [Google Earth \(2008\)](#).

The Bouguer anomaly (Figure 4.2) covers a range of approximately $0.7 \cdot 10^{-5} \text{ m/s}^2$. It is characterised by small-scale, southwest–northeast striking positive and negative anomalies. In particular an extensive positive anomaly south of the observatory which continues to northeast can be clearly identified. In the north a small positive anomaly also runs southwest–northeast. A negative anomaly striking southwest–northeast as well separates the positive anomalies.

The location and the extent of the anomalies correspond to geological units, which strike southwest–northeast as well (cf. Figure 2.5). The densities of the slate and greywacke at Moxa was determined in the laboratory, with $2740 \pm 10 \text{ kg/m}^3$ and $2600 \pm 10 \text{ kg/m}^3$ respectively. The geological units have a varying content of greywacke and slate. Positive anoma-

lies are connected to rocks which mainly contain slate. These rocks have a higher density than the rocks with a larger fraction of greywacke to which negative anomalies are assigned (cf. Table 4.1). Anomalies related to geological faults (cf. Figures 2.5, 2.6, and 2.7) could not be detected; the dislocation of the faults mapped and the differences between the densities of the geological units are too small. Therefore, faults were not included into the gravimetric model.

It turned out that the terrain reduction δg_T (Figure 4.3) is in the same order of magnitude as the Bouguer anomaly Δg_B in the Moxa area. Thus, special care was applied to reduce inaccuracies. The near field terrain reduction was determined by observing all relevant topography changes in a radius of 200 m around the particular gravity station. From these observations values for δg_T were calculated using the standard rock density of 2670 kg/m^3 . In the direct vicinity of the observatory values of up to $\delta g_T = 0.8 \cdot 10^{-5} \text{ m/s}^2$ occur which decrease rapidly with increasing distance to the observatory. In the outer regions of the modelling area, the values are smaller than $0.1 \cdot 10^{-5} \text{ m/s}^2$. For this reason and due to the small extension of the study area middle or far field terrain reductions were not applied.

If the terrain reduction was neglected in the computation of the Bouguer anomaly (Equation 4.4), a strong negative anomaly arose in the direct vicinity of the observatory, following the valley of the creek Silberleite and making an interpretation of the geological structure in the subsoil impossible (Figure 4.4). Therefore, the terrain reduction must not be neglected in the calculation of the Bouguer anomaly in the Moxa area.

The density structure of the subsoil in the Moxa area can be modelled more accurately if the free-air anomaly Δg_F is used as basis because of two reasons:

- Reductions of rock masses like the Bouguer plate reduction δg_{Pl} and the terrain reduction δg_T , which are part of the calculation of the Bouguer anomaly Δg_B , are error-affected to a certain amount, because they are calculated using the standard rock density of 2670 kg/m^3 , which is not necessarily the correct density value for the rocks around Moxa observatory.
- The Bouguer anomaly Δg_B is very small compared to the changes in topography in the surroundings of Moxa observatory. Thus, uncertainties in the determination of the terrain reduction δg_T can have a big impact on the resulting Bouguer anomaly.

In the gravimetric modelling the mass distribution below and above the gravity stations is an essential part. In the free-air anomaly Δg_F with

$$\Delta g_F = g + \delta g_F - \gamma_0 \quad (4.5)$$

reductions of rock masses are not applied. It turned out to be best suited for the aspired investigations in which topography and hydrological specials need to be included. The free-air anomaly, shown in Figure 4.5, covers a gravity range of $14 \cdot 10^{-5} \text{ m/s}^2$ with lower values in the valley at the observatory and south of it, but higher values on the plain north and northwest of the station.

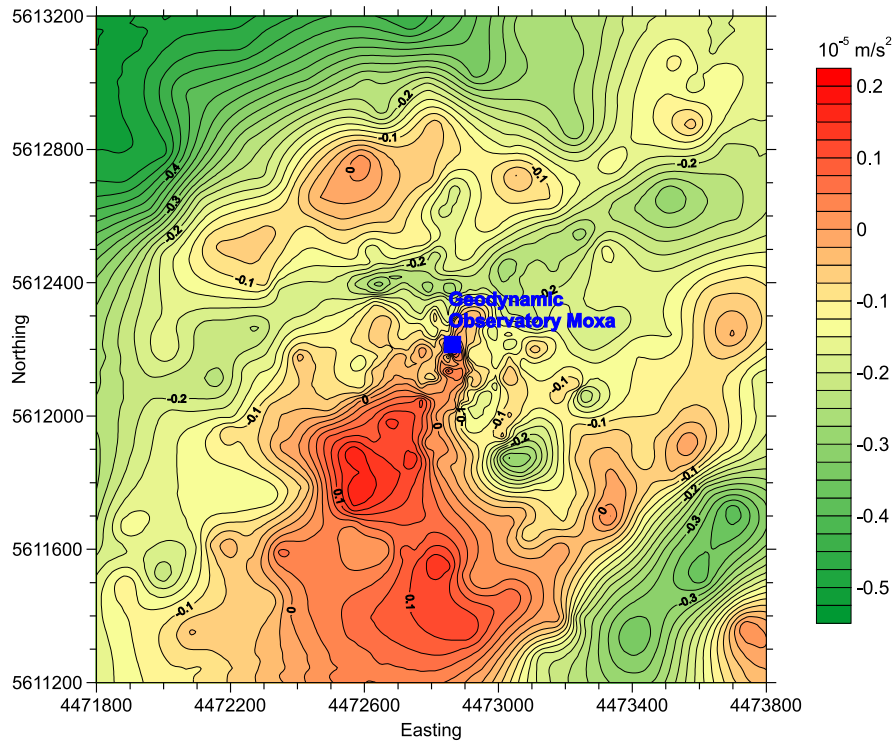


Figure 4.2: Bouguer anomaly in the surroundings of Moxa observatory.

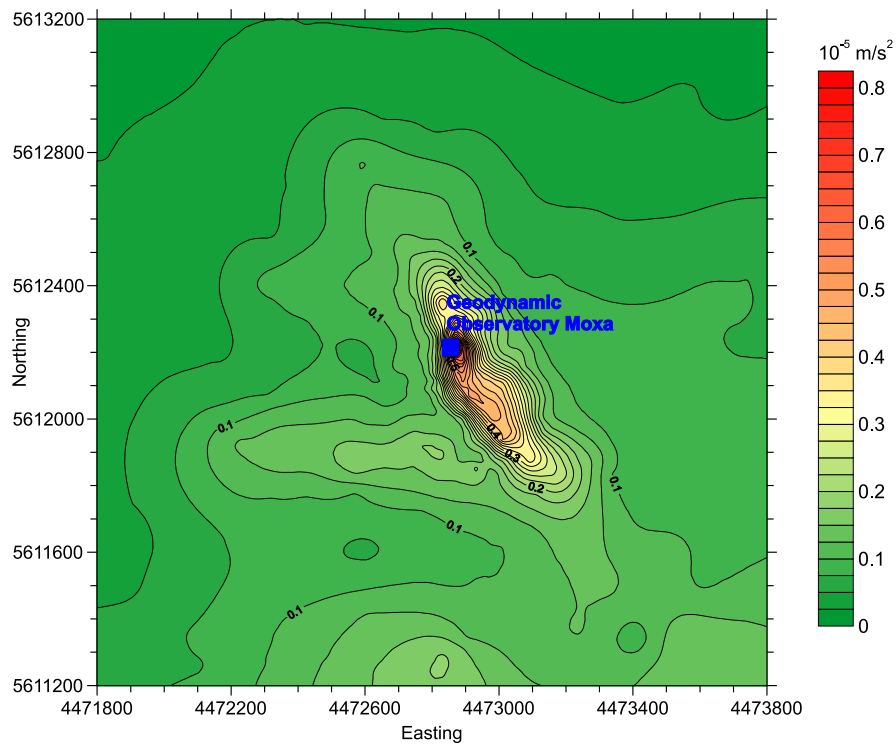


Figure 4.3: Terrain reduction in the surroundings of Moxa observatory.

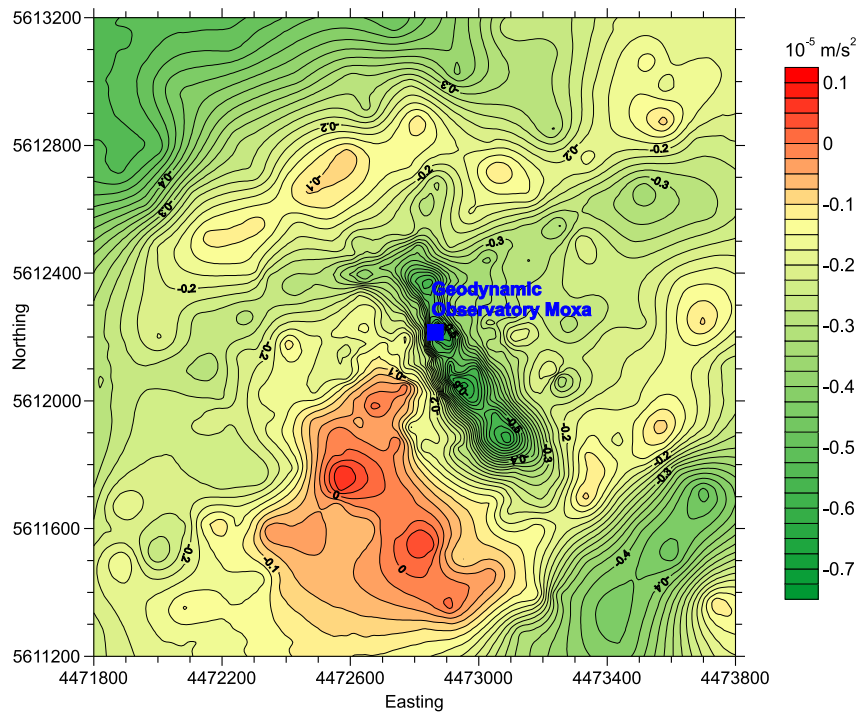


Figure 4.4: Bouguer anomaly in the observatory vicinity without terrain reduction.

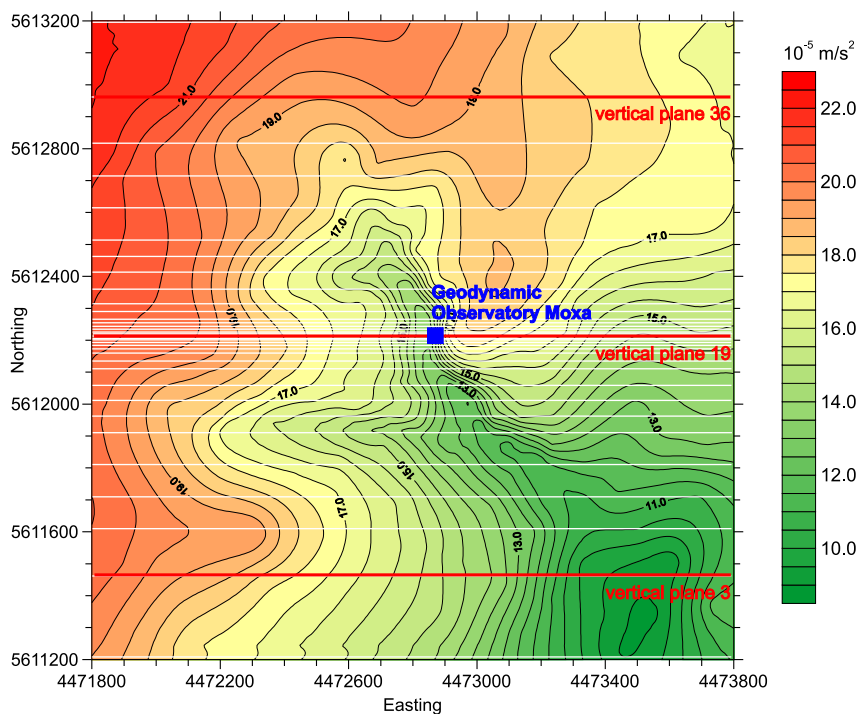


Figure 4.5: Free-air anomaly in the surroundings of Moxa observatory and the 38 vertical planes of the gravimetric 3D model (white lines). The modelling plane 19 which cuts through the observatory is shown in Figure 4.6, the planes 3 and 36 in the Figures 4.8 and 4.9.

Because of the disregarded Bouguer plate and terrain reduction, however, in the free-air anomaly gravity anomalies caused by geological structures are masked by the effect of the topography (cf. Figure 4.1). Thus, the Bouguer anomaly was used for the interpretation of the geology. This information entered the gravimetric 3D model, which is based on the free-air anomaly. It includes the density structure of the geological subsoil in the hilly topography of the observatory's vicinity.

4.3 Boundary conditions

To limit the ambiguities which are associated with potential methods, the inclusion of extensive geological, tectonic, and geophysical constraints in the gravimetric model is required to ensure a realistic modelling.

The results of a geological mapping as well as a geological and tectonic model (Section 2.4) are directly used for the gravimetric model. Further constraints, in particular regarding the type and the thickness of the soil and the aquiferous layer of disaggregated bedrock, are derived from the soil mapping campaign (Scholten et al., 2004) as well as from drilling and digging in the observatory gallery and its surroundings. Results from small-scale seismic and geoelectrical measurements – carried out 1998 by Schulze (1998) as well as during student practical trainings over the last seven years (Jahr et al., 2008) – provide spatially distributed information about the thickness of the soil and the disaggregated bedrock. The spatial distribution of the geoelectrical soundings and seismic lines available in the modelling area is included in Figure 4.1.

In the valley, the soil layer (including artificial valley fill) has a thickness of 2.4 m to 4.0 m. At the steep slope east of the observatory it reaches a thickness between 0.20 m and 0.45 m and on the plain around the Silberleite valley a thickness of 1.3 m to 2.3 m. The thickness of the disaggregated bedrock varies between 13 m and 18 m in the valley, between 3.5 m and 5.0 m at the slope, and between 9 m and 12 m on the plain.

The densities of the rocks outcropping in the study area and used in the gravimetric modelling were determined in the laboratory (Table 4.1). Both, outcropped solid rock and material from drill cores were used. Pure slate turned out to have a density of $2740 \pm 10 \text{ kg/m}^3$, pure greywacke of $2600 \pm 10 \text{ kg/m}^3$. In Table 4.1 the composition and the calculated corresponding densities of the geological bodies are summarised.

To determine the density of the disaggregated bedrock engineer-geologic measurements were carried out at joint or fault zones which are available in the drill cores. The density of an approximately 25 cm thick joint zone, preserved in a drill core, was determined in the laboratory with $2110 \pm 50 \text{ kg/m}^3$. Joint zones like this occur approximately every 10 m in the disaggregated bedrock. Additionally, the rock contains many small joints, faults and cracks. Approximately 5 % of the rock in the disaggregated bedrock can be assumed to be jointed material. This leads to the densities given in Table 4.1. The densities of the cambisol in the forest and the gleysol at the valley floor were measured several times and in different depths with engineer-geologic methods (cf. Prinz, 1997) and an average density was calculated.

Table 4.1: Measured rock densities around Moxa observatory applied in the gravimetric model.

Geological unit	Composition	Density of bedrock in kg/m ³	
		intact	disaggregated
Interbedded Lower Ziegenrück Subformation	50% slate, 50% greywacke	2670	2640
Interbedded Röttersdorf Subformation	75% slate, 25% greywacke	2710	2680
Röttersdorf banded slates Subformation	90% slate, 10% greywacke	2730	2700
Kaulsdorf Formation	50% slate, 50% greywacke	2670	-
Soil layer with weathering zone	cambisols & rock fragments		2050
Valley floor	gleysols & rock fragments		2150

4.4 The gravimetric 3D model

For the modelling the area was divided into 38 east-west running vertical planes (Figure 4.5) to account for the inhomogeneous geology. Within the planes polygons (lines) build up the geological model bodies. Between the planes, polygons are built by triangulation of lines and form 3D bodies, to which a density value is assigned. The gravity effect of these 3D bodies was calculated (Götze, 1976, 1984) and compared to the observed free-air anomaly. By iterative variation of the model parameters (geometry and density of the bodies) the modelled gravity was changed successively to match the observed free-air anomaly and to ensure a gravimetric modelling close to reality for the further investigations.

A sufficiently precise implementation of the topography and the soil layers is important to correctly represent the hydrological situation. To include important topographical and hydrological details in good quality into the model, the planes of the gravimetric model were oriented east–west, perpendicular to the valley of the creek Silberleite at the observatory. The planes in the immediate surroundings of the observatory were chosen to have a very small distance of 5 m (Figure 4.5). Thus, a very high resolution of a few metres is achieved in this part of the model, corresponding to the spatial resolution of the topography, the hydrological information, and the higher density of gravity points in this area. With increasing distance to the observatory, the distance between the planes is increased gradually up to 150 m (Figure 4.5).

In Figure 4.6 plane 19 of the gravimetric 3D model is shown which runs directly through the observatory (cf. Figure 4.5). In the upper part of the figure the observed free-air anomaly is given in red and the calculated one is dotted in black. The calculated free-air anomaly results from the topography and the density model in the lower part of the figure.

The wavelengths and amplitudes of the folded geological layers were taken from the geolog-

ical model (Section 2.4) and adapted to the gravimetric model. The geology was modelled to the top of the Kaulsdorf Formation, given in green in Figure 4.6. The underlying layers have a similar density as the Kaulsdorf Formation. In this small-scale study area they are gravimetrically not relevant. Besides the bedrock, two layers were added to the model: a soil layer, consisting of cambisol in the forest and gleysol at the valley floor and a layer of disaggregated bedrock for each particular geological unit.

Figure 4.7 gives a detail from plane 19 in the immediate surroundings of the observatory. In this part of the model, the distribution and thickness of the soil and disaggregated bedrock layers were not only derived from geoelectrical and seismic measurements but also from digging and drilling. The densities of samples from the soil layers were determined in situ, the densities of the disaggregated and the intact bedrock in the laboratory. They were used to further constrain the gravimetric model. Additionally, pore volumes of up to 30 vol.-% were determined for the soil in depths down to 1 m.

As the Silberleite valley is narrow (20-30 m wide) with a steep slope to the east of the observatory, the free-air anomaly has a minimum in the valley and strongly increases at the slope (Figure 4.6). To the south and to the north of the observatory the Silberleite less incises in the topography as Figures 4.8 and 4.9 show.

In plane 3 (Figure 4.8), a plane in the southern part of the model (cf. Figure 4.5), the Silberleite valley is approximately 150 m wide in the east of the modelling area resulting in a gentle variation of the free-air anomaly of about $4 \cdot 10^{-5} \text{ m/s}^2$. In the northern part of the model, e.g. in plane 36 (Figure 4.9) the Silberleite valley is only hardly visible as an about 100 m wide depression in the west of the modelling area. While in the centre (plane 19, Figure 4.6) and partly in the north (plane 36, Figure 4.9) of the study area 3rd order folds are geologically mapped (cf. Section 2.4.3) and included into the gravimetric model, in the south of the study area (plane 3, Figure 4.8) they could not be found at the surface. Additionally, from the Bouguer anomaly no indications can be derived that they are essential to explain the observed gravity. Thus, they were not included into the southern part of the gravimetric model.

In Figure 4.10 the complete gravimetric 3D model is shown including the disaggregated and intact bedrock of the particular geological unit as well as gleysol (green) and cambisol (yellow) as soil layer. The final model consists of 26,445 triangles distributed in and between 38 vertical planes. 10,332 vertices build up 15 geological and hydrological bodies which a different density value is assigned to.

The triangulation of the surface on the topography and of the geological layers between the planes of the 3D model is shown in Figure 4.11 as line between the vertices within one plane and between the planes. The position of plane 19, the plane through the observatory (Figure 4.6), is indicated additionally.

Edge effects in the model may influence the calculated gravity effect and falsify the modelling results. To avoid this, the lateral extension of the complete model exceeds the area of gravity calculation in x- and y-direction by 10 km.

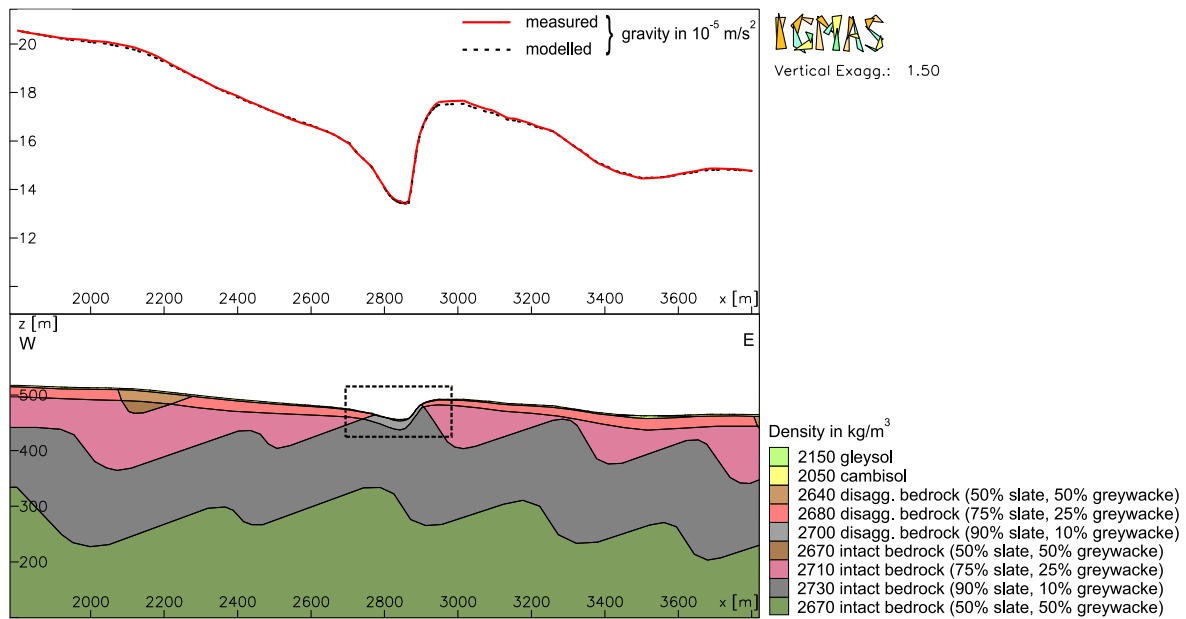


Figure 4.6: Plane 19 (plane through observatory, cf. Figure 4.5) of the gravimetric 3D model including topography, soil layer with gleysol at the valley floor and cambisol in the forest, disaggregated bedrock, and intact bedrock with densities up to a distance of 1 km from the observatory. The dotted box marks a detail of plane 19 which is given in Figure 4.7. In the upper part the observed and modelled free-air anomaly is shown.

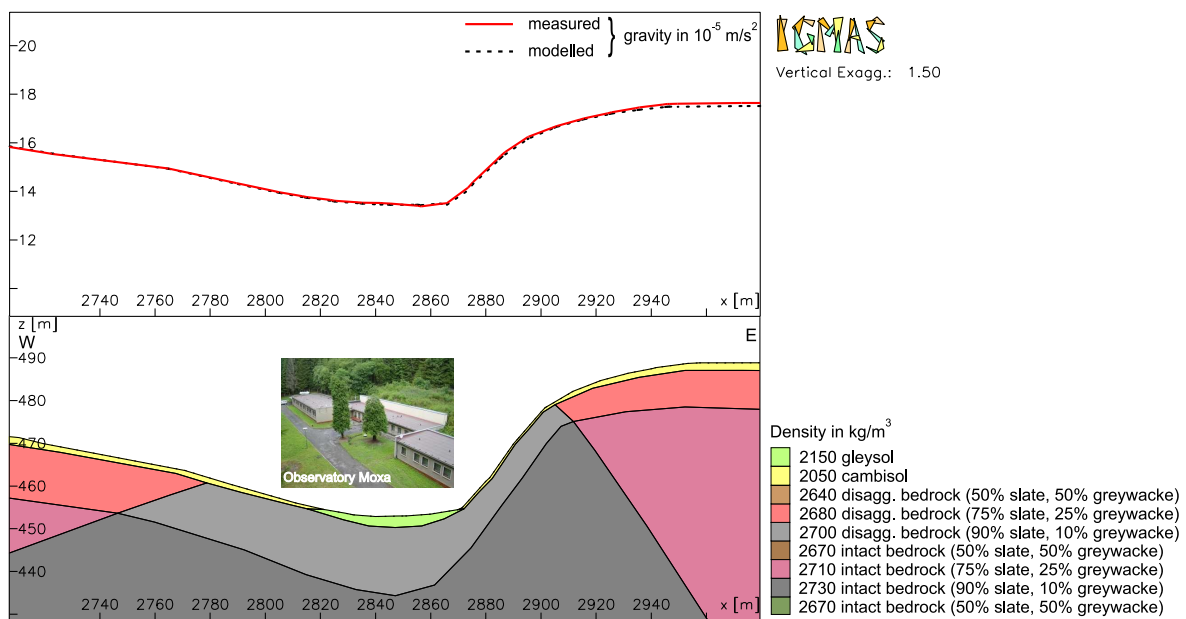


Figure 4.7: Detail of plane 19 showing the geologic bodies as well as the soil layer with gleysol at the valley floor and cambisol in the forest in the direct vicinity of the observatory.

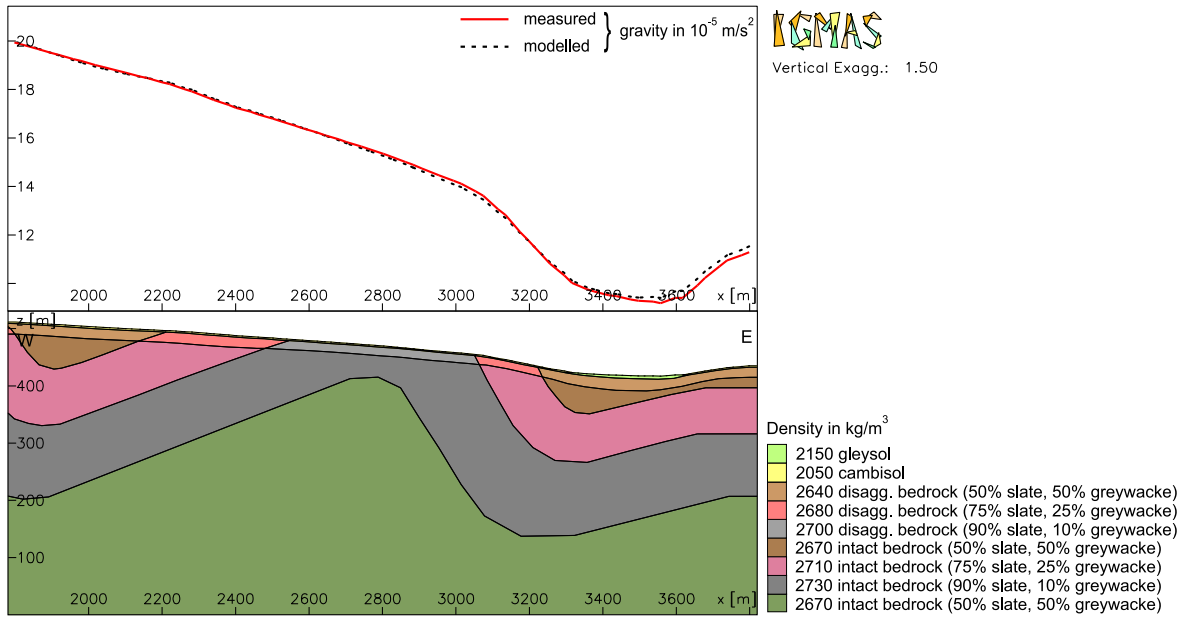


Figure 4.8: Plane 3 of the gravimetric model (cf. Figure 4.5).

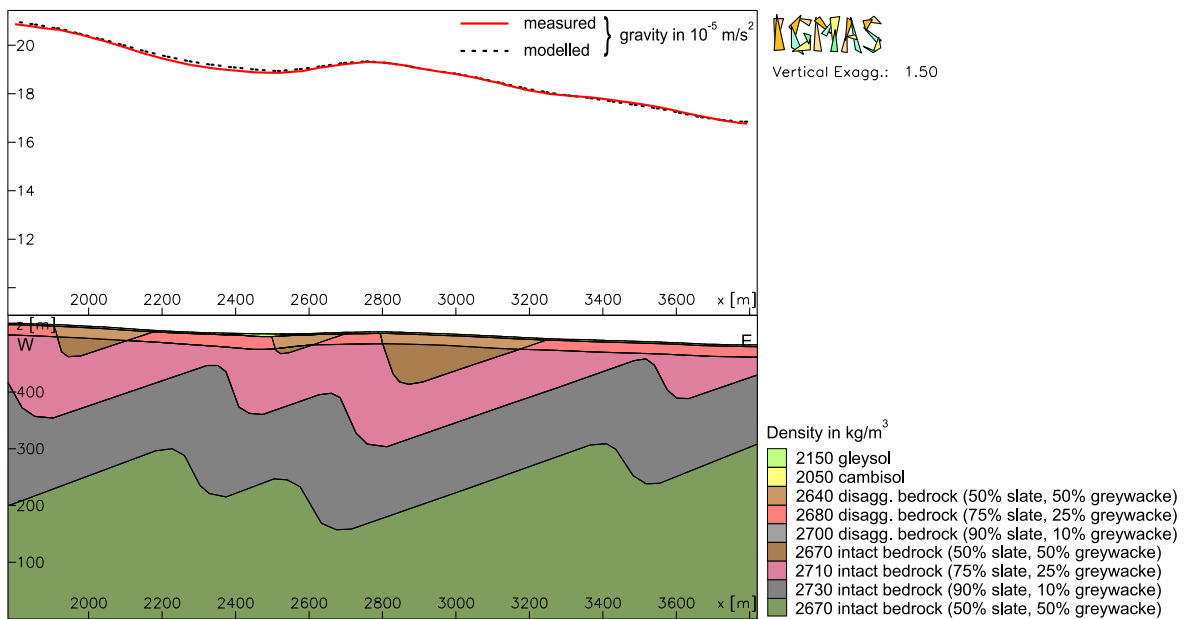


Figure 4.9: Plane 36 of the gravimetric model (cf. Figure 4.5).

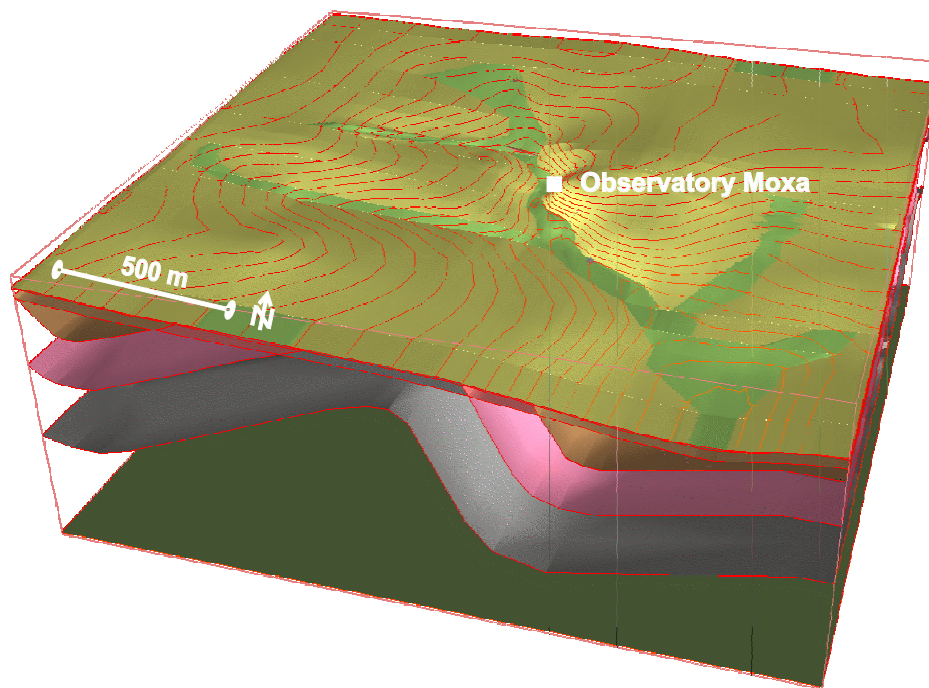


Figure 4.10: Gravimetric 3D model of the observatory surroundings including topography, disaggregated and intact bedrock, and soil layer. Legend is given in Figure 4.6.

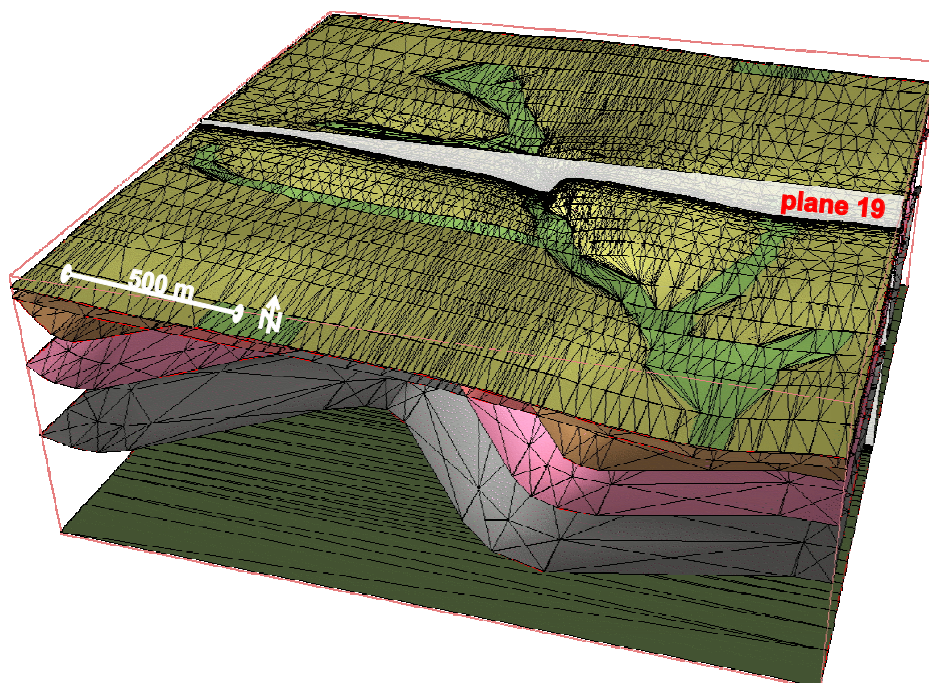


Figure 4.11: Triangulation of the surfaces of the gravimetric 3D model and position of plane 19 (cf. Figures 4.5 and 4.6) within the model. Legend is given in Figure 4.6.

4.5 Residuals

The free-air gravity anomaly computed from the gravimetric model corresponds well to the observed free-air anomaly (Figure 4.5) in the study area. The quality of the gravimetric modelling can be evaluated by the residuals (Figure 4.12) which are defined as discrepancy between measured and modelled gravity. In most regions of the gravimetric model residuals smaller than $\pm 0.1 \cdot 10^{-5} \text{ m/s}^2$ occur. Compared to usual gravity field anomalies (e.g. Gabriel et al., 1997; Hofmann et al., 2003), here the residuals are lower by the factor of 20 because of the small study area with small Bouguer anomaly.

The agreement between modelled and measured gravity in the long wave lengths (several 100 m) can be considered as good, because a correlation with the Bouguer anomaly (Figure 4.2) does not exist. Local deviations up to $\pm 0.35 \cdot 10^{-5} \text{ m/s}^2$ occur mainly at the edges of the model and between the modelling planes in some distance from the observatory. There, the distance between the planes is 100 to 150 m (cf. Figure 4.5). Therefore, these local deviations are intrinsic. They represent less than 1 % of the frequency of the deviations. Additionally, the large residuals around the first and last planes can be attributed to missing boundary information in these areas. Because of the integral gravimetric effect geological structures beyond the modelling area also affect the measured gravity. As mentioned previously, two boundary planes in a distance of 10 km from the study area were defined and the modelled geological structures were extrapolated to these planes to reduce the gravimetric impact of geological structures beyond the modelling area.

The residuals in the direct vicinity of the observatory ($r \approx 200 \text{ m}$), given in Figure 4.13, are mostly within the $\pm 0.1 \cdot 10^{-5} \text{ m/s}^2$ range. In general, larger residuals are outside the direct surroundings of the observatory. The large residuals of up to $+0.25 \cdot 10^{-5} \text{ m/s}^2$ in the south-west of the local area are caused by the gravity values at two gravimetric measuring points located between the modelling planes. The larger extension of this region in Figure 4.13 is due to the interpolation between the measuring points.

The percentage distribution of the deviations between measured and modelled gravity is shown in Figure 4.14. The frequency of the deviations is given between 0 and 1, corresponding to 0 and 100 %. A strong decrease of the frequency of the residuals outside the interval $\pm 0.1 \cdot 10^{-5} \text{ m/s}^2$ can be noticed. Only 12 % of the residuals are outside the interval $\pm 0.1 \cdot 10^{-5} \text{ m/s}^2$, underlining the good quality of the developed gravimetric 3D model. Thus, the complex geology of the study area including soil layer and disaggregated bedrock was sufficiently included in the gravimetric model. This enables the application of the developed model for hydrological studies.

The impact of the geological and hydrological structures on the achieved residuals was tested. Applying a uniform density structure in the whole gravimetric model with no geological or hydrological structures, but including the topography, a standard deviation of the residuals between the measured free-air anomaly for all gravity stations and the modelled free-air anomaly of $0.1016 \cdot 10^{-5} \text{ m/s}^2$ was derived. The consideration of the geometry and different densities of the folded geological units reduced the standard deviation to $0.0953 \cdot 10^{-5} \text{ m/s}^2$. An additional inclusion of the layer of disaggregated bedrock, reduces

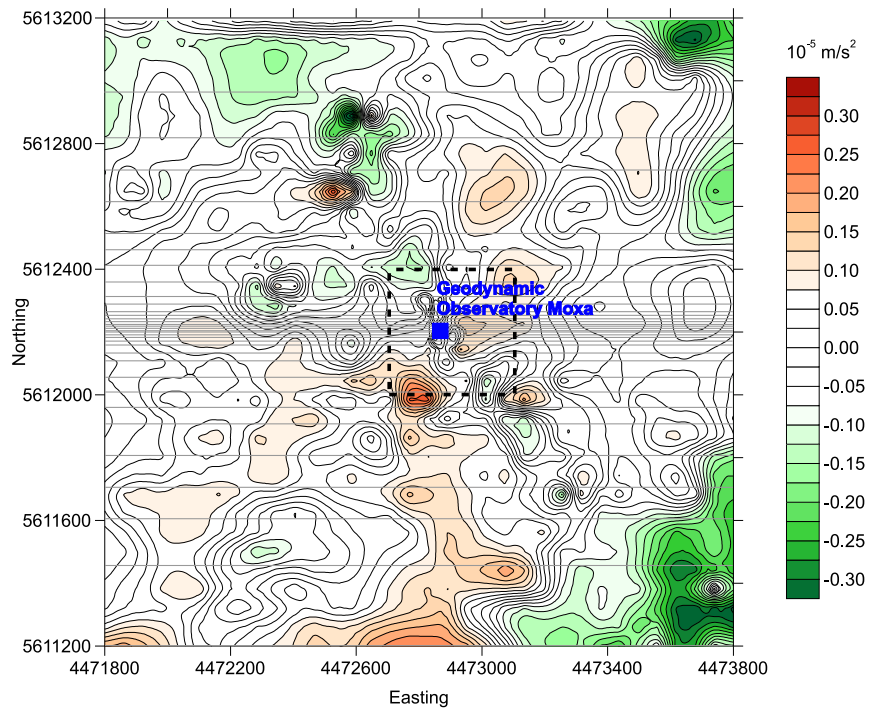


Figure 4.12: Residuals of the gravimetric model. The contour line spacing is $0.025 \cdot 10^{-5} \text{ m/s}^2$. The location of the planes of the gravimetric model is given as well. The dotted box marks the inner part of the modelling area which is given in Figure 4.13.

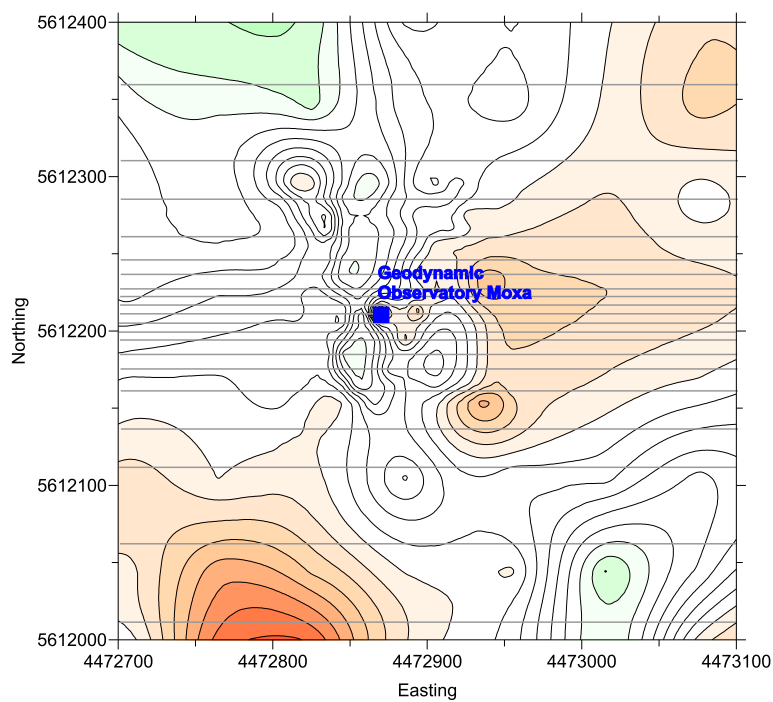


Figure 4.13: Local residuals of the gravimetric model in the vicinity of the observatory. The contour line spacing is $0.025 \cdot 10^{-5} \text{ m/s}^2$. The location of the planes of the gravimetric model is given as well.

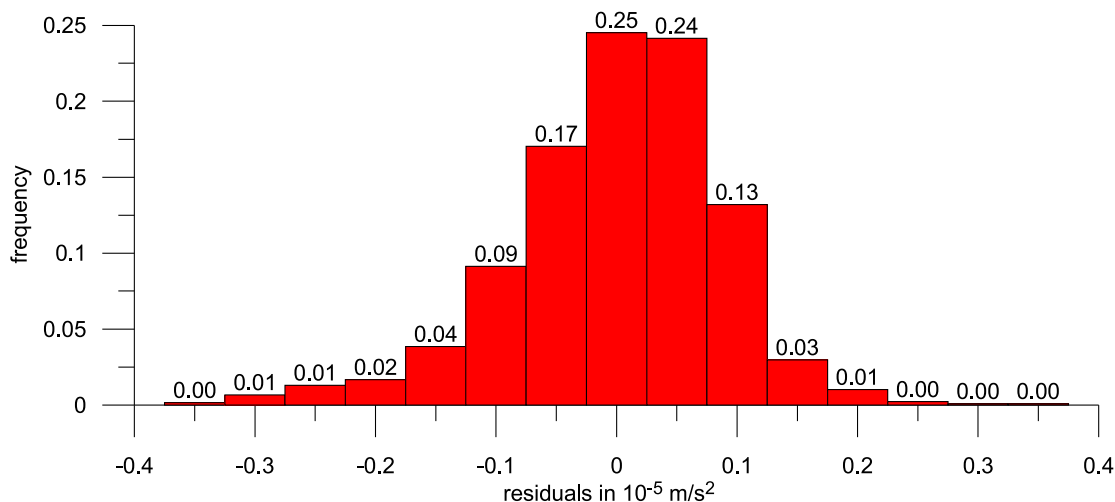


Figure 4.14: Histogram of the residuals of the gravimetric 3D model.

the standard deviation further to $0.0934 \cdot 10^{-5} \text{ m/s}^2$. Finally, if a soil layer is added on the top of the disaggregated bedrock, a standard deviation of $0.0868 \cdot 10^{-5} \text{ m/s}^2$ is reached.

From the gravimetric point of view a further reduction of the residuals is possible, for example by an expansion of the modelling area and the consideration of additional planes. Compared to the existing boundary conditions in the area and the accuracy of the observed Bouguer and free-air anomaly a more detailed modelling is not expedient and would mean an over-interpretation. These considerations also concern 3rd order folds. Some of the very small-scale variations in the Bouguer anomaly (Figure 4.2) are probably caused by 3rd or 4th order folds. Because these folds are only partially and mostly doubtfully geologically mapped in the surroundings of the observatory, a complete inclusion of them into the gravimetric model is not appropriate and also not needed for the aim of this work.

4.6 Different model versions

To investigate the impact of uncertainties in the thickness of the soil layer and the disaggregated bedrock on the modelling results, seven different versions of the gravimetric model were developed (Table 4.2). In these model versions the thickness of the layers was varied differently in the observatory valley, at the slope, and on the plateau around the Silberleite valley. The average thickness of the soil layer was changed in the valley between 1.5 and 4.5 m, at the slope between 0.05 and 0.6 m, and on the plain between 0.2 and 3.0 m, whereas the average thickness of the disaggregated bedrock was varied between 9 and 21 m in the valley, between 2.5 and 5.5 m at the slope, and between 4 and 16 m on the plateau. In Table 4.2 the standard deviations of the residuals between the observed and the computed free-air anomaly are also given to show the quality of the gravimetric modelling. Model version 3 is the original model which best reproduces the boundary conditions described in Section 4 (geolectrical and seismic measurements, digging, drilling, and the soil mapping

campaign). For this model version the standard deviation is lowest ($0.0868 \cdot 10^{-5} \text{ m/s}^2$), for the versions 2 ($0.0873 \cdot 10^{-5} \text{ m/s}^2$), and 4 ($0.0870 \cdot 10^{-5} \text{ m/s}^2$) only slightly higher. The model versions 0 ($0.0886 \cdot 10^{-5} \text{ m/s}^2$) and 6 ($0.0884 \cdot 10^{-5} \text{ m/s}^2$) show the highest standard deviations. They also do not reflect the thickness of the soil layer and the disaggregated bedrock given by the boundary conditions. Therefore, they were excluded from further studies. The model versions 1 and 5 also do only marginally match the boundary conditions and have high standard deviations compared to the versions 2–4.

Table 4.2: Versions of the gravimetric model to study the impact of the thickness of the soil layer and the disaggregated bedrock on the model results. Additionally, the standard deviation of the residuals between the measured free-air anomaly for all gravity stations and the modelled free-air anomaly is given (cf. Figure 4.1 and 4.5). The model versions 2, 3, and 4 match the depth information from seismic and geoelectrical measurements. Version 3 matches them best, versions 0, 1, 5, and 6 only marginally.

Model version	Average thickness in m						Standard deviation of the gravimetric model in 10^{-5} m/s^2
	Observatory valley		Steep slope		Plain		
	Soil	Dis. bedrock	Soil	Dis. bedrock	Soil	Dis. bedrock	
0	1.5	9	0.05	2.5	0.2	4	0.0886
1	2.0	11	0.1	3.0	0.5	6	0.0880
2	2.5	13	0.2	3.5	1.0	8	0.0873
3	3.0	15	0.3	4.0	1.5	10	0.0868
4	3.5	17	0.4	4.5	2.0	12	0.0870
5	4.0	19	0.5	5.0	2.5	14	0.0876
6	4.5	21	0.6	5.5	3.0	16	0.0884

5 Hydrological modelling

A hydrological modelling for the Silberleite catchment was realised with the fully distributed process-oriented hydrological model J2000 (Krause, 2001; Krause et al., 2005, 2008). In close connection to the geophysical requirements the modelling was carried out by S. Eisner and P. Krause from the Institute of Geography of the Friedrich-Schiller-University Jena.

5.1 Model layout

J2000 implements the relevant hydrological processes evapotranspiration, snow accumulation and melt, interception, soil water balance, and groundwater balance as conceptual approaches. The catchment (Figure 5.1) was partitioned into 337 process-oriented response areas (Hydrological Response Units – HRUs, Figure 5.2) which were delineated by a geographic information system (GIS) overlay of the relevant physio-geographical input information (topography, land use, soil types, geology). For the modelling, the measured climate data precipitation, temperature, solar radiation, relative humidity, and wind velocity, recorded at the observatory, were used as driving forces.

Each HRU consists of different water storages (surface depression storage, snow storage, interception storage, large and middle pore soil storage, and groundwater storages) which interact with each other. Lateral water movement from one HRU to the next is simulated by connections between the single units (Figure 5.2). Based on these contacts, flow cascades are implemented which route the flow components (overland flow, interflow, quick and slow baseflow) through the units and finally into the creek Silberleite, following the maximum topographic gradient. Inside the creek, the water is routed as streamflow to the catchment outlet. The model was applied in hourly time steps for the period from 03/10/23 to 07/05/27 and calibrated with the observed streamflow records.

5.2 Streamflow

From the comparison of the simulated to the observed streamflow values near the observatory (Figure 5.3) emerges that the hydrological dynamics could be reproduced fairly well, which is confirmed by the Nash-Sutcliffe efficiency value (Nash & Sutcliffe, 1970) of $R_{eff} = 0.8$. The Nash-Sutcliffe efficiency

$$R_{eff} = 1 - \frac{\sum_{t=1}^T (Q_o^t - Q_m^t)^2}{\sum_{t=1}^T (Q_o^t - \overline{Q_o})^2} \quad (5.6)$$

is used as a quality criterion to evaluate the model performance. In Equation 5.6 Q_o^t is the observed streamflow at time t , Q_m^t the modelled streamflow at time t , and $\overline{Q_o}$ the mean observed streamflow. The Nash-Sutcliffe efficiency R_{eff} can range from $-\infty$ to 1. An efficiency of $R_{eff} = 1$ corresponds to a perfect match of modelled streamflow to the observed

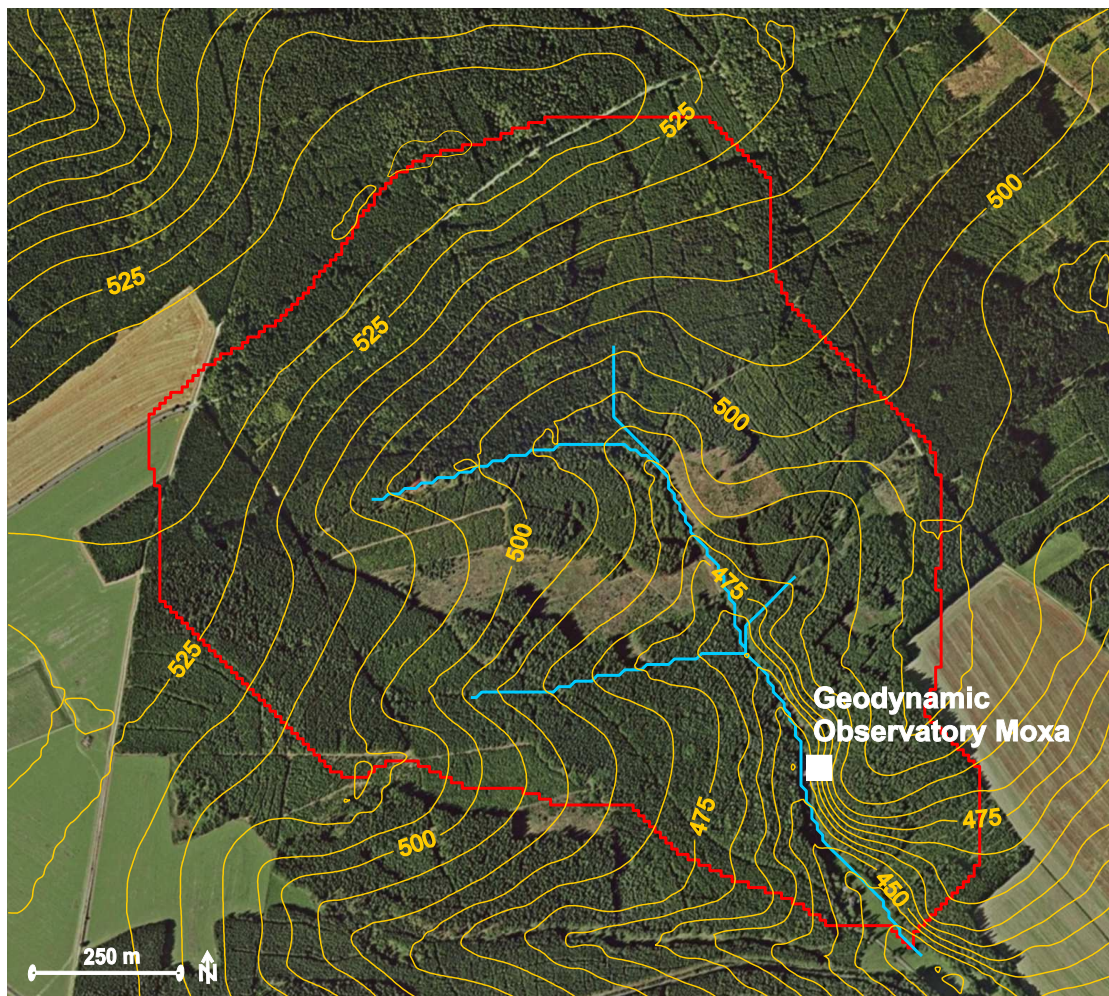


Figure 5.1: Topography around Moxa observatory and catchment area (red line) of the creek Silberleite (blue line). The aerial photograph was taken from [Google Earth \(2008\)](#).

data. $R_{eff} = 0$ indicates that the model predictions are as accurate as the mean of the observed data, whereas $R_{eff} < 0$ occurs when the observed mean is a better predictor than the model. The closer the model efficiency is to 1, the more accurate the model is. In general, the model fit can be characterised as good if $R_{eff} > 0.7$ ([Becker & Behrendt, 1998](#)).

The hydrographs in [Figure 5.3](#) show that the catchment is characterised by higher flows during winter and in particular during snow melt events in spring, whereas in summer the streamflow is in general low with some single flood events, e.g. in November 2004 and August 2006. The model is able to reproduce the hydrological variability of the catchment even if some peaks are not matched perfectly.

Especially at heavy rain events or at snow melt larger deviations between observed and modelled streamflow of up to some 10 l/s occur. These events are often underestimated. A heavy rain event in November 2004, however, is overestimated by about 20 l/s. It is always dif-

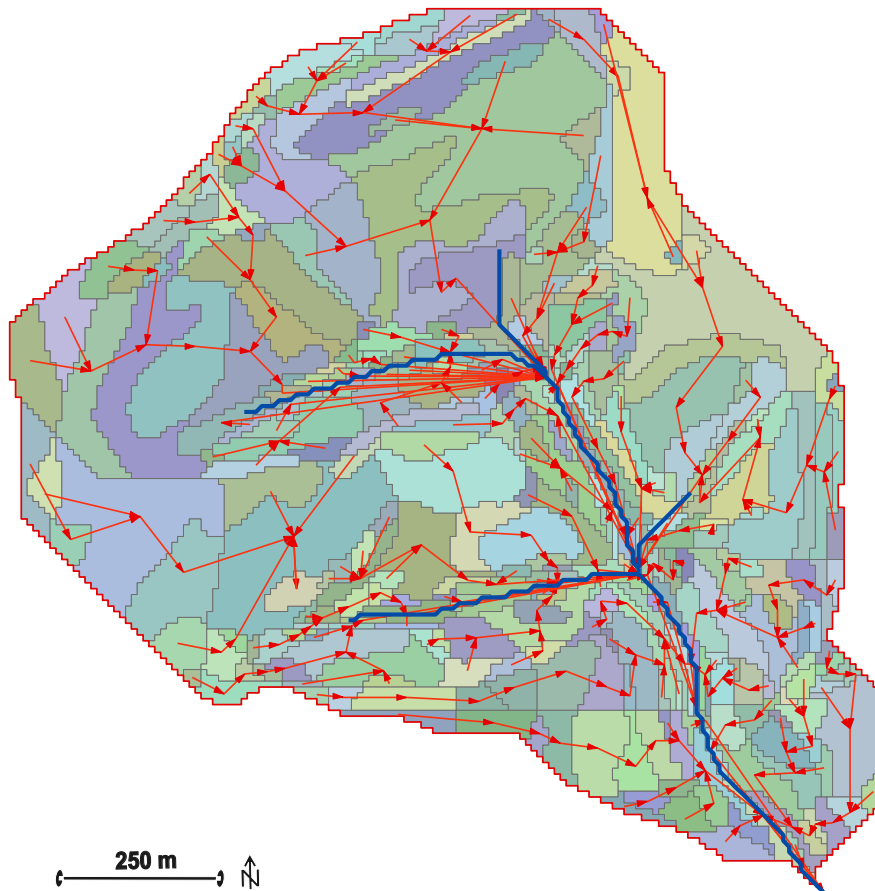


Figure 5.2: Hydrological response units (HRUs) of the small-scale hydrological model of the Silberleite catchment and lateral routing (red lines) of the water between the HRUs to the creek Silberleite following the maximum topographic gradient.

difficult to match the observed data at extreme hydrological events. For the present question, however, a sufficient accuracy was reached.

5.3 Water content of hydrological storages

For the combination of the hydrological model and the gravimetric model (Section 4), the actual contents of all storages of each HRU and time step were exported from the hydrological model. In Figure 5.4 the spatially averaged storage contents of all HRUs for the modelling period are given in hourly values. The curves show that the middle pore soil storage is the most important one (mostly more than 50 %) in terms of water storage. It represents the usable field capacity of the catchment, the water is kept against gravity in the soil pores. The large pore soil storage has a portion of about 15 %. It is subject to gravity, the water is not kept against gravity in the soil pores. The amount of water which exceeds the maximum infiltration rate of the soil is temporarily stored in the surface depression storage.

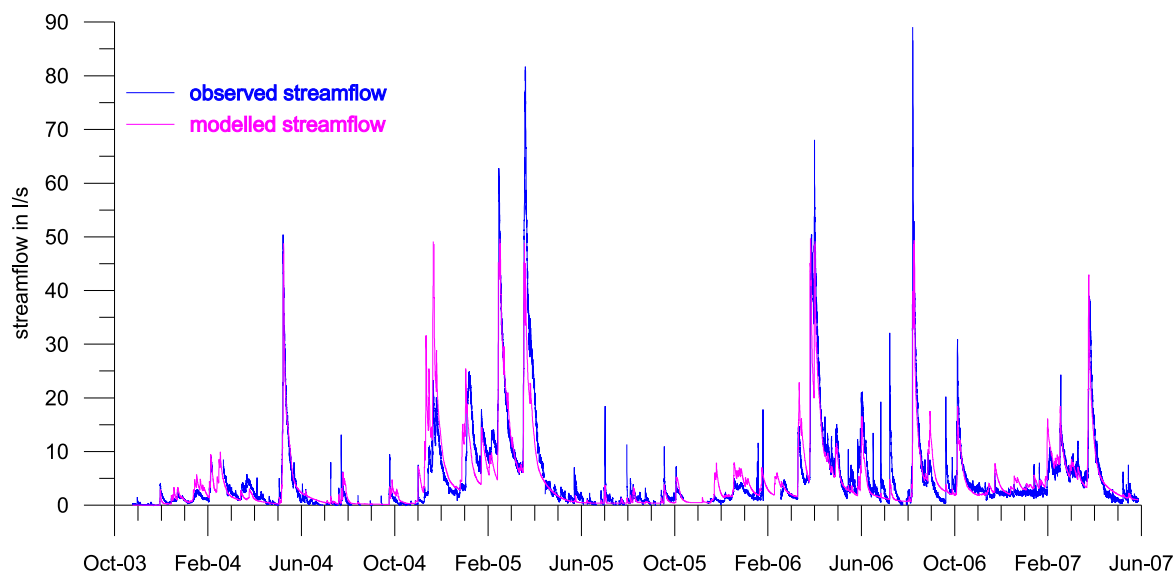


Figure 5.3: Observed and modelled streamflow of the creek Silberleite at the weir at Moxa observatory.

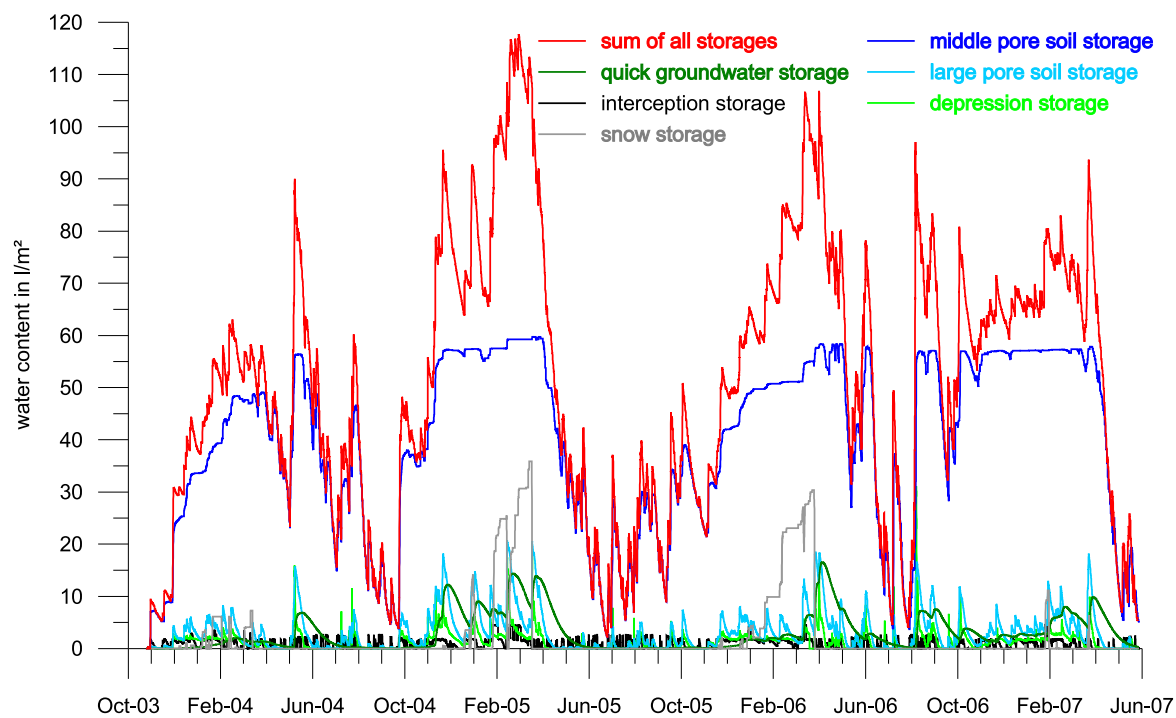


Figure 5.4: Mean water content of all hydrological mass storages, spatially averaged over all HRUs.

The storage contents given in Figure 5.4 visualize the high temporal dynamics of the hydrological state variables in the model. The surface depression storage and the large pore soil storage show an immediate reaction on rain events (cf. Figure 5.3) followed by a quick decay (hours to days). Such quick reaction can be observed for the quick groundwater storage as well. The variations of the middle pore soil storage are more attenuated and show a clear seasonality as of course the snow storage does as well. This seasonality is even more pronounced in the curve of the total sum of all storages, shown as red line in Figure 5.4.

As the model starts with empty storages, some initialization time of about seven months (until May 2004) is needed to balance the stored water content in the various hydrological compartments, resulting in a too low water content in the hydrological mass storages (Figure 5.4). After the heavy rain event in May 2004, the water content stored in the different hydrological storages is balanced.

Additionally to the comparison of the observed streamflow to the modelled one, the storage content of the different soil storages in a HRU was compared to soil moisture measurements at different locations and in different depths. In general, the correspondence between modelled and observed soil water content is good (Krause et al., 2005, 2008), underlining the good quality of the hydrological model.

As mentioned previously, this modelling bases mainly on conceptual approaches. Therefore, it can be applied even if only few measurement data are available. Hence, in contrast to models on a physical base it over-interprets the available data. To build up a hydrological model completely on a physical base is very difficult for the inhomogeneous subsoil and the hilly topography around Moxa observatory. Very first steps in this direction have been made by Niessen & Wesselius (2006) for the water flow in the valley in front of the observatory.

However, the results of the modelling show that the hydrological dynamics in the catchment were modelled fairly well especially regarding the very complex topographic and hydrological situation. Thus, they are appropriate to be used for gravimetric studies.

6 Combination of hydrological and gravimetric modelling

The gravimetric 3D model and the hydrological model are combined to provide modelled gravity time series for comparison to the observations.

6.1 Combined model assembly

Because hydrological particularities in the direct vicinity of the gravimeter sites have a greater impact on the gravity data than those in some distance, the area of the combined modelling was split into two parts (Figure 6.1): an inner part up to a distance of approximately 250 m from the observatory and an outer part comprising the remaining part of the gravimetric model.

In the Figures 6.2 and 6.3 plane 19 of the gravimetric 3D model is given again. Within a distance up to 250 m from the observatory, the disaggregated bedrock and the soil layer were subdivided into small single bodies which represent the respective hydrological response units of the hydrological model. The complete inner part of the gravimetric model, which is classified into hydrological response units, is given in Figure 6.4. The observatory is situated in the centre of this region. The hydrological response units are embedded in the triangulation of the other parts of the gravimetric model (Figure 6.5). The complete model comprises 28,729 triangles distributed in and between 38 vertical planes. 10,398 vertices build up 97 bodies. 41 of these bodies correspond to the hydrological response units of the soil layer, and 41 to the disaggregated bedrock.

6.2 Translation of hydrological mass changes into density variations

The output of the local process-oriented hydrological model, storage changes in hourly time steps for the different storages in each HRU, is converted into density changes of the respective bodies of the gravimetric model for each time step. Hereby, water storage changes given as volume per area [l/m^2] are translated to density changes [kg/m^3] assuming a density ρ_w of the water of $\rho_w = 1000 \text{ kg/m}^3$ and applying the thickness of the soil layer and the disaggregated bedrock from the gravimetric model as depth information to these figures.

In the zone of approximately 250 m around the observatory the response units of the hydrological model were transferred directly to bodies of the gravimetric 3D model (Figure 6.1). For each HRU, the modelled water mass storage variation was applied as density change of the respective soil and disaggregated bedrock HRU body of the gravimetric model. Hereby, for the soil HRU bodies the sum of the variations of the middle and large pore soil storage, interception storage, snow storage, and depression storage was always applied whereas for the HRU bodies of disaggregated bedrock the variations of the groundwater storage were used.

In greater distances (250-1000 m) from the observatory the hydrological dynamics influences

gravity to a lesser degree. In addition, these regions can be assumed to be largely homogeneous regarding hydrological properties as derived from measurements. To hold the model as simple as possible without loss of accuracy, spatially averaged water storage variations of all HRUs of the hydrological model, shown in Figure 5.4 in Section 5, were applied to the soil layer and disaggregated bedrock bodies of the gravimetric model in this outer region. In this region, for the soil layer the sum of the variations of the middle and large pore soil storage, interception storage, snow storage, and depression storage was always applied whereas for the layers of disaggregated bedrock the variations of the groundwater storage were used.

By the coupling of the local hydrological model with the gravimetric one, gravity effects caused by hydrological mass variations were computed for each gravity observation site, time step, and version of the gravimetric model (cf. Section 4.6).

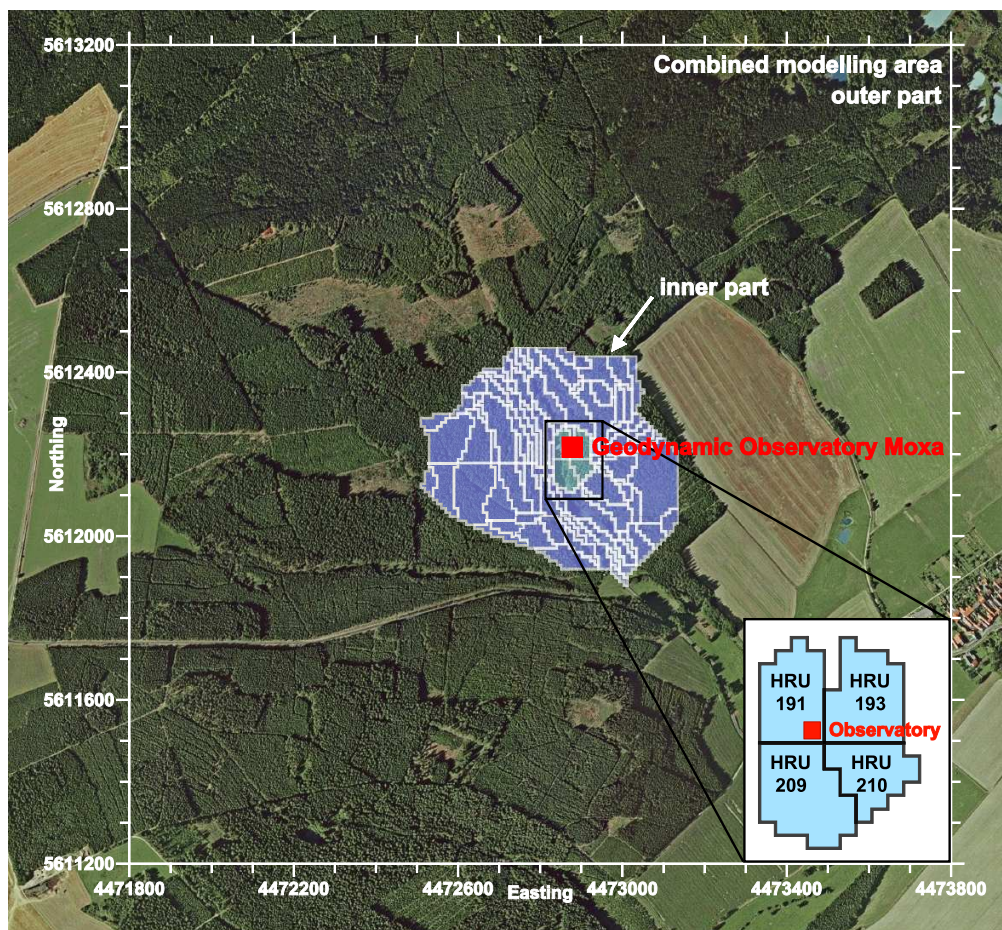


Figure 6.1: Combined gravimetric and hydrological modelling area and HRUs in the observatory surroundings. The complete modelling area covers $2 \times 2 \text{ km}^2$. The outer part of the model is marked by the white box, the HRUs in the inner part within a distance of 250 m around the observatory in dark blue. The HRUs 191, 193, 209, and 210 are marked light blue, they comprise an area within a radius of about 90 m around the observatory. The aerial photograph was taken from [Google Earth \(2008\)](#).

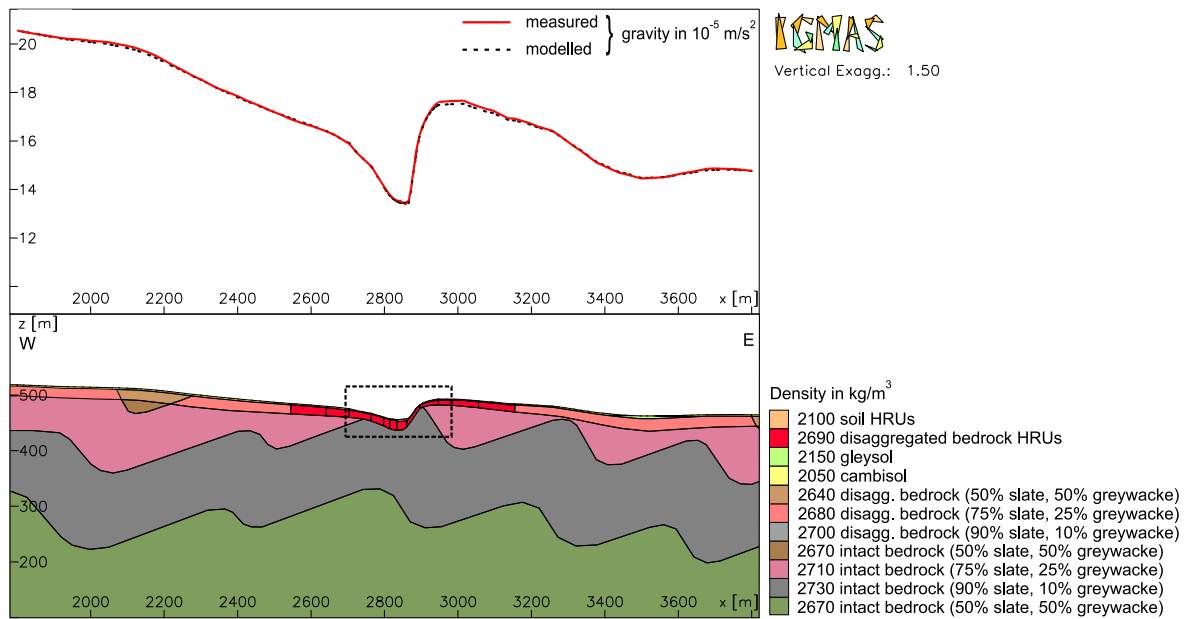


Figure 6.2: Plane 19 (through observatory, cf. Figure 4.5) of the gravimetric 3D model including besides topography and the layers given in Figure 4.6 also the bodies (HRUs) of the hydrological model up to a radius of 250 m around the observatory. The dotted box marks a detail of plane 19 which is given in Figure 6.3. In the upper part the observed and modelled free-air anomaly is shown.

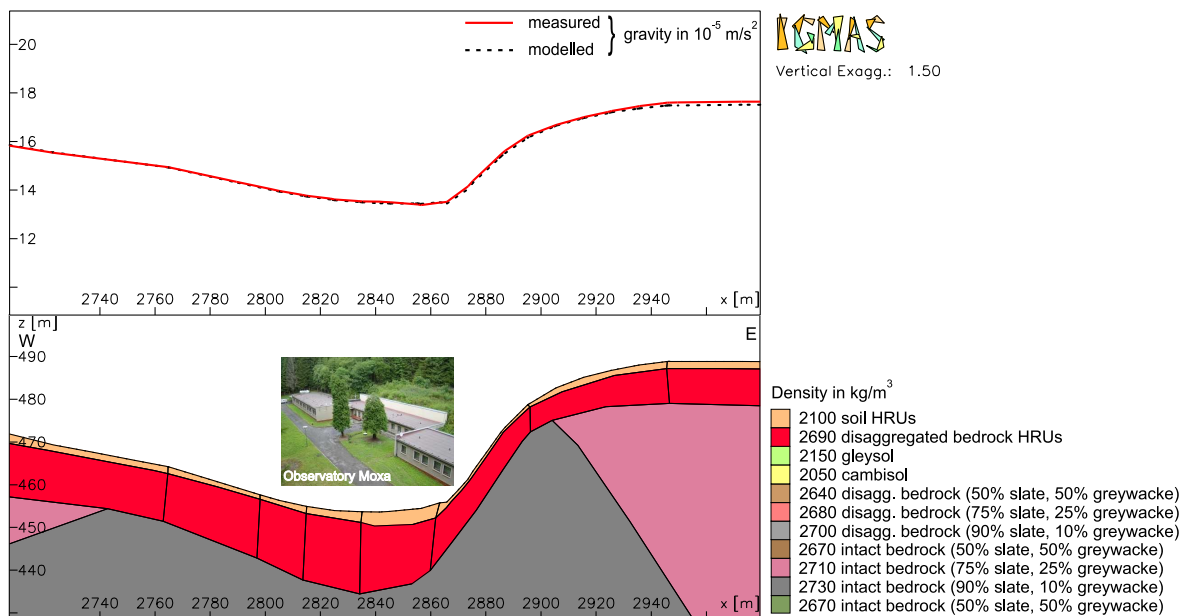


Figure 6.3: Detail of plane 19 showing in particular the HRUs of the hydrological model in the direct vicinity of the observatory corresponding to the soil layer (orange) and the disaggregated bedrock (red).

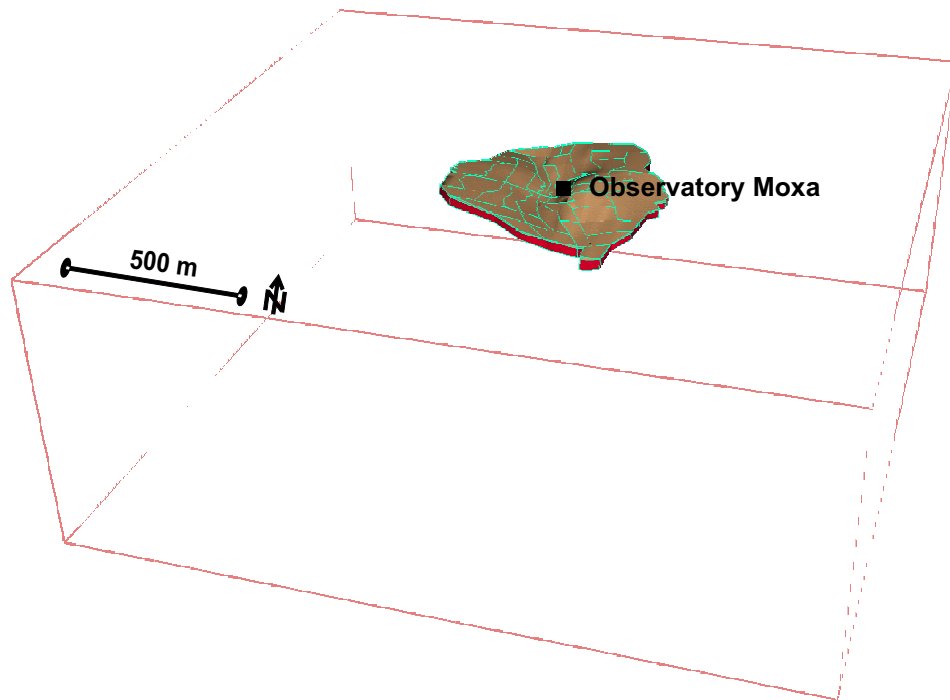


Figure 6.4: HRUs of the inner part of the hydrological model which are included into the gravimetric model for the soil layer and the disaggregated bedrock up to a distance of 250 m from the observatory. Legend is given in Figure 6.2.

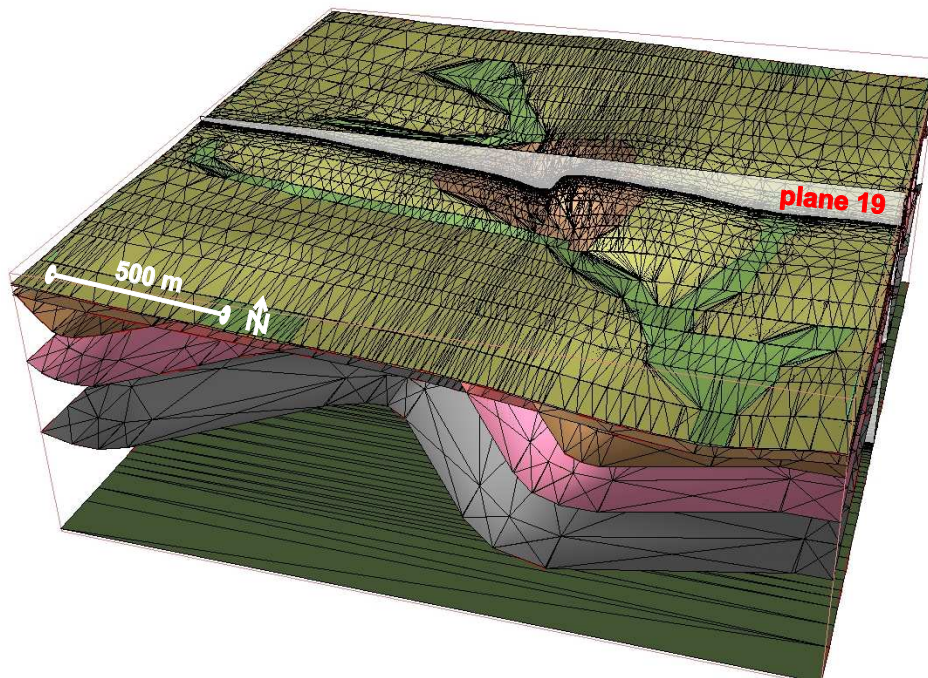


Figure 6.5: Triangulation of the surfaces of the gravimetric 3D model including the HRUs in the inner part (cf. Figure 6.4) and position of plane 19 (cf. Figures 4.5 and 6.2) within the model. Legend is given in Figure 6.2.

7 Results

From the combined hydrological and gravimetric modelling temporal gravity changes due to hydrological variations were derived. For the gravity differences between the points of the local network these gravity changes are presented in Section 7.1, and for the location of the superconducting gravimeter in Section 7.2.

7.1 Local gravity network MoxaNet

The modelled temporal gravity changes for the differences between the points of the local gravity network are shown in the Figures 7.1 and 7.2 for the model versions 1–5 which were described in Section 4.6. For comparison, the results of the observations on the local network (Section 3.3) are given in the Figures 7.1 and 7.2 as well.

The modelled gravity differences generally show high temporal dynamics. Changes of several 10 nm/s^2 were derived in most differences. Peaks after rain events are followed by a decay due to the water runoff. A seasonal signal can also be identified in the modelled differences reflecting a generally dry situation in summer and a wet situation in winter months.

7.1.1 Differences to the observation site on the hill

In the modelled gravity differences which include point *ET* on the hill (Figure 7.1 a–e), the largest changes occur. This is in agreement with the repeated gravity observations. The seasonal variations are very pronounced. During wet conditions in winter, the modelled gravity differences are several 10 nm/s^2 smaller than in dry summer months. The changes are maximum in the differences *SG-ET* and *AG-ET*, and smaller in the differences *MB-ET* and *WE-ET*.

Exemplarily, the changes between the campaigns 5, 6, 8, 9, and 11 are described for these differences. The campaigns 5 and 9 were carried out during snow melt in the years 2005 and 2006, the campaigns 6, 8, and 11 in the dry summers. Between campaigns during snow melt and those in the following dry summer (between campaigns 5 and 6, as well as 9 and 11) a clear increase is found in the modelled gravity differences corresponding to the observed variations. This increase is maximum for the differences *SG-ET* and *AG-ET*; it reaches 160 nm/s^2 . Between campaigns 8 (dry summer) and 9 (snow melt) the modelled as well as the observed differences decrease consistently. These changes can only be explained by hydrological processes which occurred between the points. Thus, hydrological processes in the hill slope have a crucial impact on the gravity differences.

The modelled as well as the observed changes in the differences *SG-ET* and *AG-ET* are by a factor of 2 larger than the changes in the differences *MB-ET* and *WE-ET*. Because the points *SG* and *AG* are located directly at the foot of the steep slope and the points *MB* and *WE* in the middle of the valley, this result is another argument for strong hydrological variations in the steep slope.

7.1.2 Differences to the measurement point on the observatory roof

The differences from points in the observatory valley to point *DA* on the roof, given in Figure 7.2 a–d, also show seasonal variations. They do, however, not behave uniformly and only partially match the observations. In general, the modelled variations are by a factor of 2 to 3 smaller than the changes in the differences to the point *ET*. For the differences from the points outside the observatory building approximately in the middle of the valley (*WE-DA* and *MB-DA*) only small variations of less than 40 nm/s^2 were derived from the modelling, whereas the observations showed changes up to 95 nm/s^2 . In contrast, the modelled differences from the points in the building at the steep slope (*AG-DA* and *SG-DA*) show larger variations up to 100 nm/s^2 widely corresponding to the observations.

These results indicate that either the points *WE*, *MB*, and *DA* are situated in a similar hydrological regime which is not confirmed by the observations, or the hydrological dynamics in the observatory valley – in particular between these points – are only partially reproduced by the hydrological model. This result is supported by the higher standard deviations between observation and modelling (Table 7.1) for these differences.

7.1.3 Differences between the stations in the valley

The changes in the differences between the measurement points in the valley are given in Figure 7.1 f–g, and Figure 7.2 e–h. For the differences *AG-SG* and *WE-MB* (Figure 7.1 f–g), changes of less than 20 nm/s^2 were derived from the modelling which generally correspond to the observations. These small changes may be caused by the particular location of the gravity sites – both points *AG* and *SG* located in the observatory building, both points *WE* and *MB* outside, each pair of points always close together in an almost identical hydrological regime and in a similar distance to the steep slope as described in Section 3.3. Hence, the seasonal variations nearly completely vanish in these differences.

In the differences *WE-SG*, *MB-SG*, *WE-AG*, and *MB-AG* (Figure 7.2 e–h) – always one point of the difference in the observatory building close to the slope and one outside – changes of about 80 nm/s^2 maximum were derived from the modelling which also agree to the observations. In these differences the seasonal signal is visible. During wet conditions in winter months the modelled gravity differences are approximately 60 nm/s^2 larger than in dry summer months. The seasonal signal in these differences points in the opposite direction as in the other differences which depends on the definition of the minuend and the subtrahend in the calculation of the differences. As mentioned previously, in the calculations for the MoxaNet, always the locations with higher gravity values enter the difference as minuend, and the stations with lower gravity values as subtrahend.

These results show that the hydrological situation at and between these observation points is correctly implemented in the hydrological model. This is also confirmed by the small standard deviation of 24.5 nm/s^2 between observations and modelling results for model version 3 for the differences in the valley (Table 7.1).

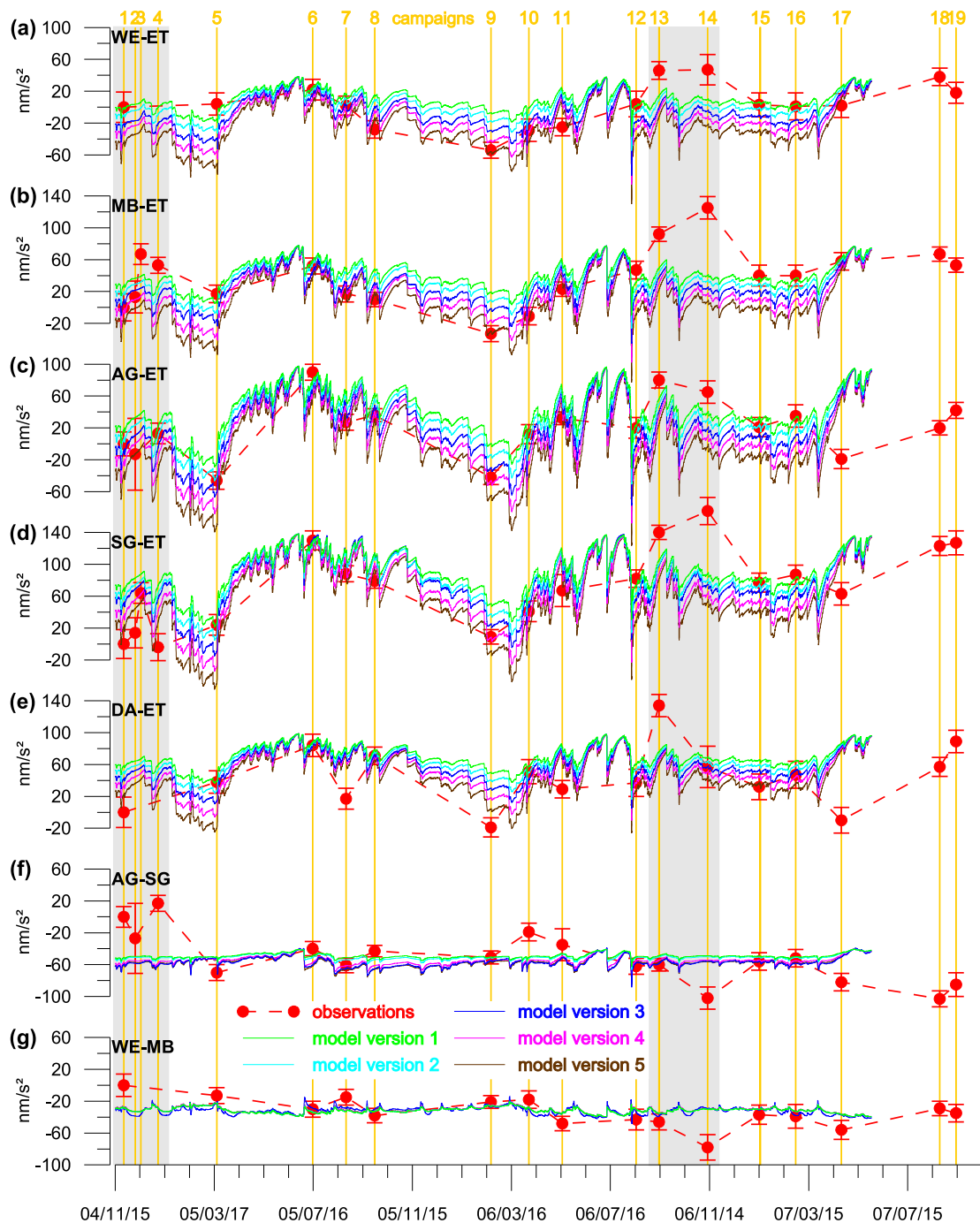


Figure 7.1: Temporal changes in the observed gravity differences with standard deviation (red circles) and modelled hydrologically induced variations for 5 different model versions (cf. Table 4.2). (a–d) observed and modelled gravity changes in the differences between several points in the valley in different distance to the steep slope and point *ET* on the hill; (e) observed and modelled gravity changes in the difference between point *DA* on the observatory roof and point *ET*; (f–g) observed and modelled gravity changes in the differences *AG-SG* (both points inside the observatory building) and *WE-MB* (both points outside the observatory building, cf. Figure 2.8). The grey boxes mark measurement campaigns with reduced data quality.

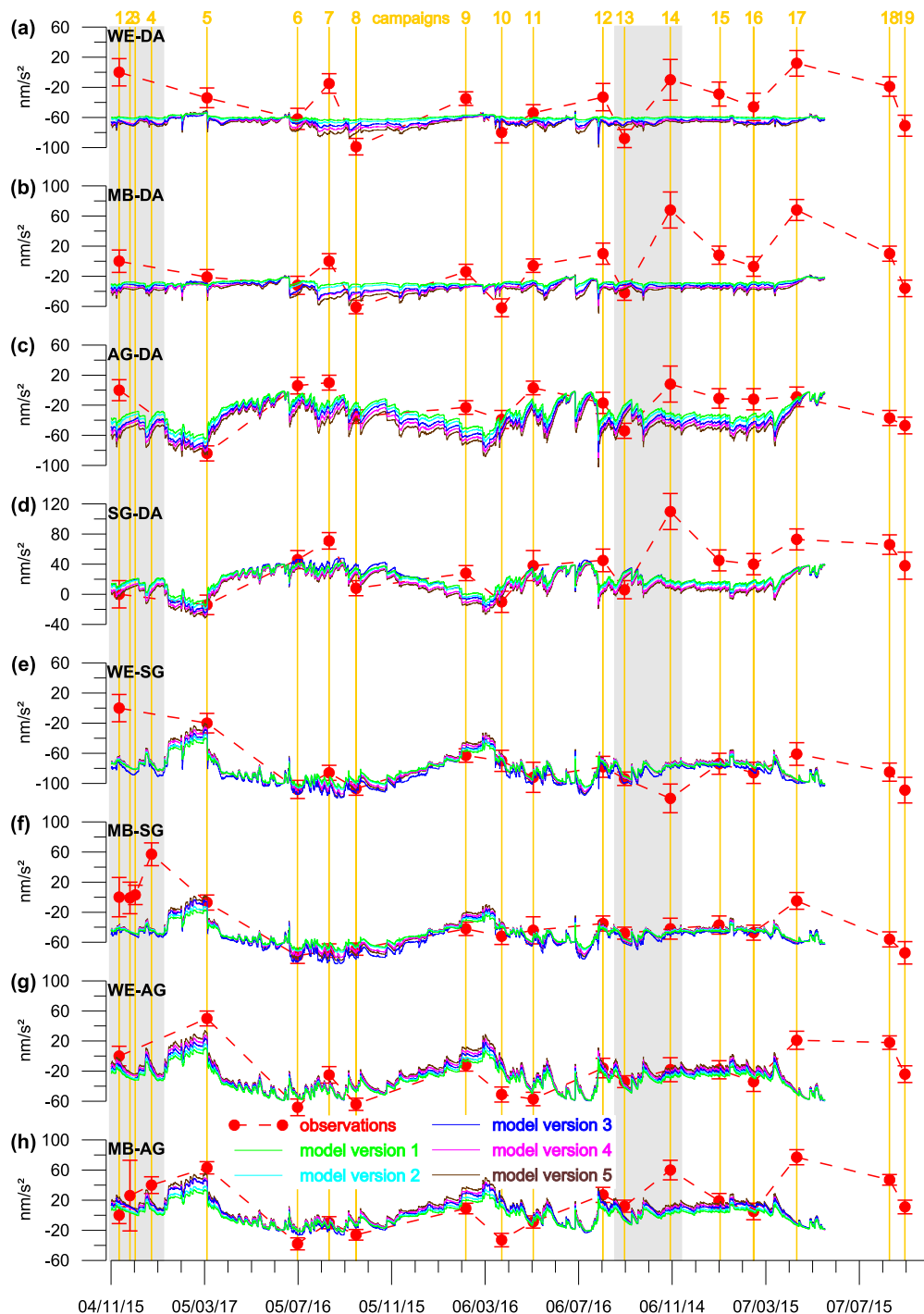


Figure 7.2: Temporal changes in the observed gravity differences with standard deviation (red circles) and modelled hydrologically induced variations for 5 different model versions (cf. Table 4.2). (a–d) observed and modelled gravity changes in the differences between several points in the valley in different distance to the steep slope and point *DA* on the observatory roof; (e–h) observed and modelled gravity changes in the differences between points in the valley (always one point inside and the other outside the observatory building, cf. Figure 2.8). The grey boxes mark measurement campaigns with reduced data quality.

However, at some campaigns the observed and modelled gravity changes significantly differ from each other, for example in the difference *MB-AG* (Figure 7.2 h) between the campaigns 9 and 10. This might be explained by the fact that the observation sites *AG* and *SG* are situated inside the observatory building where the soil is sealed. Hence, no water can infiltrate in the subsoil in this area. Below the observatory building, however, water flow is observed during heavy rain events and snow melt as discussed by Kroner et al. (2007) and proved by the experiment described in Section 3.2.3.2. Thus, a special short-term impact on the local hydrological processes must be expected which seems to be not yet sufficiently considered in the hydrological modelling. According to this result the hydrological modelling may be modified.

7.1.4 Standard deviations for the different model versions

Between the results of the different modelling versions (Table 4.2) of the gravimetric model significant deviations of up to 80 nm/s^2 occur generally during wet situation in winter. Model version 1 shows the smallest variations, whereas the variations caused by model version 5 are by a factor of 2 larger. The variations of the model versions 2–4 are in between.

Between all adjacent campaigns, in all gravity differences, and for all model versions the difference between modelled and observed gravity changes between two campaigns was calculated. The campaigns 1–4 were excluded from the calculations because the network design was changed during these campaigns and different instruments were tested in order to reach a higher quality of the observations as well as an effective measurement procedure (cf. Section 3.3.4.1). In campaign 13 strong wind influenced the measurements and reduced the accuracy, and in campaign 14 an earthquake disturbed the measurements. In this campaign the network could be covered only partially resulting in results of lower quality. The standard deviation of the discrepancies between observed and modelled gravity changes is given in Table 7.1 for each model version.

In Table 7.1 b only the differences between the campaigns 5 and 6 were used for calculation, and in Table 7.1 c only the differences between the campaigns 8 and 9. These campaigns were chosen because they represent examples for large and significant gravity changes. As discussed in Section 3.3, the campaigns 5 and 9 were carried out during snow melt whereas the campaigns 6 and 8 took place in the dry summer.

From the standard deviations in Table 7.1 a it can be derived that the results from model versions 3 and 4 of the combined hydrological and gravimetric modelling correspond to the observations best. This shows clearly that the results of the hydrological modelling most appropriate match the gravity observations if and only if the gravimetric model fulfills the boundary conditions best of all. In model version 3 the lowest standard deviation of 25.0 nm/s^2 was obtained for all differences in all considered campaigns. Whereas for model version 4 a small standard deviation of 25.1 nm/s^2 was obtained as well, for model version 2, and, in particular 1 and 5, the standard deviation is higher. Model version 1 underestimates the observed changes, model version 5 overestimates them. These model versions are not realistic and can be excluded from further considerations because of two reasons: they do only

Table 7.1: Standard deviations σ of the discrepancies between the observed and modelled gravity differences in the local network.

Considered campaigns	σ in nm/s^2 for the model versions				
	1	2	3	4	5
(a) Differences between all campaigns					
all	25.8	25.3	25.0	25.1	25.4
in the valley	24.7	24.6	24.5	24.6	24.7
to point <i>ET</i>	28.2	26.3	25.8	26.1	26.8
to point <i>DA</i>	31.2	31.1	31.0	31.0	31.2
(b) Differences between campaigns 5 and 6					
all	29.1	27.0	23.9	23.4	25.3
in the valley	25.0	31.3	29.8	26.7	24.5
to point <i>ET</i>	24.1	20.5	17.0	17.5	26.8
to point <i>DA</i>	23.1	22.0	19.6	18.7	31.2
(c) Differences between campaigns 8 and 9					
all	22.4	21.5	20.6	20.8	22.3
in the valley	24.8	23.4	22.8	23.0	23.3
to point <i>ET</i>	20.3	17.5	16.3	14.6	16.1
to point <i>DA</i>	36.7	34.8	33.2	36.1	36.3

marginally reflect the boundary conditions (Section 4.3) and the standard deviation of the discrepancies between measured and modelled free-air anomaly in the gravimetric model is higher than those of the other model versions (Table 4.2).

The standard deviations considering only the differences within the valley, to the point on the hill, and to the point on the roof are also given in Table 7.1. It can be noticed that the standard deviations are minimum for the differences in the valley and maximum for the differences to the observatory roof, which may be due to the small gravity changes between the points in the valley and the exposed and often windy point location on the observatory roof.

Considering only the gravity changes between campaigns 5 and 6 as well as 8 and 9 in the calculation of the standard deviations (Table 7.1 b and c), it is generally confirmed that model versions 3 and 4 best match the observations. The standard deviations obtained for the changes between these campaigns are mostly some nm/s^2 smaller than between all campaigns, underlining that the modelling as well as the observed gravity changes reproduce seasonal variations well. The only exception is the unusual high deviation of 29.8 nm/s^2 in the differences in the valley between campaigns 5 and 6. Apparently, the modelling matches the observed changes in the differences between the points in the valley between these two campaigns not as well as the changes to the other points. However, between the other campaigns this is not the case.

There are two possible explanations from which also possible modification of the hydrological model can be derived: First, the hydrological model has difficulties at extreme hydrological events like snow melts (cf. Section 5). Second, the observatory building is not explicitly considered in the hydrological model.

7.1.5 General findings

In general, the modelled gravity variations reflect the observed changes well within the standard deviations of the observations. However, at campaign 14 and partially at the campaigns 1–4 and 13 the modelled changes do only marginally or partially reproduce the observed gravity changes. This may be due to changes in the network design and an earthquake during campaign 14 as mentioned previously. As already discussed, here the observations are of lower quality and do not match the modelled seasonal variations. Additionally, in Figure 7.1 and 7.2 the (simple) standard deviation of the observations (68 % of the observations are covered) is given. Taking into account twice the standard deviation (95.5 % of the observations are covered) most of the modelling results (exception: campaign 14) are within this error bar of the observations.

For the other campaigns the modelled changes are in the correct order of magnitude and point in the same direction as the observations. Thus, the modelled hydrological changes generally well mirror the hydrological changes in the surroundings of the gravity observation sites for most campaigns and in most differences. In particular, the changes in the differences between points in the observatory valley and point *ET* can be satisfactorily explained. The modelling reproduces the variations in the differences between points within the Silberleite valley also very well; the standard deviation between observation and modelling is 25.0 nm/s^2 . The observed changes in the difference *SG-ET*, however, are only partially reproduced by modelling. This may be due to the fact that the sealed floor in the observatory building is not implemented as an own HRU in the hydrological model.

The modelled variations in the gravity differences from points in the valley to the point on the hill are by a factor of about 2 to 3 larger than the variations in the differences to the observatory roof or in the valley. This supports the results of the observations that, in particular, hydrological processes in the steep slope east of the observatory between the points in the valley and point *ET* on the hill have an important impact on the gravity differences. Because the differences from the observatory roof to the points in the valley as well as to the point on the hill show large variations, these hydrological processes must be active above and below the level of the observatory roof. This indicates that water flow processes in the hill may occur between these points. Because the gravity differences in the MoxaNet cannot be observed continuously, this assumption cannot be checked by the repeated measurements, only by the recordings of the superconducting gravimeter. It was tested by the irrigation experiment, discussed in Section 3.2.3.3.

Because always temporal changes in the gravity differences between two gravity sites were analysed, only local hydrological variations are reflected in the differences. An effect of regional or global hydrological variations was avoided. Thus, the local hydrological signal could be separated from regional or global changes.

7.2 Superconducting gravimeter

Further information especially on short-term hydrological changes due to rain events and water flow processes can be gained by comparing the gravity residuals of the superconducting gravimeter to the modelled local hydrological effect for the location of this instrument. First the influence from different local zones around the superconducting gravimeter on the local hydrological effect is given.

7.2.1 Hydrological contributions from various zones around the gravimeter

To gain more information on not only seasonal but also short-term hydrological influences on the superconducting gravimeter, the influencing areas need to be studied. The contributions from different local zones around the gravimeter on the local hydrological effect are given in Figure 7.3 and 7.4. The results of the modelling are shown for version 3 of the gravimetric model. In the modelled hydrological effect a seasonal signal can be identified, with maximum amplitudes in the winters 2005 and 2006 and smaller amplitudes in the winters 2004 and 2007, mainly caused by high soil water content, snow cover, and snow melt. The effect has a negative sign because most of the surroundings of the observatory is above the gravimeter level as described in Section 3.2. Besides the seasonal signal also a hydrological influence of single rain events is visible.

In the direct vicinity of the observatory within a radius of 90 m around the gravimeter, the four HRUs 191, 193, 209, and 210 of the hydrological model are located (Figure 6.1). The hydrological effect of these HRUs, given in Figure 7.3, amounts to -16 nm/s^2 in winter 2005. The data show a maximum influence of -6 nm/s^2 from the HRU 193 which covers an area of about 3200 m^2 and is situated completely above the level of the superconducting gravimeter. Because HRU 210 covers an area of only 2300 m^2 and is in some distance to the gravimeter (cf. Figure 6.1) a smaller influence of maximum -3 nm/s^2 was modelled. The HRUs 191 and 209 cover a large area of 2800 m^2 and 3700 m^2 . They are located closest to the gravimeter and their area covers regions below and above the level of the gravimeter. Thus, the hydrological effects on the gravimeter site partially compensate resulting in a minor influence of about -3 nm/s^2 for HRU 191 and -4 nm/s^2 for HRU 209 (Figure 7.3).

The hydrological effect on gravity (model version 3) in the local catchment (up to a distance of 1000 m from the gravimeter) is shown in Figure 7.4 for the period from December 2003 to May 2007. The maximum amplitude of this effect amounts to -54 nm/s^2 . The maximum effect of the HRUs in a radius of 90 m around the gravimeter is -16 nm/s^2 . This corresponds to 30 % of the local hydrological effect. The influence of the HRUs in a zone between 90 and 250 m around the observatory is maximum -21 nm/s^2 . Thus, this area takes a proportion of 39 % of the entire local hydrological effect modelled here. The area in the zone between 250 and 1000 m around the observatory contributes a maximum effect of -17 nm/s^2 to the entire effect, which corresponds to 31 % (Figure 7.4). Therefore, 70 % of the modelled local hydrological effect originate from an area within a radius of 250 m around the observatory.

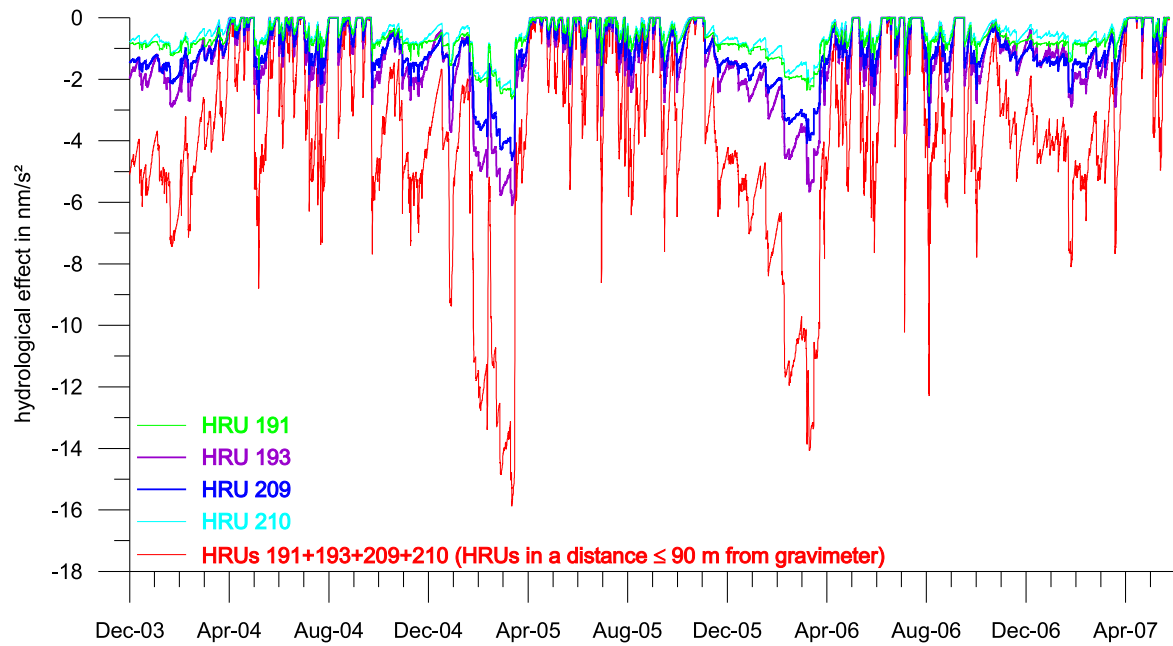


Figure 7.3: Contributions to the local hydrological effect in gravity from the HRUs 191, 193, 109, and 210 as well as the sum of these HRUs (cf. Figure 6.1), which build up a zone of approximately 90 m around the superconducting gravimeter at Moxa observatory for version 3 of the gravimetric model (cf. Table 4.2).

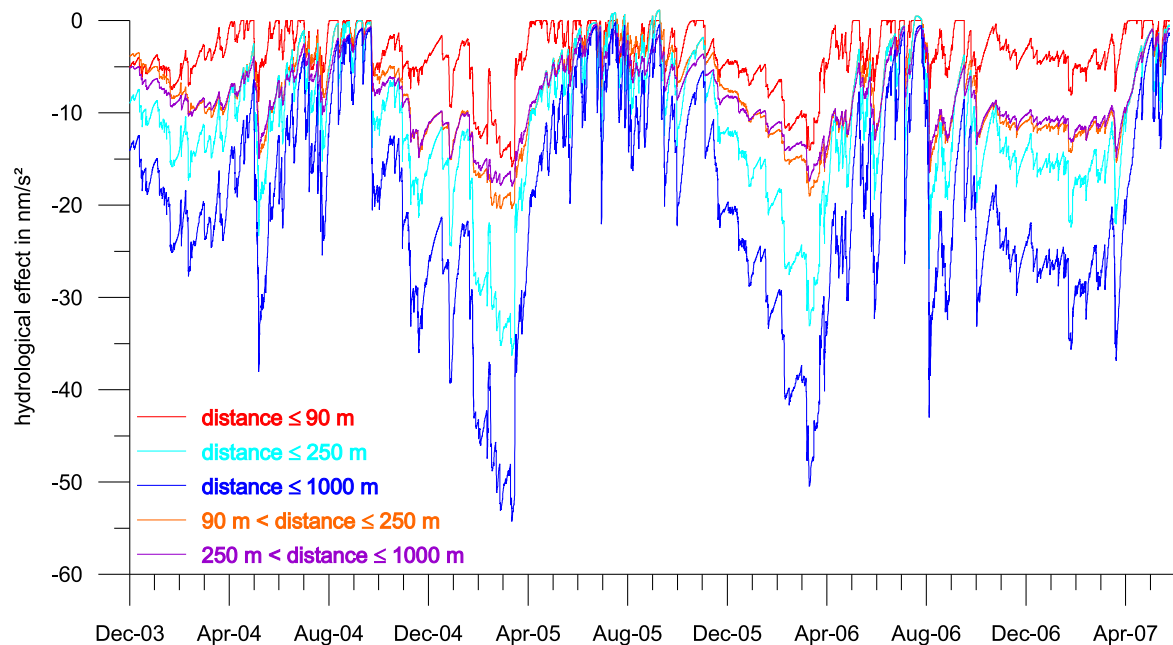


Figure 7.4: Contributions to the local hydrological effect in gravity from different zones around the superconducting gravimeter at Moxa observatory (cf. Figure 6.1, 7.4) for version 3 of the gravimetric model (cf. Table 4.2).

7.2.2 Seasonal variations

In the same way as for the gravity stations of the MoxaNet (Section 7.1), the impact of different thicknesses of the soil layers and the disaggregated bedrock on the hydrological effect for the location of the superconducting gravimeter was studied, but here not for gravity differences but for gravity changes at one point, the location of the superconducting gravimeter. The results for these model versions are shown in Figure 7.5 a. For model version 3, a maximum amplitude of -54 nm/s^2 was derived for the entire local hydrological effect. For model version 4 this amplitude is -61 nm/s^2 . Therefore, the maximum (seasonal) hydrological effect between model version 3 and 4 varies by maximum 7 nm/s^2 or 13 %. Because of the

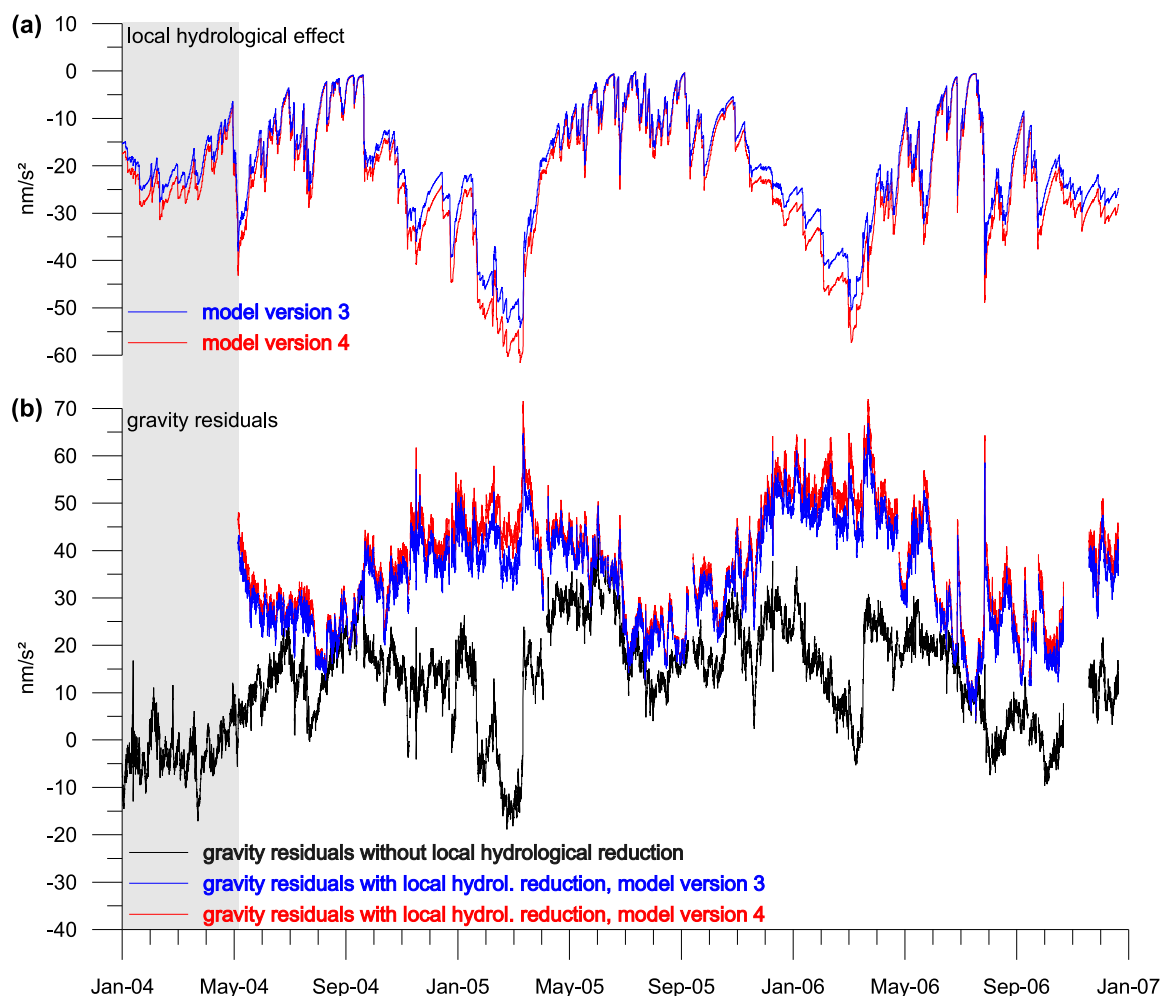


Figure 7.5: Local hydrological effect and gravity residuals: (a) local hydrological effect derived from the local hydrological and gravimetric model for the location of the superconducting gravimeter at Moxa observatory; (b) gravity residuals of the superconducting gravimeter without and with local hydrological reduction. The grey shaded box marks the initialisation period of the hydrological model.

initialisation period of the hydrological model, discussed in Section 5, the local hydrological effect is not considered completely in the first months of the modelling period. Thus, the seasonal effect of the winter 2003/2004 is underestimated and not realistic until the heavy rain event in May 2004. The effect from this first modelling period is not applied to the superconducting gravimeter data.

The gravity residuals of the superconducting gravimeter as described in Section 3.2 without any hydrological reduction are given in Figure 7.5 b for the period between January 2004 and December 2006; for the year 2007 the 3D barometric pressure reduction is not yet available. From these data the local hydrological effect – computed with the model versions 3 and 4 – was subtracted. In the resulting gravity residuals in Figure 7.5 b, a seasonal variation becomes clearly visible which was hidden before. It has a minimum/maximum amplitude of approximately 30 nm/s^2 for model version 3, and 35 nm/s^2 for model version 4, respectively. Because only these two model versions reflect the boundary conditions and match the observations in the MoxaNet, the uncertainties in the local hydrological reduction can be quoted to about $\pm 2.5 \text{ nm/s}^2$ for seasonal variations. The seasonal variations are due to regional and global hydrological fluctuations. They were masked in the original gravity data by local hydrology. Particularly during wet winter months this local masking-effect is strongly developed.

7.2.3 Rain events and snow melt

A detail of the time series of the modelled local hydrological effect and the gravity residuals from Figure 7.5 over a summer period of two months from 04/05/26 to 04/07/27 is given in Figure 7.6. The modelled local hydrological effect is shown in Figure 7.6 a along with precipitation data for comparison. The corresponding gravity residuals are given in Figure 7.6 b.

About a dozen rain events occurred during this period, giving clear signals in the modelled local hydrological effect and causing variations in the range of up to -23 nm/s^2 for model version 3, and -26 nm/s^2 for version 4, respectively. Single rain events caused a local hydrological effect of up to -12 nm/s^2 for model version 3, and -14 nm/s^2 for version 4. The distinct diurnal variation in the local hydrological effect (looking like smoothed steps) computed from the combined hydrological and gravimetric modelling originates from the fact that evaporation is active at day and only subsidiarily at night. In the Moxa area up to 70 % of the rain water evaporate as mentioned in Section 3.2.2.

Rain events can be clearly identified as strong gravity drops of some nm/s^2 in the gravity residuals without local hydrological reduction. Some rain events are marked with yellow arrows in Figure 7.6, e.g. on 04/06/01 or on 04/07/18. After subtraction of the modelled local hydrological influence from the gravity residuals, the effect of the rain events is largely reduced.

However, the effect of rain events is not always fully eliminated from the gravity data as e.g. on 04/07/08. In general, about 10 to 15 % of the variations caused by rain events still remain in the data. This value is not constant for all rain events, but varies significantly. Small rain

events, which last only some hours or less and accumulate a precipitation of only a few mm/h are nearly completely reduced. In contrast, at larger rain events up to 20 % of the gravity variations remain in the data. Apparently, heavy rain events are partially reproduced time-delayed by the hydrological model, resulting in strong (amplitude up to 10 nm/s^2) but short-term peaks in the respective local hydrology reduced gravity data (Figures 7.5 b and 7.6 b). This may be due to the lateral routing of the water mass flow in the hydrological model as discussed in Section 5 and indicates that the implementation of the local hydrological situation is not complete as already discussed in Section 7.1.

To describe the remaining uncertainty regarding rain events between reduced and unreduced gravity data quantitatively, 115 rain events in the period between May 2004 and December 2006 were selected and the remaining hydrological effects in the reduced gravity data at and after the rain events was determined. The arithmetic mean of these remaining effects amounts to $\pm 1.5 \text{ nm/s}^2$. Thus, the reduction of the local hydrological effect can be considered as successful not only for seasonal variations but also for single rain events.

A detail of the time series of the modelled local hydrological effect and the gravity residuals

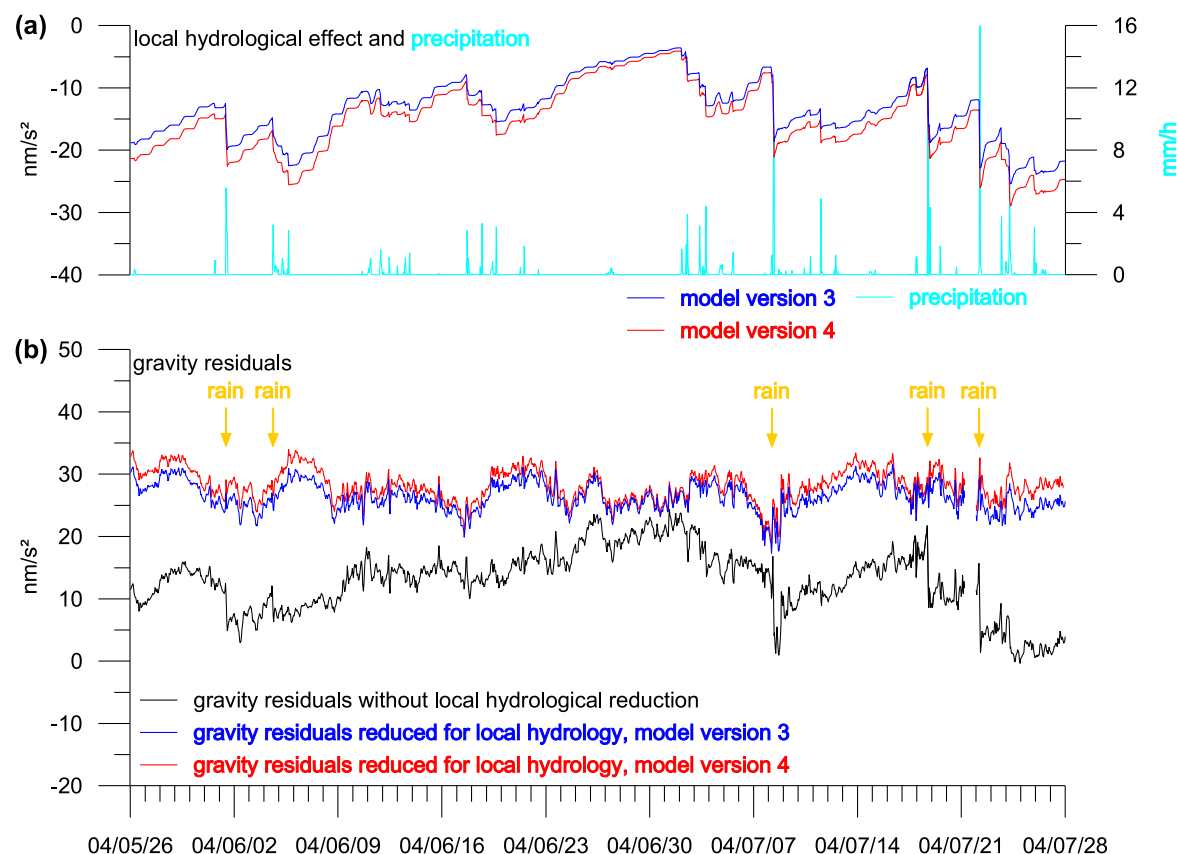


Figure 7.6: Detail of Figure 7.5 for the summer period from 04/05/26 to 04/07/27. **(a)** modelled local hydrological effect and precipitation data for comparison; **(b)** gravity residuals without and with local hydrological reduction. The yellow arrows mark some rain events.

from Figure 7.5 over a period of three months in winter 2005 is given in Figure 7.7. The modelled local hydrological effect is shown in Figure 7.7 a along with precipitation data for comparison. The corresponding gravity residuals are given in Figure 7.7 b. In general, the local effect of snow cover and melt is largely decreased by the local hydrological reduction. However, the strong gravity changes due to snow melt in 2005 (but also in 2006, cf. Figure 7.5) cannot be fully explained by the current local hydrological reduction. Besides the strong gradients after rain events, in particular, the strong gravity gradients at snow melt mid-March 2005 is time-delayed and not fully reproduced by the hydrological model, resulting in a temporal peak with an amplitude of up to 15 nm/s^2 in the respective local hydrology reduced gravity data (Figures 7.5 b and 7.7 b). Regarding these findings, the local hydrological model needs to be modified. Nevertheless, as most important point the application of combined hydrological and gravimetric modelling was successful. For both rain events and seasonal changes a crucial reduction of the local hydrological influence was obtained.

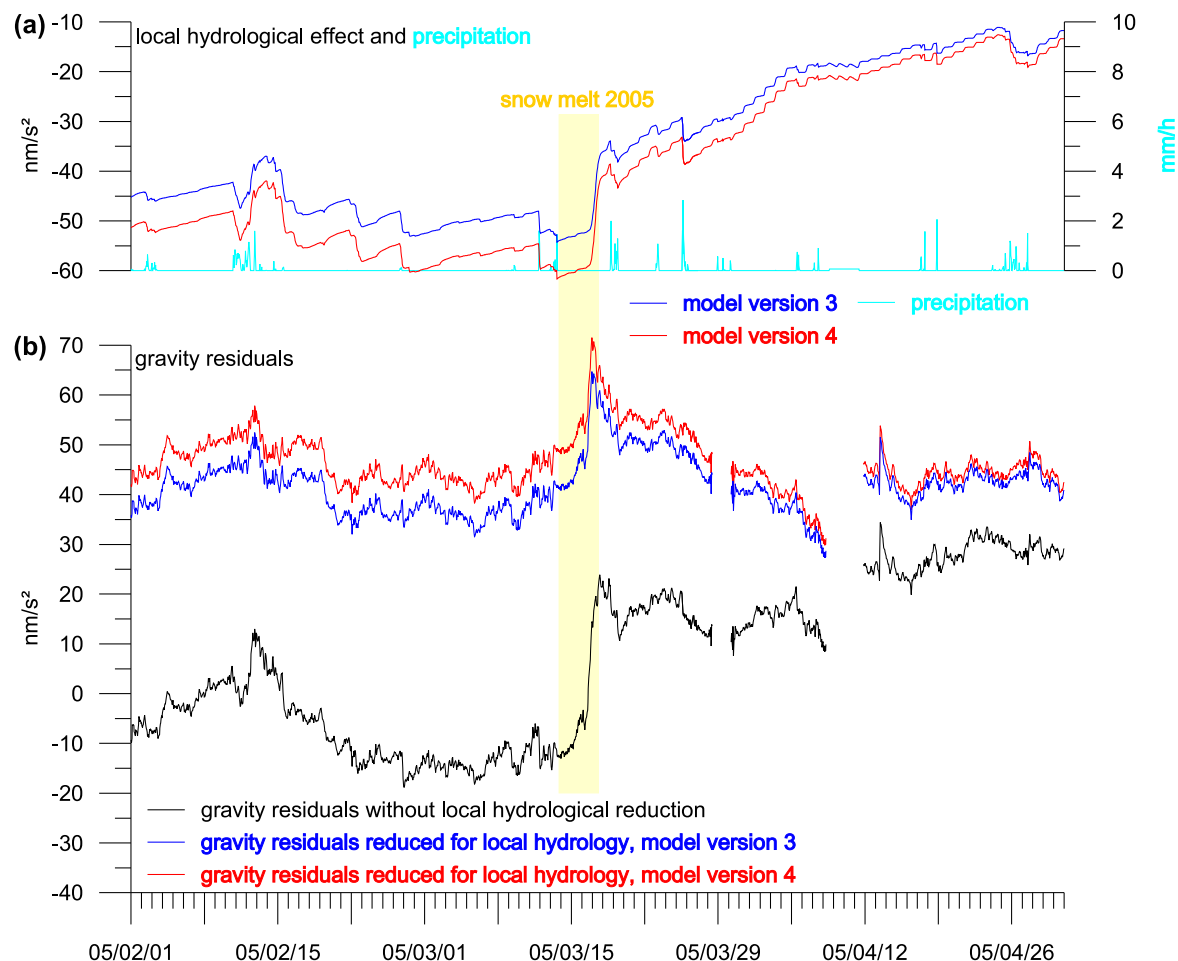


Figure 7.7: Detail of Figure 7.5 for the winter period from 05/02/01 to 05/04/30. (a) modelled local hydrological effect and precipitation data for comparison; (b) gravity residuals without and with local hydrological reduction.

8 Discussion of the results and conclusions

Time-dependent gravity field observations contain integral information on hydrological mass changes. In this thesis on the one hand first investigations were carried out regarding the question to what extent hydrological signals in gravity data can provide constraints for hydrological process research on a local scale and if they may serve for evaluating local hydrological models. On the other hand local hydrological variations need to be eliminated from gravity data because they interfere with other geodynamic signals and with changes in continental water storage. Thus, a reduction of local hydrological influences in gravity data based on a local hydrological model was developed.

For the study of these issues, experimental research was carried out for the surroundings of the Geodynamic Observatory Moxa. Gravity changes due to soil moisture and water table changes, rain events as well as snow accumulation and melt have been observed at Moxa stationarily with a superconducting gravimeter. To investigate this influence, different hydrological experiments had been carried out around the superconducting gravimeter which led to a first rough modelling approach and to some knowledge about the different hydrological processes acting in the gravimeter surroundings (Kroner et al., 2007). However, a more accurate reduction is needed which has to incorporate the spatial hydrological dynamics in the catchment around the observatory.

The feasibility to detect spatial hydrological variations of a few 10 nm/s^2 using relative gravimeters was investigated. Because this study was successful, the impact of hydrological changes on gravity could be analysed spatially by distributed observations on a local network.

For this purpose, the local gravity network MoxaNet was established in the surroundings of Moxa observatory which are characterised by inhomogeneous subsoil and hilly topography. Spatially distributed measurements were carried out using L&R relative gravimeters in a seasonal rhythm as well as at special hydrological events like snow melt or dryness in 19 campaigns over a period of nearly three years. In this thesis, the network design, the instruments deployed, and the data evaluation process were discussed in detail. After extensive test measurements and improvements in the network design, the standard deviations of the measurement results were reduced to a level which enabled the significant detection of hydrological changes in an order of some 10 nm/s^2 .

Because always temporal changes in the gravity differences between two measuring points were analysed, an effect of regional or global hydrological variations was avoided. The local hydrological variations could be separated from regional or global changes. The results of the repeated gravity measurements were compared to soil moisture and water table observations to identify and localise hydrological processes and quantify their influence on gravity. The following conclusions can be drawn:

- Within a local network with point distances of several 10 m and a gravity range of $5 \cdot 10^{-5} \text{ m/s}^2$, it is basically possible to achieve standard deviations in the order of ± 10 to $\pm 15 \text{ nm/s}^2$ for one adjusted gravity difference of one campaign by repeated measurements using several selected and well-calibrated L&R relative instruments in parallel.

- Temporal changes, observed in the gravity differences, turned out to be associated with hydrological processes. Hydrological mass shifts between points in different hydrological areas of up to 170 nm/s^2 (140 nm/s^2 between two successive campaigns), caused by lateral heterogeneities and hilly topography, were proved significantly.
- Maximum variations were found in the differences between the observation points in the valley and at the steep slope east of the observatory, pointing to strong, gravimetrically active hydrological variations in the steep slope. It leads to the conclusion that a previously underestimated gravimetrically significant hydrological storage in the hill to the east of Moxa observatory was localised and quantified by the spatially distributed measurements.

Hydrologically induced gravity variations result from the temporal and spatial variable water content in the various compartments of the hydrological system. Thus, in the next step spatial and temporal density variations of the soil and rock were simulated numerically by changing the densities of the bodies in a gravimetric 3D model of the observatory surroundings. The input of the gravimetric model bases on Bouguer and free-air anomaly maps compiled from measurements on 460 gravity points in the modelling area in the observatory surroundings. The complex model incorporates local geology, topography, and hydrological domains and is well constrained by various geological and geophysical boundary conditions as results from seismic and geoelectrical measurements or information from digging and from boreholes. The achieved residuals of the gravimetric model are small, underlining, that the model is suited for the hydrological studies aimed for.

Spatially and temporally distributed hydrological input for the gravimetric model was obtained from the application of a process-oriented hydrological model of the catchment of the creek Silberleite. Estimates of water storage changes for the different hydrological relevant compartments were derived. By coupling the hydrological and gravimetric model, the gravity effect – caused by changing densities due to changing water storage – was computed as time series for a given position. By studying the modelled gravity effects for the different observation points and comparing them to the observed gravity from the repeated campaigns at the MoxaNet and the superconducting gravimeter, the following conclusions can be drawn:

- The combination of a local hydrological model with a gravimetric 3D model is a suitable new method for hydrological time-dependent studies. It was successfully applied for the surroundings of the superconducting gravimeter at the Geodynamic Observatory Moxa.
- Hydrologically caused gravity variations of some 10 nm/s^2 , modelled for the locations of the local gravity network MoxaNet, correspond to the results of the repeated and spatially distributed high-precision gravity observations. A local seasonal signal was clearly identified and quantified.
- Both observation and modelling precisely indicate that strong hydrological variations in the steep slope east of the observatory have a major impact on the gravity observations.

- About 30 % of the local hydrological gravity effect originate from an area within a radius of 90 m around the observatory, 39 % from the zone between 90 and 250 m from the observatory. Thus, 70 % of the modelled local hydrological effect originate from an area within a radius of 250 m around the observatory.
- An improved reduction of the local hydrological effect in the continuous gravity recordings with the superconducting gravimeter was derived for both short-term meteorological events and seasonal variations. The reduction has a high accuracy, with uncertainties of $\pm 1.5 \text{ nm/s}^2$ for rain events and $\pm 2.5 \text{ nm/s}^2$ for seasonal changes.
- Local seasonal fluctuations were reliably eliminated from the superconducting gravimeter data unmasking clear regional and global seasonal variations with a maximum/minimum amplitude of approximately 32 nm/s^2 . This seasonal signal is confirmed by global hydrological models and GRACE satellite observations (cf. Section 9).

Regarding the quality of the local hydrological model, additional conclusions can be drawn indicating also possible modifications on the model:

- From the comparison of the modelled and the observed gravity for the MoxaNet it can be derived that the hydrological modelling reproduces the hydrological dynamics in the catchment very well. The modelling results obtained for the location of the superconducting gravimeter make a reduction of the local hydrological effect in the gravimeter data possible, in particular the effect of rain events was crucially reduced. Additionally, a previously hidden global seasonal signal in the gravity data was unmasked by the reduction.
- As mentioned previously, hydrological variations in the steep slope to the east of the observatory have a major impact on the gravimeter signals. The hydrological situation in this slope is not well investigated so far. From additional hydrological investigations on this slope, a finer HRU partitioning in this gravimetrically crucial area may be derived to provide further improved modelling results.
- The hydrological influence of the sealed floor of the observatory building is not sufficiently reflected by the modelling so far. This might cause some of the deviations between observations and modelling results in the gravity differences between the points in the valley. In particular, uncertainties in short-period influences (hours to days) may be reduced by incorporating the sealed floor more precisely, though that may be a very challenging and difficult task.
- Variations due to common rain events and seasons are very well simulated by the hydrological model. At extreme hydrological events such as heavy or long lasting rain or snow melt, however, improvement is required. The gravity effect of snow melt and heavy rain events is reflected time-delayed by the local hydrological model compared to the observations with the superconducting gravimeter. This produces strong peaks

after such events in the respective local hydrology reduced gravity data. Because this effect is probably caused by the lateral routing in the hydrological model, the response time of the different storages need to be shortened by some hours for heavy rain events and days for snow melts.

- Partially, the modelled gravity effect over- or underestimates the observed gravity effect. This leads to the assumption that some details of hydrological processes influencing gravity are not sufficiently considered yet, e.g. groundwater flow or small-scale heterogeneities in the Silberleite valley. However, the maximum amplitude of these effects can be estimated to be smaller than $\pm 1.5 \text{ nm/s}^2$.

From these results the general conclusion can be drawn that an evaluation of hydrological modelling by gravity observations in combination with gravimetric 3D modelling on a local scale is possible to a certain extent. The accuracy of this evaluation strongly depends on the quality of the gravity data, the resolution of the local hydrological and gravimetric model, how close to reality the different hydrological contributors are included in the particular hydrological model, and how accurate the output of the hydrological model is converted to gravity values for comparison with the observed gravity data. For the local hydrological reduction an accuracy of $\pm 2.5 \text{ nm/s}^2$ was obtained for the minimum/maximum amplitude of the seasonal variations. A number of possible modifications on the modelling were derived which may further improve the hydrological model and the local hydrological reduction for the superconducting gravimeter.

9 Outlook

There are different ideas to continue the work started regarding several aspects of this thesis. The most important point concerns the unmasked seasonal variations in the data of the superconducting gravimeter.

9.1 Global interpretations

Because of the high-accuracy local hydrological reduction for the superconducting gravimeter data with uncertainties of only $\pm 2.5 \text{ nm/s}^2$ for seasonal variations, the gravity data become suitable to be interpreted with regard to changes in continental water storage as studied in data derived from the GRACE satellite mission and global hydrological models.

The superconducting gravimeter data are recorded each second. In contrast, GRACE gravity field solutions and data from global hydrological models are available as monthly values. To bridge this gap in temporal resolution, monthly arithmetic means were calculated from the continuous gravimeter data for the period between January 2004 and December 2006, shown in Figure 9.1. The gravity variations reduced for local hydrology with versions 3 and 4 of the local gravimetric 3D model (cf. Figure 7.5) are shown in Figure 9.1 a, the unreduced gravity is given in Figure 9.1 b. After removing the local hydrological effect, a clear seasonal variation becomes visible in the gravity data as discussed already in Section 7.2. This remaining part can be assumed to be mainly due to mass changes in regional and global terrestrial water storage.

A comparison of terrestrial gravity data monitored with the superconducting gravimeter at Moxa station, GRACE satellite-derived gravity field variations, and gravity changes based on the Water-GAP Global Hydrology Model WGHM (Döll et al., 2003) is given in Figure 9.2. The total non-local seasonal hydrological effect amounts to 30–50 nm/s^2 which is a well-resolvable signal in terrestrial gravity observations in mid-Europe on condition that – if needed – a local hydrological influence is appropriately removed first. In the gravity residuals without local hydrological reduction (cf. Figure 9.1), the seasonal signal is not reflected. Thus, only the reduction of the local hydrological influence reveals variations related to changes in continental water storage.

An agreement that is in principle good exists between the terrestrial data and the GRACE monthly gravity field solutions for a Gauss filtering with $\ell_{\text{fl}} = 10$ and $\ell_{\text{fl}} = 13$ respectively (cf. also Neumeyer et al., 2006, 2008). The GRACE solutions are low pass filtered by Gaussian averaging in the space domain, which corresponds to a damping of the spherical harmonic coefficients by a Gaussian bell shaped function (Jekeli, 1981). Damping functions are used in such a way that their values are 1/2 for spherical harmonic degrees =10 and 13 (Neumeyer et al., 2008).

The WGHM, applied to estimate gravity contributions caused by continental water storage changes, represents the most important continental water storage compartments (snow, soil moisture, groundwater, surface water in rivers, lakes and wetlands) at a spatial resolution of

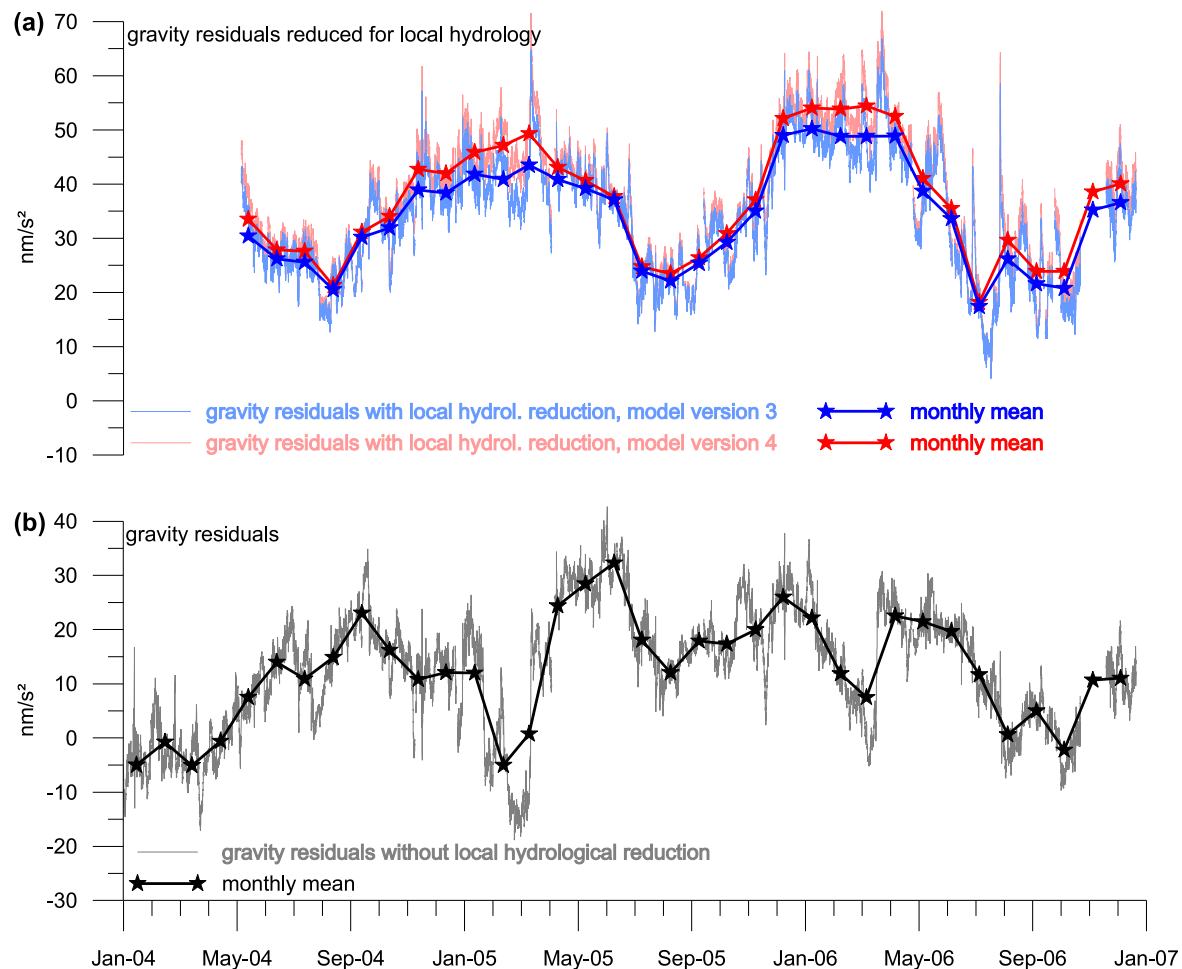


Figure 9.1: Gravity variations of the superconducting gravimeter at Moxa between January 2004 and December 2006 in hourly values (continuous line) as well as monthly arithmetic means (linear connected stars) for comparison with GRACE and global hydrological models (Figure 9.2); (a) gravity variations reduced for local hydrology with model versions 3 and 4 (cf. Figure 7.5), (b) unreduced gravity variations.

0.5° with global coverage in monthly time steps (Güntner et al., 2007a,b). Gravity changes from the WGHM and observed variations generally coincide. Apart from the correspondence in principle between the various time series, deviations with respect to amplitudes and phases occur between terrestrial and satellite data as well as observed gravity variations and such derived from the global hydrological model. With regard to these deviations further research may commence with the goal to derive constraints from terrestrial and satellite gravity observations for an improvement of regional and global hydrological models.

As shown in Section 7.2, after applying a local hydrological reduction a seasonal variation emerges in the residuals of the superconducting gravimeter at Moxa station which was previously masked by the local hydrology. This variation is related to changes in continental water storage. At other stations equipped with a superconducting gravimeter like Bad Homburg or

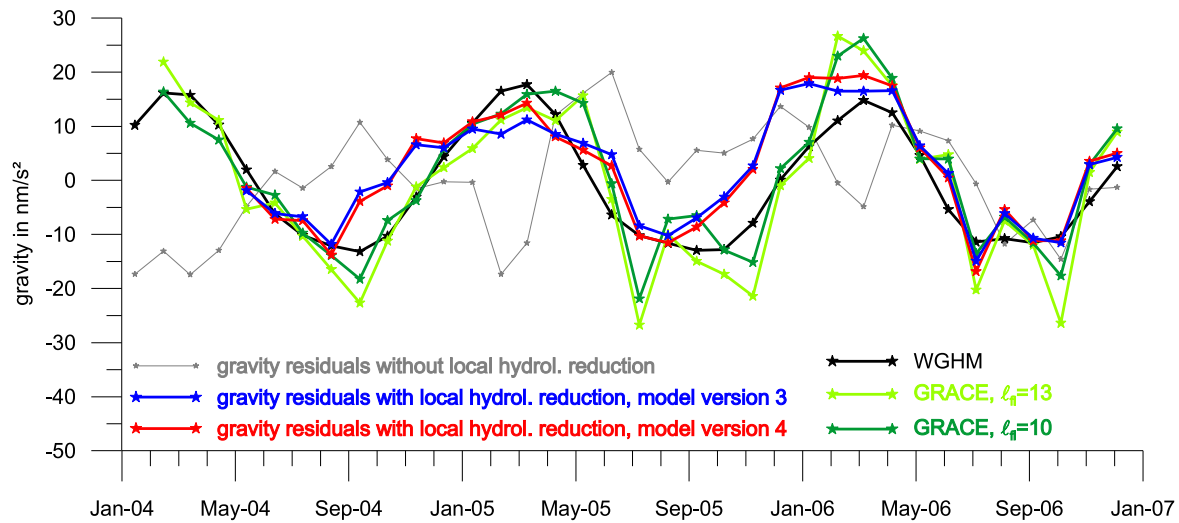


Figure 9.2: Comparison of gravity residuals from the superconducting gravimeter observation, reduced and unreduced for local hydrology, with monthly GRACE solutions using different filtering and gravity variations derived from changes in continental water storage computed with the WGHM model for the station Moxa; GRACE and WGHM data after Neumeyer et al. (2008).

Medicina the local hydrological signal does not seem to differ significantly from the regional changes. In contrast to Moxa station, at these observatories there is no rock and water mass above the level of the gravimeter. Because these stations are surface stations all hydrological variations take place below the instrument. At the subsurface station Strasbourg, the local hydrological signal also masks regional changes (Longuevergne, 2008). The situation there is partially comparable to the situation at Moxa station.

In general, both terrestrial and satellite data contain valuable information on mass transfer, especially on hydrological mass phenomena. Thus, they can be deployed for the assessment and evaluation of regional and global hydrological models.

9.2 Other perspectives

Besides the most important outlook from this thesis already given some other perspectives are worth to be studied in future.

- The vertical gravity gradient at the location of the superconducting gravimeter at Moxa was determined with high accuracy from measurements with L&R relative gravimeters to $-0.2296 \pm 0.0007 \cdot 10^{-5} \text{ s}^{-2}$. It would be an interesting task to investigate if measurements with L&R instruments offer a sufficiently high accuracy to determine hydrologically induced changes of the vertical gravity gradient at the locations of the MoxaNet.

During the first irrigation experiment (cf. Paragraph 3.2.3.1), in which more than

17.6 m³ water were irrigated on the roof area over a period of half an hour, a gravity decrease of 11.5 nm/s² was measured by the lower sensor of the gravimeter, and 12.0 nm/s² by the upper sensor (Kroner, 2002). Because the sensors are in a vertical distance of 0.2 m, a change in the vertical gravity gradient of $0.00025 \cdot 10^{-5} \text{ s}^{-2}$ follows. This order of magnitude was confirmed by test calculations with the gravimetric model. The change lies within the standard deviations obtained at the gradient measurements with L&R gravimeters. Thus, hydrological variations can probably not be significantly detected in the gravity gradient using L&R gravimeters or instruments with similar accuracy. Even if a maximum effect, e.g. the gravity effect of a snow melt, is considered, the accuracy of portable gravimeters is too low to detect such events as changes in the gravity gradient.

- The methods developed and the results achieved for Moxa observatory can be transferred to other gravity stations and other regions. Depending on the extension of the local area in other regions, spatial gravity information as constraint for local and regional hydrological modelling can be gained by GRACE or GOCE satellite observations combined with terrestrial gravity data from superconducting and absolute gravimeters as well as – if possible and needed – repeated and spatial observations with transportable instruments.
- Additional investigations to separate the local hydrological influence from areas above and below the level of the superconducting gravimeter at Moxa observatory could be carried out to gain further information on the hydrological processes and to derive further constraints for the local hydrological modelling.
- Local hydrological influences on gravity records might be avoided, if the gravimeter station is established far away from such influence, e.g. in the desert. However global hydrological changes are always measured. Regarding Moxa observatory, it would be interesting to investigate, whether the hydrological influence on the gravimeter signal will be significantly lower, if the gravimeter is operated in the hill at the end of the gallery.
- From the gravimetric modelling a high resolution model of the subsoil was derived. The geometry of the subsoil can be transferred to a 3D finite element model and hydrological effects in strain and tilt observations could be modelled, quantified and compared to the observations at Moxa observatory. This approach may lead to reduction methods for hydrological changes in tilt and strain observations and could provide further constraints for local hydrological modelling.

10 References

- Abe, M., Kroner, C., Neumeyer, J., & Chen, X. D., 2008: *Assessment of atmospheric reductions for terrestrial gravity observations*, Geophys. J. Int., submitted.
- Abe, M., Takemoto, S., Fukuda, Y., Higashi, T., Imanishi, Y., Iwano, S., Ogasawara, S., Kobayashi, Y., Takiguchi, H., Dwipa, S., & Kusuma, D. S., 2006: *Hydrological effects on the superconducting gravimeter observation in Bandung*, J. Geodyn. 41 (1–3): 288–295, doi:10.1016/j.jog.2005.08.030.
- Amalvict, A., Hinderer, J., Mäkinen, J., Rosat, S., & Rogister, Y., 2004: *Long-term and seasonal gravity changes at the Strasbourg station and their relation to crustal deformation and hydrology*, J. Geodyn. 38 (3–5): 343–353, doi:10.1016/j.jog.2004.07.010.
- Andersen, O. B., Bauer-Gottwein, P., Smith, R., Berry, P., & Krogh, P. E., 2008: *Terrestrial water storage monitoring from time-lapse GRACE gravimetry and satellite altimetry in the Okavango Delta (Botswana)*, Poster presentation at GGEO2008, 23–27 June 2008, Chania.
- Aoyama, Y. & Naito, I., 2000: *Wind contributions to the earth's angular momentum budget in seasonal variations*, J. Geophys. Res. 105 (D10): 12 417–12 431, doi:10.1029/2000JD900101.
- Atzbacher, K. & Gerstenecker, C., 1993: *Secular gravity variations: recent crustal movements or scale factor changes*, J. Geodyn. 18 (1–4): 107–121, doi:10.1016/0264-3707(93)90033-3.
- Baker, T. F., 1978: *What can earth tide measurements tell us about ocean tides or earth structure?*, in *Proc. 9th GEOP Conf. Dept. of Geod. Science, Ohio State Univ.*, vol. 280.
- Banka, D., 1993: *Die Theorie zur direkten Berechnung von Erdeigenschwingungen*, Diploma thesis, Institute for Geophysics, TU Clausthal, unpublished.
- Bartels, J., 1957: *Gezeitenkräfte*, in *Handbuch der Physik: Geophysik II*, vol. 48, pp. 734–774, Flügge, Berlin–Göttingen–Heidelberg.
- Becker, A. & Behrendt, H., 1998: *Auswirkung der Landnutzung auf den Wasser- und Stoffhaushalt der Elbe*, Interim report, Potsdam Institute for Climate Impact Research, Potsdam.
- Bonatz, M., 1967: *Der Gravitationseinfluß der Bodenfeuchte*, Zeitschrift für Vermessungswesen 92: 135–139.
- Bower, D. & Courtier, N., 1998: *Precipitation effects on gravity measurements at the Canadian absolute gravity site*, Phys. Earth Planet. Int. 106 (3–4): 353–369, doi:10.1016/S0031-9201(97)00101-5.

- Boy, J.-P., Gegout, P., & Hinderer, J., 2002: *Reduction of surface gravity data from global atmospheric pressure loading*, Geophys. J. Int. 149 (2): 534–545, doi:10.1046/j.1365-246X.2002.01667.x.
- Boy, J.-P. & Hinderer, J., 2006: *Study of the seasonal gravity signal in superconducting gravimeter data*, J. Geodyn. 41 (1–3): 227–233, doi:10.1016/j.jog.2005.08.035.
- Bullen, K. E., 1947: *An introduction to the theory of seismology*, Cambridge University Press.
- Cartwright, D. E. & Edden, A. C., 1973: *Corrected tables of tidal harmonics*, Geophys. J. R. Astr. Soc. 33 (3): 253–264.
- Chow, V. T., 1964: *Handbook of applied hydrology: a compendium of water-resources technology*, McGraw-Hill, New York.
- Courtier, N., Ducarme, B., Goodkind, J., Hinderer, J., Imanishi, Y., Seama, N., Sun, H.-P., Merriam, J. B., Bengert, B., & Smylie, D. E., 2000: *Global superconducting gravimeter observations and the search for the translational modes of the inner core*, Phys. Earth Planet. Int. 117: 3–20, doi:10.1016/S0031-9201(99)00083-7.
- Crossley, D. J., Hinderer, J., Casula, G., Francis, O., Hsu, H.-T., Imanishi, Y., Jentzsch, G., Kääriäinen, J., Merriam, J., Meurers, B., Richter, B., Shibuya, K., Sato, T., & van Dam, T., 1999: *Network of superconducting gravimeters benefits a number of disciplines*, EOS Transactions 80 (11): 121–126, doi:10.1029/99EO00079.
- Crossley, D. J., Jensen, O. G., & Hinderer, J., 1995: *Effective barometric admittance and gravity residuals*, Phys. Earth Planet. Int. 90 (3–4): 221–241, doi:10.1016/0031-9201(95)05086-Q.
- Crossley, D. J. & Rochester, M. G., 1992: *The subseismic approximation in core dynamics*, Geophys. J. Int. 108 (2): 502–506, doi:10.1111/j.1365-246X.1992.tb04631.x.
- Crossley, D. J., Xu, S., & van Dam, T., 1998: *Comprehensive Analysis of 2 years of SG Data from Table Mountain, Colorado*, in *Proc. 13th Int. Symp. Earth Tides* (B. Ducarme & P. Pâquet, eds), pp. 659–668, Observatoire Royal de Belgique, Brussels, Schweizerbart'sche Verlagsbuchhandlung.
- De Vries, D. & Wahr, J. M., 1991: *The effects of the solid inner core and nonhydrostatic structure on the earth's forced nutations and earth tides*, J. Geophys. Res. 96 (B5): 8 275–8 293, doi:10.1029/90JB01958.
- Dehant, V., 1987: *Tidal parameters for an inelastic earth*, Phys. Earth Planet. Int. 49: 97–116, doi:10.1016/0031-9201(87)90134-8.
- Dehant, V., Hinderer, J., Legros, H., & Lefftz, M., 1993: *Analytical approach to the computations of the earth, the outer core and the inner core rotational motions*, Phys. Earth Planet. Int. 76 (3–4): 259–282, doi:10.1016/0031-9201(93)90018-5.

- Delcourt-Honorez, M., 1995: *Hydrological effects on the local gravity*, Cahiers du Centre Européen de Géodynamique et de Séismologie 11: 61–168.
- Dittfeld, H.-J., 2000: *Final results of the SG–registration in Potsdam*, Bulletin d'Information des Marées Terrestres 132: 10 355–10 368.
- Döll, P., Kaspar, F., & Lehner, B., 2003: *A global hydrological model for deriving water availability indicators: model tuning and validation*, J. Hydrol. 270: 105–134, doi:10.1016/S0022-1694(02)00283-4.
- Drewes, H., Benitez, R., & Bravo, D., 1983: *Time series analysis of gravity variations*, in *Proc. of the IAG Symposia, XVIII IUGG Gen. Ass., Hamburg, 1983*, vol. 1, pp. 180–194, Dep. of Geod. Science and Surveying, The Ohio State Univ., Columbus, Ohio.
- Ekman, M., Mäkinen, J., Midtsundstad, A., & Remmer, O., 1987: *Gravity change and land uplift in Fennoscandia 1966–1984*, J. Geodesy 61 (1): 60–64, doi:10.1007/BF02520415.
- Elstner, C., 1987: *On common tendencies in repeated absolute and relative gravity measurements in the central part of the GDR*, Gerlands Beiträge zur Geophysik 96 (3–4): 197–205.
- Elstner, C. & Kautzleben, H., 1982: *Results of annual gravity measurements along a W–E profile inside the GDR for the period 1970–1980*, Proc. Gen. Meeting of the IAG, Tokyo pp. 341–348.
- Ergintav, S., Doğan, U., Gerstenecker, C., Çakmak, R., Belgen, A., Demirel, H., Aydin, C., & Reilinger, R., 2007: *A snapshot (2003–2005) of the 3D postseismic deformation for the 1999, $M_w = 7.4$ İzmit earthquake in the Marmara Region, Turkey, by first results of joint gravity and GPS monitoring*, J. Geodyn. 44: 1–18, doi:10.1016/j.jog.2006.12.005.
- Farrell, W. E., 1972: *Deformation of the Earth by Surface Loads*, Rev. Geophys. 10 (3): 761–797.
- Florsch, N. & Hinderer, J., 2000: *Bayesian estimation of the free core nutation parameters from the analysis of precise tidal gravity data*, Phys. Earth Planet. Int. 117: 21–35, doi:10.1016/S0031-9201(99)00084-9.
- Fong Chao, B., 1993: *Excitation of the earth's polar motion by atmospheric angular momentum variations 1980–1990*, Geophys. Res. Lett. 20 (3): 253–256, doi:10.1029/93GL00130.
- Forbriger, T., 2007: *Reducing magnetic field induced noise in broad-band seismic recordings*, Geophys. J. Int. 169: 240–258, doi:10.1111/j.1365-246X.2006.03295.x.
- Franke, W., 1984: *Structure of Variscan nappes of the Münchberg Gneismasse area as derived from facies, deformation and degree of metamorphism of the surrounding region*, in *Geotectonic Research*, vol. 68, E. Schweizerbart'sche Verlagsbuchhandlung, Stuttgart.

- Furuya, M. & Hamano, Y., 1998: *Effect of the Pacific Ocean on the Earth's seasonal wobble inferred from National Center for Environmental Prediction ocean analysis data*, J. Geophys. Res. 103 (B5): 10 131–10 140, doi:10.1029/97JB03531.
- Furuya, M., Hamano, Y., & Naito, I., 1996: *Importance of wind for the excitation of Chandler wobble as inferred from wobble domain analysis*, J. Physics Earth 45: 177–188.
- Gabriel, G., Jahr, T., Jentzsch, G., & Melzer, J., 1997: *Deep structure and evolution of the Harz Mountains: results of three-dimensional gravity and finite-element modeling*, Tectonophysics 270 (3–4): 279–299, doi:10.1016/S0040-1951(96)00176-X.
- Google Earth, 2008: <http://earth.google.de/>, last access 08/06/14.
- Götze, H.-J., 1976: *Ein numerisches Verfahren zur Berechnung der gravimetrischen Feldgrößen für dreidimensionale Modellkörper*, PhD thesis, Institute of Geophysics, TU Clausthal.
- Götze, H.-J., 1984: *Über den Einsatz interaktiver Computergraphik im Rahmen 3-dimensionaler Interpretationstechniken in der Gravimetrie und der Magnetik*, Habilitation thesis, Institute of Geophysics, TU Clausthal.
- Götze, H.-J. & Lahmeyer, B., 1988: *Application of three-dimensional interactive modelling in gravity and magnetics*, Geophysics 53 (8): 1096–1108, doi:10.1190/1.1442546.
- Großmann, W., 1969: *Grundzüge der Ausgleichsrechnung*, Springer, Berlin, Heidelberg, New York, 3rd edn.
- Güntner, A., Schmidt, R., & Döll, P., 2007a: *Supporting large-scale hydrogeological monitoring and modelling by time-variable gravity data*, Hydrogeology Journal 15 (1): 167–170, doi:10.1007/s10040-006-0089-1.
- Güntner, A., Stuck, J., Werth, S., Döll, P., Verzano, K., & Merz, B., 2007b: *A global analysis of temporal and spatial variations in continental water storage*, Water Resour. Res. 43 (5): W05 416, doi:10.1029/2006WR005247.
- Harnisch, G. & Harnisch, M., 2006: *Hydrological influences in long gravimetric data series*, J. Geodyn. 41 (1–3): 276–287, doi:10.1016/j.jog.2005.08.018.
- Harnisch, M. & Harnisch, G., 1999: *Hydrological influences in the registrations of superconducting gravimeters*, Bulletin d'Information des Marées Terrestres 131: 10 161–10 170.
- Harnisch, M. & Harnisch, G., 2001: *Study of long-term gravity variations, based on data of the GGP cooperation*, J. Geod. Soc. Japan 47 (1): 322–327.
- Harnisch, M., Harnisch, G., Jurczyk, H., & Wilmes, H., 2000: *889 days of registration with the superconducting gravimeter SG 103 at Wettzell (Germany)*, Bulletin d'Information des Marées Terrestres 132: 10 341–10 353.

- Hartmann, T. & Wenzel, H.-G., 1995: *The HW95 Tidal Potential Catalogue*, Geophys. Res. Lett. 22 (24): 3 553–3 556, doi:10.1029/95GL03324.
- Hasan, S., Troch, P., Bogaart, P., & Kroner, C., 2008: *Evaluating catchment-scale hydrological modeling by means of terrestrial gravity observations*, Water Resour. Res. W08416, doi:10.1029/2007WR006321.
- Hasan, S., Troch, P., Boll, J., & Kroner, C., 2006: *Modeling of the hydrological effect on local gravity at Moxa, Germany*, J. Hydrometeor. 7 (3): 346–354, doi:10.1175/JHM488.1.
- Haurwitz, B. & Cowley, A. D., 1973: *The diurnal and semi-diurnal oscillations, global distribution and annual variation*, Pageoph. 102: 193–221.
- Hempel, G., 2003: *Variszische Tektonik*, in *Geologie von Thüringen* (G. Seidel, ed.), E. Schweizerbart'sche Verlagsbuchhandlung, Stuttgart, 2nd edn.
- Hinderer, J., Crossley, D. J., & Jensen, O., 1995: *A search for the Slichter triplet in superconducting gravimeter data*, Phys. Earth Planet. Int. 90 (3–4): 183–195, doi:10.1016/0031-9201(95)05083-N.
- Hinderer, J., Legros, H., & Amalvict, M., 1982: *A search for Chandler and nearly diurnal free wobble using Liouville equations*, Geophys. J. R. Astr. Soc. 71 (2): 303–332, doi:10.1111/j.1365-246X.1982.tb05992.x.
- Hinderer, J., Legros, H., & Crossley, D. J., 1991: *Global earth dynamics and induced gravity changes*, J. Geophys. Res. 96 (B12): 20 257–20 265, doi:10.1029/91JB00423.
- Hofmann, Y., Jahr, T., & Jentzsch, G., 2003: *Three-dimensional gravimetric modelling to detect the deep structure of the region Vogtland/NW-Bohemia*, J. Geodyn. 35: 209–220, doi:10.1016/S0264-3707(02)00063-7.
- Hokkanen, T., Korhonen, K., Virtanen, H., & Laine, E. L., 2007a: *Effects of the fracture water of bedrock on superconducting gravimeter data*, Near Surface Geophysics 5 (2): 133–140.
- Hokkanen, T., Virtanen, H., & Pirttivaara, M., 2007b: *On hydrogeological noise in superconducting gravimeter data*, Near Surface Geophysics 5 (2): 125–132.
- Imanishi, Y., 2000: *Present status of SG T011 at Matsushiro, Japan*, Cahiers du Centre Européen de Géodynamique et de Séismologie 17: 97–102.
- Imanishi, Y., Kokubo, K., & Tatehata, H., 2006: *Effect of underground water on gravity observation at Matsushiro, Japan*, J. Geodyn. 41: 221–226, doi:10.1016/j.jog.2005.08.031.
- Imanishi, Y., Sato, T., Higashi, T., Sun, W., & Okubo, S., 2004: *A Network of Superconducting Gravimeters Detects Submicrogal Coseismic Gravity Changes*, Science 306: 476–478, doi:10.1126/science.1101875.

- Jahr, T., Jentzsch, G., & Kroner, C., 2001: *The Geodynamic Observatory Moxa / Germany: Instrumentation and purposes*, J. Geod. Soc. Japan 47 (1): 34–39.
- Jahr, T., Jentzsch, G., Kroner, C., Malischewsky, P., Naujoks, M., & Ziegert, A., 2008: *Geophysikalische Geländeübung (Grundstufe) in Moxa 2000–2008*, mapping report, unpublished, Institute of Geosciences, Friedrich-Schiller-University Jena.
- Jekeli, C., 1981: *Alternative methods to smooth the Earth's gravity field*, in *Reports of the Department of Geodetic Science and Surveying*, vol. 327, Ohio State University, Columbus.
- Jentzsch, G., 1986: *Auflastzeiten in Fennoscandien*, in *Berliner Geowissenschaftliche Abhandlungen*, vol. 13, Inst. of Geophys. Sciences, FU Berlin.
- Jentzsch, G., 1997: *Earth tides and ocean tidal loading*, in *Tidal Phenomena* (H. Wilhelm, W. Zürn & H.-G. Wenzel, eds), 66, pp. 145–171, Lecture Notes in Earth Sciences.
- Jentzsch, G., 2004: *Jena, eine Wiege der Seismologie in Deutschland*, Beitrag im Jahrbuch für Technikgeschichte. Glaux Verlag, Jena.
- Jentzsch, G., Knudsen, P., & Ramatschi, M., 2000: *Ocean tidal loading affecting precise geodetic observations on Greenland: error accounts of surface deformation by tidal gravity measurements*, Phys. Chem. Earth 25 (4): 401–408, doi:10.1016/S1464-1895(00)00063-6.
- Jentzsch, G. & Koß, S., 1997: *Interpretation of long-period tilt records at Blå Sjø, southern Norway, with respect to variations in the lake level*, Phys. Chem. Earth 22 (1–2): 25–31, doi:10.1016/S0079-1946(97)00073-6.
- Jentzsch, G., Weise, A., Rey, C., & Gerstenecker, C., 2004: *Gravity Changes and Internal Processes: Some Results Obtained from Observations at Three Volcanoes*, Pure Appl. Geophys. 161 (7): 1415–1431, doi:10.1007/s00024-004-2512-7.
- Kanngieser, E., Kummer, K., Torge, W., & Wenzel, H.-G., 1983: *Das Gravimeter-Eichsystem Hannover*, Wissenschaftliche Arbeiten der Fachrichtung Vermessungswesen der Universität Hannover, 120.
- Kasch, N., 2006: *Geologische Neukartierung der Umgebung des Geodynamischen Observatoriums Moxa*, Diploma thesis, Institute of Geosciences, Friedrich-Schiller-University Jena, unpublished.
- Kiviniemi, A., 1974: *High precision measurements for studying the secular variation in gravity in Finland*, Publication of the Finnish Geodetic Institute, 78.
- Krause, P., 2001: *Das hydrologische Modellsystem J2000: Beschreibung und Anwendung in großen Flußeinzugsgebieten*, in *Schriften des Forschungszentrums Jülich: Reihe Umwelt/Environment*, vol. 29, Forschungszentrum Jülich.

- Krause, P., Fink, M., Kroner, C., Sauter, M., & Scholten, T., 2005: *Hydrological processes in a small headwater catchment and their impact on gravimetric measurements*, Proc. Headwater 2005, Bergen, CD-ROM.
- Krause, P., Naujoks, M., Fink, M., & Kroner, C., 2008: *The impact of soil moisture changes on gravity residuals obtained with a superconducting gravimeter*, J. Hydrology, submitted.
- Kroner, C., 1997: *Reduktion von Luftdruckeffekten in zeitabhängigen Schwerebeobachtungen*, PhD thesis, Institute of Geophysics, TU Clausthal.
- Kroner, C., 2001: *Hydrological effects on gravity data of the Geodynamic Observatory Moxa*, J. Geod. Soc. Japan 47 (1): 353–358.
- Kroner, C., 2002: *Zeitliche Variationen des Erdschwerefeldes und ihre Beobachtung mit einem supraleitenden Gravimeter im Geodynamischen Observatorium Moxa*, Jenaer Geowissenschaftliche Schriften, 2, Habilitation thesis.
- Kroner, C., 2006: *Hydrological signals in the SG records at Moxa — a follow up*, Bulletin d'Information des Marées Terrestres 142: 11 353–11 358.
- Kroner, C. & Jahr, T., 2006: *Hydrological experiments around the superconducting gravimeter at Moxa Observatory*, J. Geodyn. 41 (1–3): 268–275, doi:10.1016/j.jog.2005.08.012.
- Kroner, C., Jahr, T., & Jentzsch, G., 2004: *Results of 44 months of observations with a superconducting gravimeter at Moxa/Germany*, J. Geodyn. 38 (3–5): 263–280, doi:10.1016/j.jog.2004.07.012.
- Kroner, C., Jahr, T., Naujoks, M., & Weise, A., 2007: *Hydrological signals in gravity – foe or friend?*, in *Dynamic Planet – Monitoring and Understanding a Dynamic Planet with Geodetic and Oceanographic Tools* (P. Tregoning & C. Rizos, eds), vol. 130, pp. 504–510, IAG Symposia Series. Springer, doi:10.1007/978-3-540-49350-1_73.
- Kroner, C. & Jentzsch, G., 1999: *Comparison of different barometric pressure reductions for gravity data and resulting consequences*, Phys. Earth Planet. Int. 115: 205–208.
- Lambert, A. & Beaumont, C., 1977: *Nano Variations in Gravity Due to Seasonal Groundwater Movements; Implications for the Gravitational Detection of Tectonic Movements*, J. Geophys. Res. 82 (2): 297–306, doi:10.1029/JB082i002p00297.
- Liard, J. & Gagnon, C., 2002: *The new A-10 absolute gravimeter at the 2001 International Comparison of Absolute Gravimeters*, Metrologia 39 (5): 477–483, doi:10.1088/0026-1394/39/5/8.
- Liebe, K. T. & Zimmermann, E., 1888: *Geologische Spezialkarte von Preußen und den Thüringischen Staaten, Blatt Ziegenrück mit Erläuterungen*, Königlich Preußische Landesanstalt, Berlin.

- Linnemann, U., 2004: *Das Saxothuringikum. Abriss der präkambrischen und paläozoischen Geologie von Sachsen und Thüringen*, in *Geologica Saxonica* (U. Linnemann, ed.), vol. 48/49, Staatliche Naturhistorische Sammlungen Dresden, Museum für Mineralogie und Geologie, 2nd edn.
- Linnemann, U., Lützner, H., Heuse, T., & Kroner, U., 2002: *Cadomiden und Varisziden des Thüringischen Schiefergebirges (Neoproterozoikum bis Unterkarbon)*, Jahresberichte und Mitteilungen der Oberrheinischen Geologischen Vereins, Stuttgart 84: 191–223.
- Longuevergne, L., 2008: *Contribution to Hydrogeodesy*, PhD thesis, University Pierre et Marie Curie, Paris, France.
- Mäkinen, J. & Tattari, S., 1988: *Soil moisture and groundwater: Two sources of gravity variations*, Bulletin d'Information, Bureau Gravimetric International 63: 103–110.
- Mäkinen, J. & Tattari, S., 1991: *The influence of variation in subsurface water storage on observed gravity*, in *Proc. 11th Int. Symp. Earth Tides, 1989*, pp. 457–471, Schweizerbart'sche Verlagsbuchhandlung, Stuttgart.
- Mathews, P. M., Buffett, B. A., Herring, T. A., & Shapiro, I. I., 1991a: *Forced nutations of the earth: influence of inner core dynamics 1. Theory*, J. Geophys. Res. 96 (B5): 8 219–8 242, doi:10.1029/90JB01955.
- Mathews, P. M., Buffett, B. A., Herring, T. A., & Shapiro, I. I., 1991b: *Forced nutations of the earth: influence of inner core dynamics 2. Numerical results and comparison*, J. Geophys. Res. 96 (B5): 8 243–8 257, doi:10.1029/90JB01956.
- Melchior, P., Ducarme, B., van Ruymbeke, M., & Poitevin, C., 1985a: *Trans World Tidal Gravity Profiles*, Bulletin d'Information des Marées Terrestres 1: 1–102.
- Melchior, P., Poitevin, C., Ducarme, B., van Ruymbeke, M., Gemaël, C., & Ratton, E., 1985b: *Tidal gravity measurements in Brazil*, in *Proc. 10th Int. Symp. Earth Tides, Madrid* (R. Vieira, ed.), pp. 177–188, Consejo Superior de Investigaciones Científicas.
- Merriam, J. B., 1992: *Atmospheric pressure and gravity*, Geophys. J. Int. 109 (3): 488–500, doi:10.1111/j.1365-246X.1992.tb00112.x.
- Meurers, B., 2006: *Long and short term hydrological effects on gravity in Vienna*, Bulletin d'Information des Marées Terrestres 142: 11 343–11 352.
- Meurers, B., Van Camp, M., & Petermans, T., 2007: *Correcting superconducting gravity time-series using rainfall modelling at the Vienna and Membach station and application to Earth tide analysis*, J. Geodesy 81 (11): 703–712, doi:10.1007/s00190-007-0137-1.
- Monteith, J. L., 1975: *Vegetation and atmosphere*, vol. 1 principles, Academic Press, London.

- Müller, J., Timmen, L., Gitlein, O., & Denker, H., 2005: *Gravity changes in the Fennoscandian land uplift area to be observed by GRACE and absolute gravimetry*, in *Gravity, Geoid and Space Missions* (C. Jekeli & L. B. A. Fernandes, eds), vol. 129, pp. 309–309, IAG Symposia Series. Springer.
- Nagy, D., 1966: *The gravitational attraction of a right rectangular prism*, *Geophysics* 31 (2): 362–371, doi:10.1190/1.1439779.
- Nash, J. E. & Sutcliffe, J. V., 1970: *River flow forecasting through conceptual models part I — A discussion of principles*, *J. Hydrology* 10 (3): 282–290, doi:10.1016/0022-1694(70)90255-6.
- Naujoks, M., Kasch, N., Jahr, T., & Kley, J., 2008a: *Combined geological and geophysical investigations regarding the impact of local geological features on geophysical monitoring at the Geodynamic Observatory Moxa, Germany*, *International Journal of Earth Sciences*, in preparation.
- Naujoks, M., Kroner, C., Jahr, T., & Weise, A., 2006: *From a disturbing influence to a desired signal: Hydrological effects in gravity observations*, *Bulletin d'Information des Marées Terrestres* 142: 11 359–11 360, extended abstract.
- Naujoks, M., Kroner, C., Weise, A., Jahr, T., Krause, P., & Eisner, S., 2008b: *Evaluating small-scale hydrological modelling by time-dependent gravity observations and a gravimetric 3D model*, *Geophys. J. Int.*, in preparation.
- Naujoks, M., Kroner, C., Weise, A., Jahr, T., Krause, P., & Eisner, S., 2008c: *Schwerefeldbeobachtungen und Hydrologie*, DGG Kolloquium, DGG Sonderband.
- Naujoks, M., Weise, A., Kroner, C., & Jahr, T., 2008d: *Detection of small hydrological variations in gravity by repeated observations with relative gravimeters*, *J. Geodesy*, 82: 543–553, doi: 10.1007/s00190-007-0202-9.
- Nawa, K., Satake, K., Suda, N., Doi, K., Shibuya, K., & Sato, T., 2007: *Sea level and gravity variations after the 2004 Sumatra Earthquake observed at Syowa Station, Antarctica*, in *Dynamic Planet – Monitoring and Understanding a Dynamic Planet with Geodetic and Oceanographic Tools* (P. Tregoning & C. Rizos, eds), vol. 130, pp. 536–540, IAG Symposia series. Springer, doi:10.1007/978-3-540-49350-1_78.
- Nawa, K., Suda, N., Fukao, Y., Sato, T., Tamura, Y., Shibuya, K., McQueen, H., Virtanen, J., & Käätäinen, J., 2000: *Incessant excitation of the earth's free oscillations: global comparison of superconducting gravimeter records*, *Phys. Earth Planet. Int.* 120 (4): 289–297, doi:10.1016/S0031-9201(00)00158-8.
- Neumeyer, J., Barthelmes, F., Dierks, O., Flechtner, F., Harnisch, M., Harnisch, G., Hinderer, J., Imanishi, Y., Kroner, C., Meurers, B., Petrovic, S., Reigber, C., Schmidt,

- R., Schwintzer, P., Sun, H.-P., & Virtanen, H., 2006: *Combination of temporal gravity variations resulting from superconducting gravimeter (SG) recordings, GRACE satellite observations and global hydrology models*, *J. Geodesy* 79 (10–11): 573–585, doi:10.1007/s00190-005-0014-8.
- Neumeyer, J., Barthelmes, F., Kroner, C., Petrovic, S., Schmidt, R., Virtanen, H., & Wilmes, H., 2008: *Analysis of gravity field variations derived from Superconducting Gravimeter recordings, GRACE satellite and hydrological models at selected European sites*, *Earth, Planets and Space* 60 (5).
- Niessen, S. & Wesselius, C., 2006: *Groundwater flow and storage distribution in vicinity of the Geodynamic Observatory Moxa, Germany*, Diploma thesis, Department of Environmental Sciences, Wageningen University, unpublished.
- Pálinkáš, V., Kašpar, P., & Lederer, M., 2003: *Effect of the magnetic field on LCR gravimeters*, in *Proceedings of the Workshop: IMG-2002 Instrumentation and Metrology in Gravimetry* (O. Francis & T. van Dam, eds), pp. 89–93, ECGS and BIPM, Münsbach, Grand-Duchy of Luxembourg.
- Peter, G., Klopping, F., & Berstis, K., 1995: *Observing and modeling gravity changes caused by soil moisture and groundwater table variations with superconducting gravimeters in Richmond, Florida, U.S.A.*, *Cahiers du Centre Européen de Géodynamique et de Séismologie* 11: 147–159.
- Prinz, H., 1997: *Abriß der Ingenieurgeologie – mit Grundlagen der Boden- und Felsmechanik, des Erd-, Grund- und Tunnelbaus sowie der Abfalldeponien*, Ferdinand Enke Verlag, Stuttgart, 3rd edn.
- Sato, T., Boy, J.-P., Tamura, Y., Matsumoto, K., Asari, K., Plag, H.-P., & Francis, O., 2006: *Gravity tide and seasonal gravity variation at Ny-Ålesund, Svalbard in Arctic*, *J. Geodyn.* 41 (1–3): 234–241, doi:10.1016/j.jog.2005.08.016.
- Schmidt, S., 1996: *3D Modelling of Geoid and Gravity using GIS-Functions*, Österreichische Beiträge zur Meteorologie und Geophysik, Wien 14: 137–144.
- Schmidt, S., 2000: *IGMAS — Interactive Gravity and Magnetic Application System*, Online Manual, <http://www.gravity.uni-kiel.de/igmas/> Last access 08/06/14.
- Scholten, T., Behrens, T., Dahlke, H., Förster, H., Gülland, K., Kipka, H., Lippelt, J., Poppe, U., & Schmidt, K., 2004: *Bodenkundliche Karte 1:10 000 für das Einzugsgebiet der Silberleite am Geodynamischen Observatorium Moxa*, soilmap, unpublished.
- Schroeder, E., 1966: *Beiträge zur Schiefergebirgstektonik in Ostthüringen*, in *Abhandlungen der Deutschen Akademie der Wissenschaften, Klasse für Chemie, Geologie und Biologie*, 1965, 4; *Abhandlungen zur Geotektonik*, 23, Akademischer Verlag.

- Schulze, C., 1998: *Kleinräumige geophysikalische Untersuchungen im Bereich des seismologischen Observatoriums Moxa*, Diploma thesis, Institute of Geophysics, TU Clausthal, unpublished.
- Schwan, W., 1995: *Untervorschiebung (Under-forward thrust) – Strukturtyp und Kinematik*, Geologische Blätter NE-Bayern, Erlangen 45 (1–2): 11–102.
- Schwan, W., 1999: *Zur strukturellen, kinematischen und zeitlichen Entwicklung der Frankenwälder Querzone im Thüringisch-Fränkischen Schiefergebirge – Neue Betrachtungen, Fragen und Stellungnahme*, Geologische Blätter NE-Bayern, Erlangen 49 (3–4): 165–242.
- Slichter, L. B., 1961: *The Fundamental Free Mode of the Earth's Inner Core*, Proceedings of the National Academy of Science, USA 47 (2): 186–190.
- Smith, M. L. & Dahlen, F. A., 1981: *The period and Q of the Chandler Wobble*, Geophys. J. R. Astr. Soc. 64 (1): 223–281, doi:10.1111/j.1365-246X.1981.tb02667.x.
- Smylie, D. E., Francis, O., & Merriam, J. B., 2001: *Beyond tides – determination of core properties from superconducting gravimeter observations*, J. Geod. Soc. Japan 47 (1): 364–372.
- Smylie, D. E. & Jiang, X., 1993: *Core oscillations and their detection in superconducting gravimeter records*, J. Geomagnet. Geoelectr. 45 (11–12): 1 347–1 369.
- Steffen, H., Denker, H., & Müller, J., 2008: *Glacial isostatic adjustment in Fennoscandia from GRACE data and comparison with geodynamical models*, J. Geodyn. 46 (3–4): 155–164, doi:10.1016/j.jog.2008.03.002.
- Suda, N., Nawa, K., & Fukao, Y., 1998: *Earth's background free oscillations*, Science 279 (5359): 2 089–2 091, doi:10.1126/science.279.5359.2089.
- Sun, H.-P., 1992: *Comprehensive researches for the effect of the ocean loading on gravity observations in the Western Pacific area.*, Bulletin d'Information des Marées Terrestres 93: 8 271–8 292.
- Sun, H.-P., 1995: *Static deformation and gravity changes at the earth's surface due to atmospheric pressure*, PhD thesis, Catholic University Louvain, Belgium.
- Teupser, C., 1975: *The Seismological Station of Moxa*, in *Seismology and Solid-Earth-Physics*, vol. 14, pp. 577–584, Veröffentlichungen des Zentralinstituts Physik der Erde (ZIPE).
- Timmen, L. & Gitlein, O., 2004: *The capacity of the Scintrex Autograv CG-3M no. 4492 gravimeter for “absolute-scale” surveys*, Rev. Brasil. Cartografia (Brazil. J. Cartography) 56 (2): 89–95.
- Timmermann, A., 1978: *Petrographische Untersuchungen an Grauwacken des Ziegenrücker Synklinoriums*, Jahrbuch für Geologie 9/10: 141–174.

- Toomre, A., 1974: *On the 'nearly diurnal free wobble' of the earth*, *Geophys. J. R. Astr. Soc.* 38: 335–348.
- Torge, W., 1989: *Gravimetry*, Walter de Gruyter, Berlin, New York.
- Torge, W. & Kanngiesser, E., 1980: *Gravity and height variations during the present rifting episode in Northern Iceland*, *J. Geophys.* 47: 125–131.
- Van Camp, M., Vanclooster, M., Crommen, O., Petermans, T., Verbeeck, K., Meurers, B., van Dam, T., & Dassargues, A., 2006: *Hydrogeological investigations at the Membach station, Belgium, and application to correct long periodic gravity variations*, *J. Geophys. Res.* 111 (B10403), doi:10.1029/2006JB004405.
- Vicente, R. & Wilson, C., 2002: *On long period polar motion*, *J. Geodesy* 76 (4): 199–208, doi:10.1007/s00190-001-0241-6.
- Virtanen, H., 2000: *On the observed hydrological environmental effects on gravity at the Metsähovi station, Finland*, *Cahiers du Centre Européen de Géodynamique et de Séismologie* 17: 169–176.
- Virtanen, H., Tervo, M., & Bilker-Koivula, M., 2006: *Comparison of superconducting gravimeter observations with hydrological models of various spatial extents*, *Bulletin d'Information des Marées Terrestres* 142: 11 361–11 368.
- Vitushkin, L., Becker, M., Jiang, Z., Francis, O., van Dam, T. M., Faller, J., Chartier, J.-M., Amalvict, M., Bonvalot, S., Debeglia, N., Desogus, S., Diamant, M., Dupont, F., Falk, R., Gabalda, G., Gagnon, C., Gattacceca, T., Germak, A., Hinderer, J., Jamet, O., Jeffries, G., Käker, R., Kopaev, A., Liard, J., Lindau, A., Longuevergne, L., Luck, B., Maderal, E., Mäkinen, J., Meurers, B., Mizushima, S., Mrlina, J., Newell, D., Origlia, C., Pujol, E., Reinhold, A., Richard, P., Robinson, I., Ruess, D., Thies, S., Van Camp, M., Van Ruymbeke, M., de Villalta Compagni, M., & Williams, S., 2002: *Results of the Sixth International Comparison of Absolute Gravimeters, ICAG-2001*, *Metrologia* 39 (5): 407–424, doi:10.1088/0026-1394/39/5/2.
- Wahr, J. M., 1985: *Deformation Induced by Polar Motion*, *J. Geophys. Res.* 90 (B11): 9 363–9 368, doi:10.1029/JB090iB11p09363.
- Warburton, R. & Goodkind, J., 1977: *The influence of barometric pressure variations on gravity*, *Geophys. J. R. Astr. Soc.* 48: 281–291.
- Wenzel, H.-G., 1993: *Program package GRAVNA – Adjustment of gravity observations*, Fortran-program, Geodetic Institute, University Karlsruhe, unpublished.
- Wenzel, H.-G., 1996: *The nanogal software: Earth tide processing package ETERNA 3.30*, *Bulletin d'Information des Marées Terrestres* 124: 9 425–9 439.

- Wenzel, H.-G., 1997: *Tide generating potential for the earth*, in *Tidal Phenomena* (H. Wilhelm, W. Zürn & H.-G. Wenzel, eds), vol. 66 of *Lecture Notes in Earth Sciences*, pp. 9–26, Springer, Berlin.
- Widmer-Schmidrig, R., 2003: *What Can Superconducting Gravimeters Contribute to Normal-Mode Seismology?*, *Bull. Seismol. Soc. Am.* 93 (3): 1370–1380, doi:10.1785/0120020149.
- Wilson, C. R., Wu, H., Scanlon, B., & Sharp, J. M., 2007: *Taking the Superconducting Gravimeter to the Field – A new tool for Hydrology and Other Investigations*, in *Poster presentation at GRACE Science Team Meeting, 15th–17th October 2007, Potsdam*.
- Wolf, H., 1997: *Ausgleichsrechnung I, Formeln zur praktischen Anwendung*, Dümmlers, Bonn, 3rd edn.
- Wucher, K., 1997: *Zur tektonischen Entwicklung des Südostteiles der Frankenwälder Querzone (Thüringisch-Fränkisches Schiefergebirge)*, *Geowissenschaftliche Mitteilungen Thüringen*, Weimar 6: 21–155.
- Wucher, K., Puff, P., & Steinmüller, A., 2001: *Geologische Karte von Thüringen 1:25.000, no. 5335 Saalfeld (Saale)*, Thüringer Landesanstalt für Umwelt und Geologie, Jena.
- Zahran, K. H., 2000: *Accuracy assessment of ocean tide loading computations for precise geodetic observations*, in *Wissenschaftliche Arbeiten der Fachrichtung Vermessungswesen der Universität Hannover*, vol. 238, Universität Hannover, Fachrichtung Vermessungswesen.
- Zahran, K. H., Jentzsch, G., & Seeber, G., 2006: *Accuracy assessment of ocean tide loading computations for precise geodetic observations*, *J. Geodyn.* 42 (4–5): 159–174, doi:10.1016/j.jog.2006.07.002.
- Zerbini, S., Richter, B., Negusini, M., Romagnoli, C., Simon, D., Domenichini, F., & Schwahn, W., 2001: *Height and gravity variations by continuous GPS, gravity and environmental parameter observations in the southern Po Plain, near Bologna, Italy*, *Earth Planet. Sci. Lett.* 192 (3): 267–279, doi:10.1016/S0012-821X(01)00445-9.
- Zimmermann, E., 1912: *Das Diluvium auf Blatt Saalfeld mit Erläuterungen*, Jahrbuch der Königlich Preußischen Landesanstalt, Berlin für 1909.
- Zürn, W., Richter, B., Rydelek, P. A., & Neuberg, J., 1987: *Comments on detection of inertial gravity oscillations in the earth's core with a superconducting gravimeter at Brussels*, *Phys. Earth Planet. Int.* 49: 176–187, doi:10.1016/0031-9201(87)90140-3.

Acknowledgements

First I would like to sincerely thank PD Dr. Corinna Kroner, my supervisor, for providing me this interesting work. Her generous supervision made me feel comfortable in pursuing the subject, and during my work, she had always time for discussion and gave helpful suggestions. Besides her, I am especially indebted to Dr. Adelheid Weise. She always listened to my countless questions and had time for very special scientific and sometimes also non-scientific discussions. The financial support from the German Research Foundation is also gratefully acknowledged.

Prof. Dr. Gerhard Jentzsch I want to thank for the possibility to work on my thesis in his working group “Applied Geophysics”. He and PD Dr. Thomas Jahr deserve special thanks for the unreserved given support in all belongings. Besides them, I would like to thank the other colleagues from the working group and from the Institute of Geosciences of the Friedrich-Schiller-University Jena for the joyful time.

I gratefully acknowledge Prof. Dr. Hans-Jürgen Götze and Dr. Sabine Schmidt for valuable discussions on gravimetric reductions and gravimetric modelling. I am especially indebted to Dr. Sabine Schmidt for providing a special IGMAS version which built a basis for the time-dependent calculations in this thesis.

Dr. Peter Krause and Stefanie Eisner are thanked for providing the results of the local hydrological modelling. From many discussions with them valuable information regarding the local hydrology around Moxa observatory was derived and the one or other hydrological and gravimetrical riddle was solved. Norbert Kasch I thank for providing the geological basis for my work. For all geological questions, he was the contact per se.

The extensive field work around Moxa observatory would not have been possible without the contribution of a number of persons. I thank Raphael Dlugosch, Holger Hartmann, Katrin Heintz, Anne Hegewald, Romy Schmidt, Stefanie Zeumann, and Albrecht Ziegert for their help. And, of course, the work of Wernfrid Kühnel and Matthias Meininger in establishing and maintaining the hydrological observation network at Moxa observatory, constructing the gravimeter lift, and repairing everything what scientists break is gratefully acknowledged.

My thanks go to Andreas Hoffmann for many valuable hints in the Linux and Windows world and the help in speed of light with the one or other evil computer problem.

I am especially thankful to Dr. Holger Steffen and Maida Appel for carefully reading the manuscript. Besides them I would like to thank my friends and colleagues, who accompanied my life and work in the last years. Along with all others I want to mention Dr. Wiete Beel, Fabian Jähne, Steffen Goldau, Dr. Jörg Hennig, Dirk Munsel, Christian Zeidler and Uwe Zubrinna.

My wife Viktoriya supported me whenever I needed her, I thank you with all my heart. And my little daughter Sophie lighted up the days and my heart with her smile.

My final words are dedicated to my parents. Their encouragement, support and good wishes made me what I am today.

Selbstständigkeitserklärung

Ich erkläre, dass ich die vorliegende Arbeit selbstständig und unter Verwendung der angegebenen Hilfsmittel, persönlichen Mitteilungen und Quellen angefertigt habe.

Jena, den 17. Oktober 2008

Marco Naujoks

Curriculum Vitae

Personal details

Name: Marco Naujoks
Date of birth: 03 July 1978
Place of birth: Eisenach
Nationality: German
Marital status: Married, 1 child

Education

09/85 to 08/90 10th Polytechnische Oberschule –
Primary and Secondary School in Eisenach

09/90 to 07/97 Elisabeth-Gymnasium – Grammar school in Eisenach
07/97 Abitur (A-levels), Gesamtnote 1,5 (Grade: “very good”)

10/98 to 10/04 Study of Geophysics at Friedrich-Schiller-University Jena
09/01 Vordiplom (Gesamtnote 1,3)
Intermediate examination (Grade: “very good”)

10/04 Diplom in Geophysik (Gesamtnote 1,0 – mit Auszeichnung)
Diploma (MSc) in Geophysics (Grade: “very good, with distinction”)
Majors: *Geophysics, Physics, Geology, Computer Sciences*
Thesis: *Modelling regarding physical mechanisms in earthquake swarm areas worldwide: similarities and differences*

since 11/04 PhD student at Friedrich-Schiller-University Jena

Contracts

08/97 to 09/98 Civil service at the nursing home “Wartburgblick” in Eisenach

01/03 to 02/03 Alfred Wegener Institute for Polar and Marine Research in Bremerhaven, geophysical cruise on the research vessel *FS Sonne*
Tasks: *refraction seismics and wide angle reflection seismics*

since 11/04 Research Associate in the working group “Applied Geophysics” at the Institute of Geosciences of the Friedrich-Schiller-University Jena
Scientific Tasks: *research on hydrological information in gravity*

Jena, 17th October 2008

Marco Naujoks

